ABSTRACT

Title of Dissertation: FLOQUET HEATING AND RELAXATION
OF INTERACTING BOSE EINSTEIN CONDENSATES

James Maslek
Doctor of Philosophy, 2022

Dissertation Directed by: Professor Trey Porto
Department of Physics

Floquet's theorem says that any unitary, periodically driven system can be described by an effective time-independent Hamiltonian, where the effective Hamiltonian can have completely different properties than the static, undriven system. Floquet engineering makes use of this idea to simulate new Hamiltonians that would otherwise not be possible in the undriven case. For interacting systems, this approach can be used to realize interesting correlated many-body states, but drive-induced heating must be understood and mitigated. Cold atoms in optical lattices provide a controllable, well-isolated system in which these ideas can and have been realized. I describe research into two areas of Floquet engineering for interacting Bose-Einstein condensates in periodically driven optical lattices.

The first half of this thesis focuses on the study of heating mechanisms for condensates in periodically driven lattices. In the weakly interacting limit, one might expect that heating could be described with a Fermi Golden Rule approach. Parametric driving of fluctuations in the

condensate, however, can lead to runaway heating that cannot be described perturbatively. We experimentally study heating in shaken 2D square lattices and demonstrate heating consistent with the theoretical predictions of parametric instabilities.

The second half of this thesis describes experiments that realize Floquet-induced effective staggered magnetic fields, and the relaxation dynamics of interacting particles subject to these fields. Interestingly, we observe pre-thermal relaxation dynamics, where an initially heated cloud suddenly subject to the effective Hamiltonian condenses into a state governed by the drive-induced effective Hamilton on a timescale faster than heating.

FLOQUET HEATING AND RELAXATION IN INTERACTING BOSE EINSTEIN CONDENSATES

by

James Maslek

Dissertation submitted to the Faculty of the Graduate School of the
University of Maryland, College Park in partial fulfillment
of the requirements for the degree of
Doctor of Philosophy
2022

Advisory Committee:
Professor Steven Rolston, Chair
Professor Trey Porto, Co-Chair/Advisor
Professor Gretchen Campbell
Professor Victor Galitski.
Professor Thomas Murphy (Dean's Representative)

Acknowledgments

I would like to start off by thanking Trey for the opportunity to join the Rubidium 1 when I was still an undergrad at Rochester. I appreciate your guidance and support throughout the years and I will always be amazed that you turned your house into a sundial. I will take to my grave that python is superior to Mathematica. Additionally, thank you to Steve, Gretchen and Alicia for help and mentorship through the CPRK group.

I would like to acknowledge my lab mate Carlos, it was a pleasure to work with over the last many years. From building 80/20 in an empty room and figuring out if a laser that fell in a car was broke to jerry-rigging the vacuum shutter minutes before opening it up, I enjoyed learning and growing through grad school with you. Additionally, throughout my time, I have had the pleasure to work with a great bunch of people on the Rb1 experiment: Thomas, Eric, Elizabeth, Daniel, AJ, Pierre.

I would like to thank my family for their continued support over the last 20 years of school.

Finally, to my wife, Marisa. It was fun getting to have two weddings over the pandemic, but you were always there for me. And you let me get a doggo, Cooper, so thanks for that.

Go Bills.

Table of Contents

List of Figures

Chapter 1: Introduction

Floquet engineering is a powerful tool that makes use of a periodic modulation to simulate an effective time independent system, where the resulting time independent system can exhibit behaviors that are not present in the static system. Cold atoms in optical lattices provide a controllable, well isolated system in which these ideas can and have been realized. Circular driving of a honeycomb lattice has been performed to realize the Haldene model [1], which exhibits a topological band structure. Periodic driving in optical superlattices has been used to simulate the Harper-Hofstadter model with neutral atoms [2, 3, 4]. The simulation of the Harper-Hofstadter Hamiltonian is a specific realization of artificial gauge fields[5], which have been studied in Floquet engineered systems [6, 7, 8, 9]. Additionally, Floquet engineering has been proposed as a method to generate fractional quantum hall states [10, 11], and experimentally simulate Z2 lattice gauge theories [12].

Despite the interesting new possibilities that emerge in time periodic systems, the addition of energy, particularly in interacting systems, inevitably results in heating, which in itself is an outstanding theoretical and experimental area of investigation. Although the continual addition of energy eventually heats the system to infinite temperature [13, 14], there can exist a range of parameters for which there is different behavior on intermediate timescales. These "prethermal" states emerge as an approximate equilibrium condition where the system has thermalized

according to the effective Hamiltonian associated with the periodic modulation, which is different from the full time dependent Hamiltonian [15, 16, 17]. For lattice systems with locally bounded Hilbert spaces, such "Floquet pre-thermalization" is generally expected in the limit of high frequency driving [15, 18, 19, 20]. While the Hilbert spaces of real systems are not locally bounded, if the states of interest are separated from all other states by a sufficient energy gap, Floquet pre-thermalization can occur [21].

In this thesis, I describe research into two areas of Floquet engineering for Bose-Einstein condensates in periodically driven optical lattices. The first is a mechanism of heating on condensates in an optical lattice. Previous theoretical work presented two main descriptions of heating dynamics for bosons in driven optical lattices. One is a Fermi golden rule approach where the periodic driving of the lattice couples atoms to many other states, which is expected to be accurate for weakly heating systems. The second, which is the focus of our work, is applicable for interacting mean-field systems with bosonic excitations. This strong heating arises due to the existence of parametric instabilities in the Floquet system. Driving resonantly excites modes, which can then grow exponentially under the right conditions and result in a depletion of the condensate.

The second aspect of this thesis is the realization of effective staggered fields in a Floquet system and the study of interaction driven dynamics in the effective system. Circularly driving the optical lattice, under the right conditions, leads to an effective system with complex tunneling parameters that can be described by an effective magnetic field. The effective magnetic field is similar to the Harper-Hofstadter model, which describes particles in a lattice subject to a gauge field. The Harper-Hofstadter model was motivated by the band structure of an electron on a lattice in a magnetic field, which results in the fractal Hofstadter butterfly band structure [22]. One of

the signatures of the gauge field is that the bands display minima at non-zero quasimomentum. In our work, we study the relaxation of atoms into these non-zero momentum states and the extent to which the full Hamiltonian for atoms in the circularly driven lattice can be approximated by the effective tight binding model.

The outline of this thesis is as follows. Chapter 2 starts with the theoretical background relevant to the main experimental results in this work. Chapter 3 goes into the experimental apparatus used for the work, with the primary focus on the design of our tripod-piezo mirrors that allowed us to perform Floquet experiments. Chapters 4 and 5 go into the main experiments performed, the study of parametric instabilities and the study of prethermal BEC relaxation, respectively. Chapter 6 provides an outlook into future work that can be explored with our experimental techniques.

Chapter 2: Background

This section provides some of the background physics that will be discussed throughout the rest of this thesis. The primary focus is the emergence of heating and relaxation in Floquet-engineered systems.

The starting point for all my research was a Bose Einstein Condensate (BEC) loaded into an optical lattice. The physics of BECs and their production has been extensively studied and documented elsewhere (see [23, 24]). I will limit the discussion of background topics to the aspects needed for the works in this thesis

2.1 Floquet Theory

Periodically driven systems exhibit properties similar to those of systems with a periodic spatial potential. Instead of repeating in space, the Hamiltonian repeats in time, with a period T, $H(t+T) = H(t)$. The starting point is the Schrödinger equation:

$$i\hbar\frac{\partial\psi(x,t)}{\partial_t} = H(t)\psi(x,t) \tag{2.1}$$

Because the Hamiltonian is time periodic, the Floquet theorem says that we can expand $\psi(x,t)$ in terms of Floquet modes, $\phi_n(x,t)$, which have the same periodicity as the Hamiltonian, $\phi_n(x,t) =$

$\phi_n(x, t+T)$ [25]

$$\psi(x,t) = \sum_n \phi_n(x,t) e^{-i\epsilon_n t/\hbar} \tag{2.2}$$

The quantities ϵ_n are known as quasi-energies, and they resemble the quasi-momentum that appear in the Bloch expansion of periodic spatial potentials. Substituting this expansion into (2.1) gives an eigenvalue equation for the Floquet modes

$$\left(H(t) - i\hbar\frac{\partial}{\partial t}\right)\phi_n(x,t) = \epsilon_n \phi_n(x,t). \tag{2.3}$$

The Floquet modes are time periodic, with frequency $\omega = 2\pi/T$, so they can be expanded in harmonics of ω, namely $\phi_n(x,t) = \sum_m \chi_{nm}(x) e^{im\omega t}$, where χ_{nm} are the spatial modes of the mth fourier component. At this point, the total wavefunction ψ is given by

$$\psi(x,t) = \sum_{n,m} e^{-i\epsilon_n t/\hbar} e^{im\omega t} \chi_{nm}(x) \tag{2.4}$$

The Floquet mode, $\phi_{nj} = \phi_n e^{ij\omega t}$ can be substituted into Eq. 2.3, which yields an identical solution, but with a shifted quasienergy, namely $\epsilon_{nj} = \epsilon_n + j\hbar\omega$ [26]. This implies that the Floquet modes ϕ_n and $e^{ij\omega t}\phi_n$ are the same physical state, but they differ in quasienergy by j photons ($j\hbar\omega$). The quasi-energy spectrum resembles a Brillouin zone, where the quasienergies can take values in a reduced energy zone, $[-\hbar\omega/2, \hbar\omega/2]$.

2.2 Time Evolution Operator

Going back to the Schrödinger equation, if we have an initial state $\psi(x, t_0)$, then we can time-evolve this state using the operator $U(t, t_0)$, such that at time, t, (writing $\psi(x, t)$ as $|\psi(t)\rangle$)

$$|\psi(t)\rangle = U(t, t_0)|\psi(t_0)\rangle \tag{2.5}$$

U is the operator which is defined to be a solution to the Schrödinger equation, namely

$$i\hbar\partial_t U(t, t_0) = H(t)U(t, t_0). \tag{2.6}$$

This has the general solution

$$U(t, t_0) = \mathcal{T} \exp\left(-i/\hbar \int_{t_0}^{t} H(t')dt'\right), \tag{2.7}$$

where the $\mathcal{T}$ indicates a time ordered product. Since our Hamiltonian is periodic in time, the time evolution operator is time periodic as well, namely evolving from a time t_0 for an integer number of periods, nT, results in $U(nT, 0) = U(T, 0)U(nT - T, 0)... = (U(T))^n$ (where t_0 is taken to be 0 without loss of generality).

According to Floquet theory, we can now express this time evolution as

$$U(t_2, t_1) \equiv e^{-iK(t_2)}e^{-i(t_2-t_1)H_{\text{eff}}}e^{iK(t_1)}, \tag{2.8}$$

where $K(t)$ is a "Kick" operator, which is periodic with zero average value and H_{eff} is an effective

Hamiltonian which, for properly chosen $K(t)$, has no time dependence [6]. The kick operator can also be interpreted as an effective initial condition for the drive. The effective Hamiltonian, H_{eff} can display properties different from the time dependent H, such as topological structure or interesting energy dispersions. This is the premise of Floquet engineering, in that interesting effective Hamiltonians can be simulated through a periodically driven system.

2.3 High Frequency Expansion

In most systems, Eq. 2.8 will not be useful for finding analytical results for H_{eff}. In many cases, a high frequency expansion in $1/\omega = T/2\pi$, can be used to accurately describe the system. Ignoring the kick operators, the time evolution is governed by $U(T) = \exp(-iTH_{\text{eff}}) = \exp(-2\pi i H_{\text{eff}}/\omega)$. In realistic experimental setups, a smooth turning on of the drive can largely mediate the effect of the kick operator. The time evolution operator can be expanded in terms of the inverse frequency,

$$H_{\text{eff}} = \sum_{n=0} \frac{H^{[n]}}{(\hbar\omega)^n}. \tag{2.9}$$

Since the time dependent Hamiltonian is periodic, it can be expanded in fourier terms, $H(t) = \sum_\ell h_\ell e^{i\ell\omega t}$. The first two terms in this high frequency expansion of the effective Hamiltonian are given as [27, 28]

$$H^{[0]} = \frac{1}{T}\int_0^T H(t)dt = h_0 \tag{2.10}$$

$$H^{[1]} = \sum_\ell \frac{1}{\ell}[h_\ell, h_{-\ell}], \tag{2.11}$$

which is referred to either as the High Frequency expansion (HFE) or the Magnus Expansion [29] and can be extended to higher orders in $(1/\omega)$.

2.4 Mean Field Theory

Having done a quick overview of Floquet theory, I now discuss the relevant physics of cold atoms. In the second quantization description of our system of particles, the field operators, $\hat{\Psi}(x)(\hat{\Psi}^\dagger(x))$ are defined to be the annihilation (creation) of a boson at position x. The Hamiltonian for N bosons in a confining potential, V_{ext}, subject to two body interactions, $V(x_i - x_j)$, is given as

$$\begin{aligned} H = \int d^3x\ \hat{\Psi}^\dagger(x) \left(\frac{-\hbar^2}{2m}\nabla^2 + V_{ext}(x) \right) \hat{\Psi}(x) \\ +\frac{1}{2}\int d^3x\ d^3x'\ \hat{\Psi}^\dagger(x)\hat{\Psi}^\dagger(x')V(x-x')\hat{\Psi}(x)\hat{\Psi}(x') \end{aligned} \tag{2.12}$$

Properties of this Hamiltonian can be computed from this expression, but as the number of particles increases, the complexity of the Hamiltonian increases, and calculations become computationally expensive. In order to formulate a framework that can simplify these calculations, we introduce a mean-field approach, where we separate out the contribution from the condensate to the field operator, and treat interactions with the condensate with an average mean field. The field operator can be expanded into a mode basis as $\hat{\Psi} = \sum_n \psi_n a_n$, which annihilates a single particle wave function, ψ_n and the index n runs over a complete set of orthonormal basis states. The mode annihilation and creation operators satisfy the usual bosonic commutation relations: $[a_n, a_m^\dagger] = \delta_{n,m}$.

The condensate can be described as a macroscopic occupation of a single particle state and

adding a particle will not significantly change the physical configuration, meaning that $N_0 \approx N_0 + 1$. In this situation, the annihilation and creation operators can be expressed as just a complex number, which we denote as $a = a^\dagger = \sqrt{N_0}$, such that $N = a^\dagger a$. The BEC mean field single-particle state, $\psi_0 = \sqrt{N_0/V}$, confined to a volume V, has zero momentum and its density is given by $|\psi_0|^2$, which is proportional to the total number of condensed particles, N_0. The total state in mean this mean field approach is then represented as the BEC plus a small fluctuation, $\Psi = \psi_0 + \delta\psi$.

2.5 Weakly Interacting Condensates : GP Limit

Given the classical field $\Psi(r,t)$, we first assume that there are no fluctuations and that the single particle state is time dependent, $\Psi(r,t) = \phi(r,t)$ and look at the time evolution from the non-linear Schrödinger equation:

$$\begin{aligned} i\hbar\partial_t\phi(r,t) &= -\frac{\hbar^2\nabla^2}{2m}\phi(r,t) + V_{ext}(r)\ \phi(r,t) \\ &+ \left(\int d^3x'\phi^\dagger(r,t)V(x'-x)\phi(r,t)\right)\phi(r,t). \end{aligned} \tag{2.13}$$

For weakly interacting condensates in a dilute, low temperature system, the interaction is dominated by s-wave scattering, so we replace the interaction with a delta function with strength proportional to the scattering length, a:

$$V(x'-x) = \frac{4\pi\hbar^2 a}{m}\delta(x'-x). \tag{2.14}$$

Substitution of this into (2.13) results in the Gross-Pitaevskii (GP) equation:

$$i\hbar\partial_t\phi(r,t) = \left(-\frac{\hbar^2\nabla^2}{2m} + V_{ext}(r) + \frac{4\pi\hbar^2 a}{m}|\phi(r,t)|^2\right)\phi(r,t). \tag{2.15}$$

This nonlinear equation governs the evolution for the condensate under the assumption that there is a macroscopic number of particles, the scattering length is smaller than the average distance between bosons, and the interactions are weak enough that the ground state is not highly correlated.

The ground state of the mean-field Hamiltonian can be written $\phi(r,t) = \Phi(r)e^{-i\mu t/\hbar}$ where Φ is a real function with normalization given by $\int dx\Phi(x) = N$ and μ is the chemical potential. Defining the interaction strength to be $g = 4\pi\hbar^2 a/m$, the GP equation for the ground state simplifies to the following nonlinear Schrödinger equation:

$$\mu\Phi(x) = \left(\frac{-\hbar^2\nabla^2}{2m} + V_{ext}(x) + g\Phi^2(x)\right)\Phi(x). \tag{2.16}$$

In the limit where the kinetic energy can be neglected with respect to interactions, known at the Thomas-Fermi regime, the atomic density, $n(x) = \Phi(x)^2$ can be written as

$$n(x) = \frac{1}{g}\left(\mu - V_{ext}(x)\right). \tag{2.17}$$

For a harmonic external potential (such as an optical dipole trap), this is an inverted parabola for points where the chemical potential is greater than the external potential, and 0 otherwise (since $\Phi(x)$ is real). In realistic experimental setups, there is a thermal component as well, so the total atomic distribution can be approximated as a sum of a thermal gaussian distribution and this

Thomas Fermi inverted parabola.

2.6 Bogoliubov Theory

I now consider excitations of the BEC, which is assumed to be homogenous and lattice free, in the presence of weak interactions. To characterize interactions, we choose the plane-wave basis for expanding the field operator, $\hat{\Psi}^\dagger(x) = \hat{a}_p e^{ipx}/\sqrt{V}$, where V is the volume of the uniform gas, which results in the following momentum space Hamiltonian:

$$H = \sum_p \frac{p^2}{2m} a_p^\dagger a_p + \frac{g}{2V} \sum_{p_1,p_2,q} a_{p_1+q}^\dagger a_{p_2-q}^\dagger a_{p_1} a_{p_2}. \tag{2.18}$$

In the limit of no interactions, the free particle dispersion, $p^2/2m$, is recovered. To include the interaction terms, we can apply perturbation theory, starting with atoms condensed in the BEC ($p = 0$) state. Allowing for excitations into a plane wave of momentum k, the total number of atoms will be given as $N = N_0 + \sum a_k^\dagger a_k \approx N_0$. If we expand the Hamiltonian in powers of $a_k^{(\dagger)}$ and ignore any higher order excitations, everything remains condensed in $p = 0$, and the contribution is $\frac{g}{2V} a_0^\dagger a_0^\dagger a_0 a_0 = \frac{gN_0^2}{2V}$.

First order processes in the Hamiltonian violate conservation of momentum, as they contain terms such as $a_k^\dagger a_0^\dagger a_0 a_0 = N_0 a_k^\dagger a_0$. In order to conserve momentum, terms that include second order processes have to be included, which results in:

$$\frac{g}{2V} \sum_{p_1,p_2,q} a_{p_1+q}^\dagger a_{p_2-q}^\dagger a_{p_1} a_{p_2} \to \frac{gN_0}{2V} \sum_k \left(a_k a_{-k} + a_k^\dagger a_{-k}^\dagger + 4 a_k^\dagger a_k \right), \tag{2.19}$$

where these come from the following combinations of (p_1, p_2, q) : (0,0,k), (0,k,0), (k,0,0),

(0,k,k), (k,0,$-k$), (k,$-k$,k). All of these terms result in momentum conservation and are proportional to N_0. In this Bogoliubov approximation, we can make the assumptions that $N_0 \approx N$ and $N_0^2 \approx N^2 - 2N\sum_k a_k^\dagger a_k$ and rewrite the Hamiltonian as:

$$H = \frac{gN^2}{2V} + \sum_k \left(\frac{k^2}{2m} + \frac{gN}{V}\right) a_k^\dagger a_k + \frac{gN}{2V}(a_k^\dagger a_{-k}^\dagger + a_k a_{-k}), \tag{2.20}$$

which is not diagonal in the a_k basis. The linear transformation that diagonalizes Eq. 2.20 is given by [30]:

$$\begin{aligned} a_k &= u_k b_k + v_k b_{-k}^\dagger \\ a_k^\dagger &= u_k b_k^\dagger + v_k b_{-k} \end{aligned} \tag{2.21}$$

To maintain the same commutation relations, $[b_k, b_{k'}^\dagger] = \delta_{kk'}$, the relationship $|u_k|^2 - |v_k|^2 = 1$ must hold, which is done by defining a parameter θ_k, in which $u_k = \cosh(\theta_k), v_k = \sinh(\theta_k)$. Diagonalizing Eq. 2.20 requires that the $b_k^\dagger b_{-k}^\dagger + b_k b_{-k}$ terms vanish, and that the following relationship holds.

$$\left(\frac{k^2}{2m} + \frac{gN}{V}\right) u_k v_k + \frac{gN}{2V}(u_k^2 + v_k^2) = 0 \tag{2.22}$$

Substitution of Eq. 2.21 into Eq.2.22 defines our parameter θ_k:

$$\coth(2\theta_k) = -\frac{\frac{k^2}{2m} + \frac{gN}{V}}{\frac{gN}{V}} \tag{2.23}$$

The diagonal contribution of 2.20 is given by

$$\sum_k \left[\left(\frac{k^2}{2m} + \frac{gN}{V}\right)(u_k^2 + v_k^2) + \frac{gN}{V} u_k v_k\right] b_k^\dagger b_k = \sum_k E(k) b_k^\dagger b_k, \tag{2.24}$$

where

$$E(k) = \sqrt{\left(\frac{k^2}{2m} + \frac{gN}{V}\right)^2 - \left(\frac{gN}{V}\right)^2} \tag{2.25}$$

The collective mode dispersion, Eq. 2.25, is shown in Fig. 2.1. In the limit of no interactions, the quadratic free particle dispersion is recovered and in the presence of interactions, for small momentum, the dispersion is linear, with a speed of sound given by $v_s = \sqrt{gN/Vm}$ [31]. As the interaction parameter is increased, the speed of sound, or the slope of the dispersion, is increased as shown in the figure. The appearance of this linear dispersion can be interpreted as a Goldstone mode arising from the broken U(1) symmetry of the BEC [32]. In the limit of large momentum (low wavelength), the parabolic free particle dispersion is recovered, with an offset equal to the interaction parameter, U.

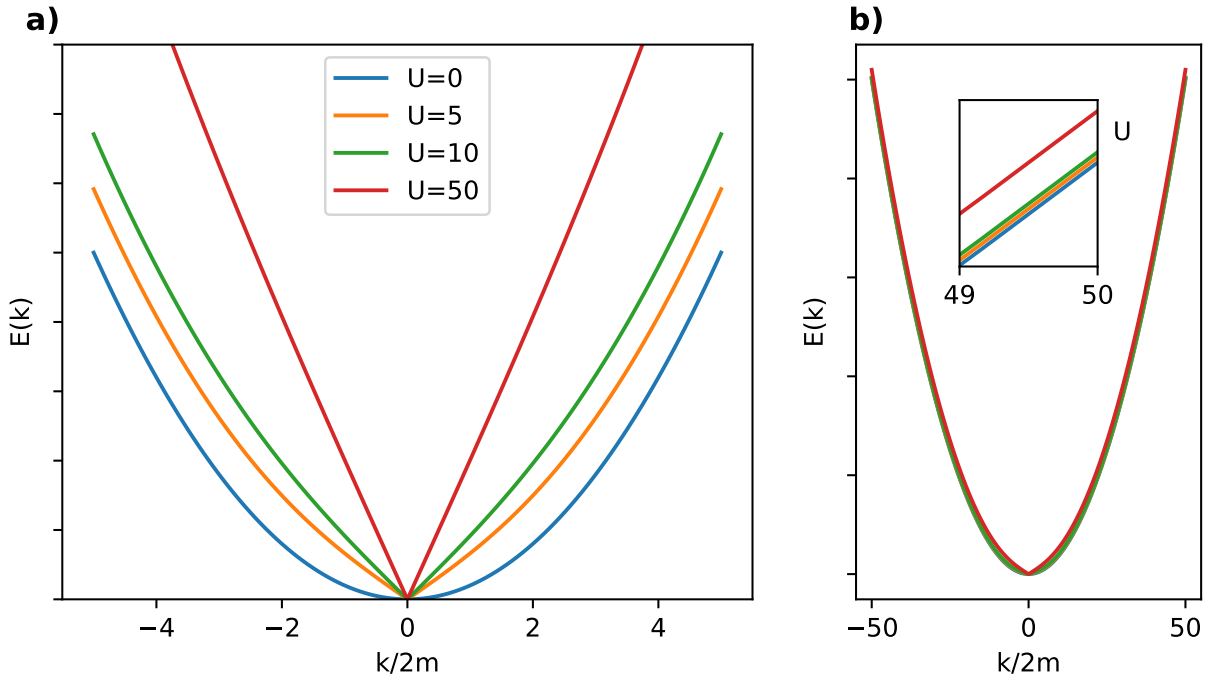

Figure 2.1: Bogoliubov mode dispersion for different interaction parameters, $U = gN/V$. (a) Low momentum, where the dispersion becomes linear with increasing interactions due to the Goldstone mode appearing from the broken U(1) symmetry. (b) High momentum, where the behavior is quadratic, just offset by the interaction parameter U, which is shown in the inset.

2.7 Optical Lattices

Optical lattices are periodic structures that arise from the interference between electric fields of propagating light. For an arbitrary number of beams, the intensity is given as the absolute square of the electric fields, i.e. $I(r,t) = |\sum_i^N \vec{E}_i(r,t)|^2$. In the simplest case of a 1D lattice, where a beam is reflected on itself, the total Electric field is given as $E = E_0(e^{ikx} + e^{-ikx}) = 2E_0\cos(kx)$. The intensity is just the magnitude squared of this, $I = 4|E_0|^2\cos^2(k_x)$ = $I_0(1 + \cos(2kx))$, which is just a standing wave with a spatial period of half the wavelength.

Optical lattices are ideal for quantum simulation tasks because different geometries can be formed by engineering different electric fields. Multiple lattices can be superimposed, resulting in so-called superlattices, such as checkerboard, kagome or honeycomb lattices. Examples of quantum simulation can include studies of magnetization effects, or band structure studies, which may exhibit rich topological features.

For neutral atoms subject to a standing optical wave, their dynamics are governed by the optical dipole force. If we consider our atom to be a two level system, with energy states denoted $|e\rangle$ and $|g\rangle$ for the excited and ground state, respectively, then the energy shift, to second order in the dipole interaction, $H_{int} = -d \cdot E$, is given by [33]:

$$\delta\epsilon_i^{(2)} = \sum_{i \neq j} \frac{|\langle j|dE|i\rangle}{\epsilon_i - \epsilon_j}. \tag{2.26}$$

Defining the Rabi frequency as $\hbar\Omega \equiv d \cdot E$ which couples the two states, and the energy difference

as $\epsilon_i - \epsilon_j \equiv \hbar\Delta$, this can be written as:

$$V = \delta\epsilon = \frac{\Omega^2}{\Delta}. \tag{2.27}$$

There are a few important things to note. Since Ω is proportional to the electric field, the potential felt by the atoms will be proportional to the intensity, which means that for a periodic wave (lattice), the atoms will see a potential of the same period. Another thing to consider is the Rabi frequency. The orientation of the dipole matrix operator was ignored in this simplified derivation, but in the full picture, this contains information regarding the strengths of certain transitions. They are effected by Clebsch-Gordon coefficients, so the same intensity of light can couple different states differently, or not at all. Transitions are also dependent on the orientation of the Electric fields, as angular momentum must be conserved, meaning certain transitions may require circular polarization, whereas others require a linear polarization. The final thing to consider is that atoms in the lab are not two level systems (as I have been told, "There are no two level atoms, and Rubidium is not one of them"). In order to account for the atomic structure, the sum in Eq. 2.26 should be carried out for all dipole allowed transitions.

2.7.1 Band Structure

Now that we have a form for the potential felt by neutral atoms, we wish to solve the Schrödinger equation for atoms in an optical lattice:

$$-\frac{\hbar^2 p^2}{2m}\psi + V\psi = E\psi \tag{2.28}$$

Taking the 1D case as an example, we substitute in the lattice potential, $V = V_0 \sin^2(2kx)$, where V_0 will be a function of the atomic dipole matrix elements and the detuning, and $k \equiv 2\pi/\lambda$:

$$-\frac{\hbar^2 p^2}{2m}\psi + V_0 \sin^2(kx)\psi = E\psi \tag{2.29}$$

Given the periodicity of the lattice potential, we can employ the Bloch theorem, which states the solutions of this equation will be the product of a plane wave, $\exp(iqx)$, and a function $u_q^n(x)$, which will have the same periodic dependence as the lattice. The n subscript now represents the band index and q represents the quasi-momentum which is defined in the range $[-\pi/\lambda, \pi/\lambda]$. We now rewrite the Schrödinger equation in terms of this ansatz (working with $\hbar = 1$):

$$H\phi_q^n = E_q^n \phi_q^n$$

$$\left(-\frac{p^2}{2m} - \frac{V_0}{4}\left(e^{2ikx} + e^{-2ikx} - 2\right)\right) e^{iqx} u_q^n(x) = E_q^n e^{iqx} u_q^n(x) \tag{2.30}$$

Due to the periodicity, it is helpful to Fourier transform u_n in terms of the lattice momentum harmonics

$$u_q^n = \sum_\ell a_l e^{2i\ell kx} \tag{2.31}$$

The kinetic term in the Hamiltonian will just shift p to $p + q$, where p will be the momentum of the ℓ-th component and the lattice potential shifts the Fourier component by $\pm 2k$. This will result in the following eigenvalue equation

$$\sum_{\ell} \frac{(2k\ell+q)^2}{2m} a_\ell e^{2ik\ell} - \sum_{\ell} \frac{V_0}{4} a_\ell \left(e^{2ik(\ell+1)} + e^{2ik(\ell-1)}\right) = E_q^n \sum_{\ell} a_\ell e^{2ik\ell} \tag{2.32}$$

We can match plane wave solutions, which results in the following eigenvalue problem for the coefficients

$$a_\ell \frac{(2k\ell+q)^2}{2m} - \frac{V_0}{4}(a_{\ell-1} + a_{\ell+1}) = E_q^n a_l \tag{2.33}$$

Defining recoil units to be $q_r = \hbar k_r$, $E_R = \frac{\hbar^2 k_r^2}{2m}$, with $k_r = 2\pi/\lambda$ we can recast this as:

$$(2\ell + q/q_r)^2 a_\ell - \frac{V_0}{4E_R}(a_{\ell-1} + a_{\ell+1}) = \frac{E_q^n}{E_R} a_l \tag{2.34}$$

In order to numerically solve this, we truncate the sum to a finite number of components, ℓ_{max}, and compute the plane wave states for $\ell = (-\ell_{max}, \ell_{max})$ which is an eigenvalue problem, where the Hamiltonian is just a tri-driagonal matrix with the following structure.

$$\begin{bmatrix} \ddots & \ddots & 0 & 0 \\ \ddots & (2*(\ell-1)+q/q_r)^2 & -V_0/4 & 0 \\ 0 & -V_0/4 & (2*\ell+q/q_r)^2 & \ddots \\ 0 & \ddots & \ddots & (2*(\ell+1)+q/q_r)^2 \end{bmatrix} \begin{bmatrix} a_{-\ell_{max}} \\ \vdots \\ a_{\ell-1} \\ a_{\ell} \\ a_{\ell+1} \\ \vdots \\ a_{\ell_{max}} \end{bmatrix} = E \begin{bmatrix} a_{-\ell_{max}} \\ \vdots \\ a_{\ell-1} \\ a_{\ell} \\ a_{\ell+1} \\ \vdots \\ a_{\ell_{max}} \end{bmatrix} \tag{2.35}$$

Wannier Functions

In the previous section, the energy band structure was solved for in the presence of an optical lattice. The next step is to determine what the eigenvectors, or the eigenstates are for an atom in an optical lattice. The matrix equation, 2.35, solves for the coefficients introduced in the bloch function (Eq. 2.31), and the bloch wave associated with this solution is delocalized over all sites, due to the $a_i^\dagger a_{i+1}$ terms, which are off-diagonal in the site location. In order to determine

a localized wave function for an atom in a given site, we introduce the Wannier functions, which make up an orthonormal basis for an atom in the nth energy band. The Wannier functions represent the most localized function one can construct from the Bloch solutions confined to a single band, and can be expressed as:

$$\mathcal{W}_n(x - x_i) = \sum_q e^{-iqx_i} \phi_q^n = \sum_\ell \sum_q a_\ell \, e^{-iqx_i} e^{2ikx\ell} \tag{2.36}$$

Figure 2.2 shows the lowest Wannier orbital for increasing lattice depths. As the lattice depth increases, the Wannier function becomes more localized to a specific site, and there is a decreased lobe on the next nearest site, indicating a reduced probability of tunneling to the next site. We note that the Wannier functions are not eigenstates of the Hamiltonian.

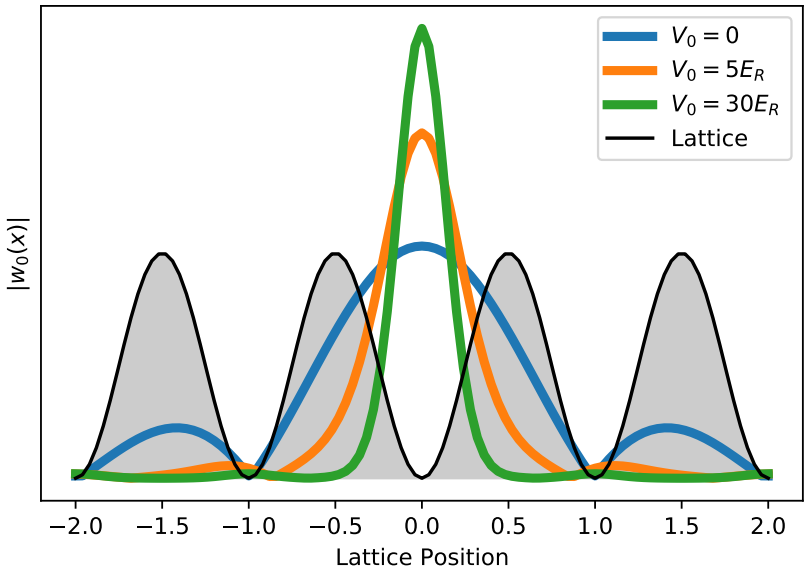

Figure 2.2: Wannier function corresponding to ground band of optical lattice at different depths. The absolute value is taken to show the overlap on the next nearest site.

2.7.2 2D Checkerboard Band Structure

In the Rubidium-1 experiment, we work with a 2D optical lattice that is formed by a single beam that is folded to retro-reflect upon itself twice (sketch in Chapter 3). The relative polarization allows for control of an in plane and out of plane lattice, resulting in a dynamically controllable lattice with 2 sites per unit cell. The total potential seen by the atoms is given by ([34]):

$$I = I_{2D} + I_z = \underbrace{2\cos(2kx - 2\theta_{xy} - 2\phi_{xy}) + 2\cos(2ky + 2\phi_{xy}) + 4}_{I_{2D}} + \underbrace{4\left(\cos(kx - \theta_z - \phi_z) + \cos(ky + \phi_z)\right)^2}_{I_z}, \tag{2.37}$$

where the ϕ and θ variables define the relative phase due to the polarization.

For the case of $\theta_{xy} = \theta_z = \phi_{xy} = \phi_z = 0$, we have a pure checkerboard lattice where the out of plane lattice has twice the spatial period and the double well structure is seen. Figure 2.3 shows an example lattice where the double well structure appears due to the sum of the two lattices. The phase θ controls the location of the λ (out of plane) lattice, and Fig. 2.3 shows that this allows for control of the geometry from something that has double wells to a dimerized lattice.

Just as with the 1D case, we now seek solutions of the Schrödinger equation $H\psi = E\psi$ and start by expanding in plane waves $\psi = \sum e^{iq\cdot r}\phi_q(r)$. In the checkerboard case, the lattice can be written in terms of the reciprocal lattice vectors, $\hat{b}_{1(2)} = \hat{x} \pm \hat{y}$. The in plane and out of

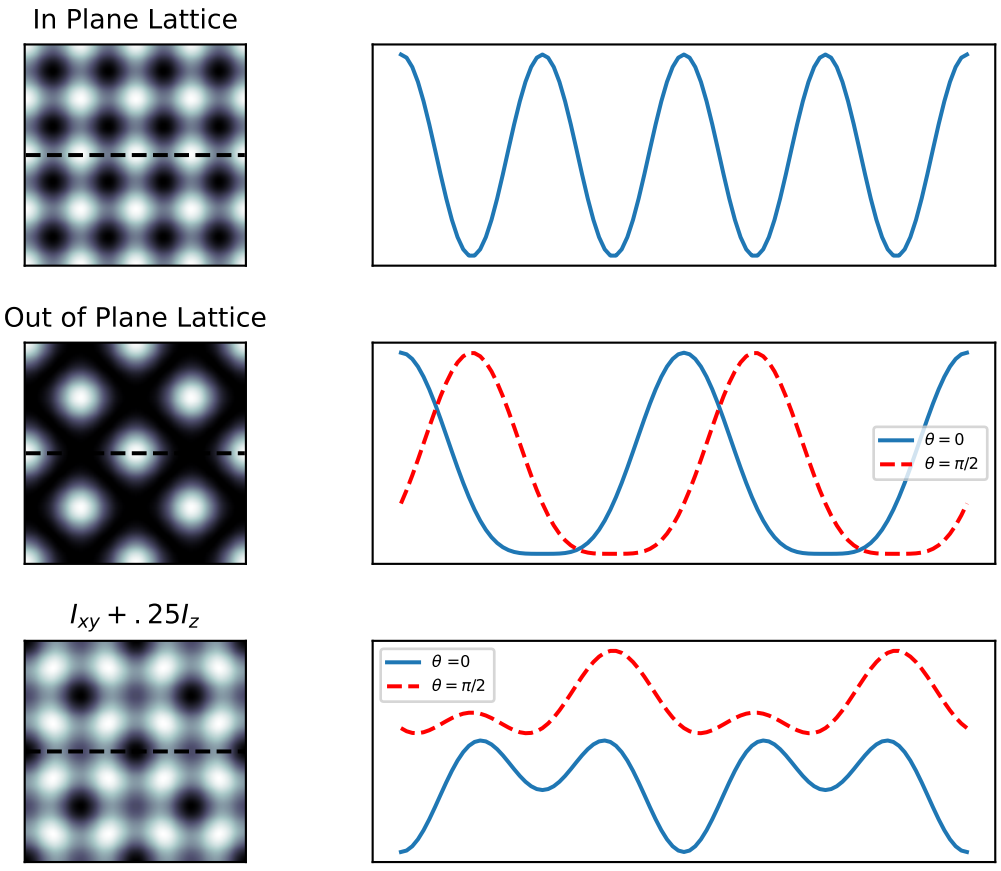

Figure 2.3: Checkerboard optical lattice, where the white (black) indicates maximum (minimum) intensities. The total intensity (bottom left) is the sum of the in-plane (top) and out of plane (middle) intensities. The red curves on the right indicate a different θ, changing the location of the out of plane lattice from the $\lambda/2$ minimum to the barrier (bottom right is offset for visual aid).

plane potentials can be rewritten as:

$$V_{xy}(x,y) = -\frac{V_{2D}}{8}\left(e^{i(b_1+b_2)\cdot r} + e^{-i(b_1+b_2)\cdot r} + e^{i(b_2-b_1)\cdot r} + e^{-i(b_2-b_1)\cdot r} + 4\right) \tag{2.38}$$

$$\begin{aligned} V_z = -\frac{V_z}{16}(4 + 2e^{ib_2\cdot r} + 2e^{-ib_2\cdot r} + 2e^{ib_1\cdot r} + 2e^{-ib_1\cdot r} + e^{i(b_1+b_2)\cdot r} + e^{-i(b_1+b_2)\cdot r} \\ + e^{i(b_2-b_1)\cdot r} + e^{-i(b_2-b_1)\cdot r}) \end{aligned} \tag{2.39}$$

Expanding the bloch function in terms of plane wave components $\phi_n = \sum_{m,n} a_{mn} e^{imb_1+inb_2}$, the 2D potential couples terms that differ in reciprocal vectors by either 1 $b_{1(2)}$ or any combination of $\pm b_1 \pm b_2$. An example Hamiltonian is illustrated in Fig. 2.4 in the form of a matrix plot, illustrating the sparseness. This example is using a cutoff of 2 plane waves, resulting in a $(2n+1)^2$ = 25 x 25 matrix, where each element denotes a plane wave with momentum $nb_1 + mb_2$. The diagonal elements represent the kinetic energy terms, $(p + 2nk + 2mk)^2$.

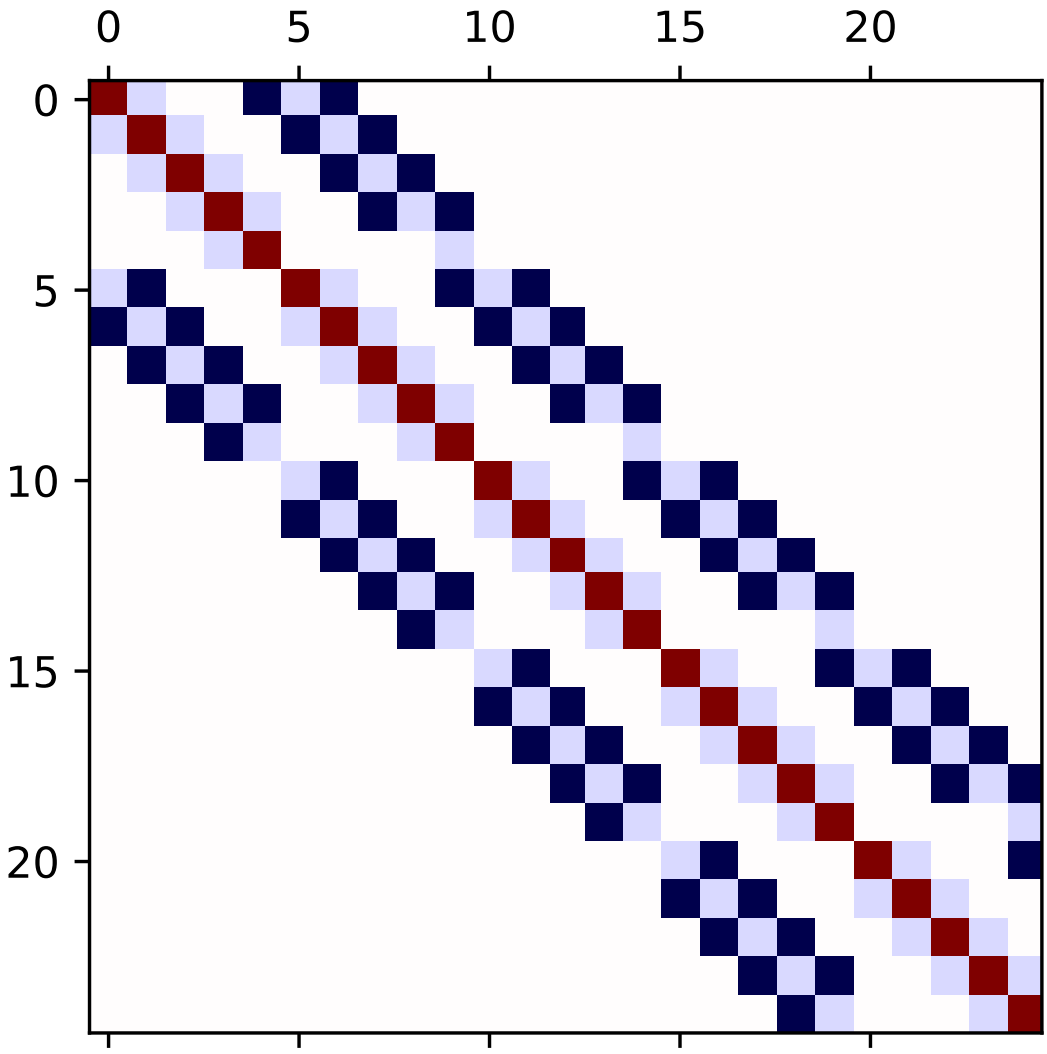

Figure 2.4: Matrix plot of the elements of a Hamiltonian matrix for a cutoff of 2 plane waves. The red points on the diagonals represent the kinetic energy, whereas the off-diagonal elements represent coupling due to the lattice.

Figure 2.5 shows the two lowest bands for a 3 E_R lattice with 0.5 E_R out of plane lattice. Under these conditions, the $q = 0$ gap is approximately 3600 Hz, and the total width of the ground band is 1100 Hz (defined as max-min). Figure 2.6 shows the effect of increasing the out of plane lattice while keeping the same in plane lattice. Increasing the tilt increases the gap along the

edges while simultaneously flattening the lowest bands.

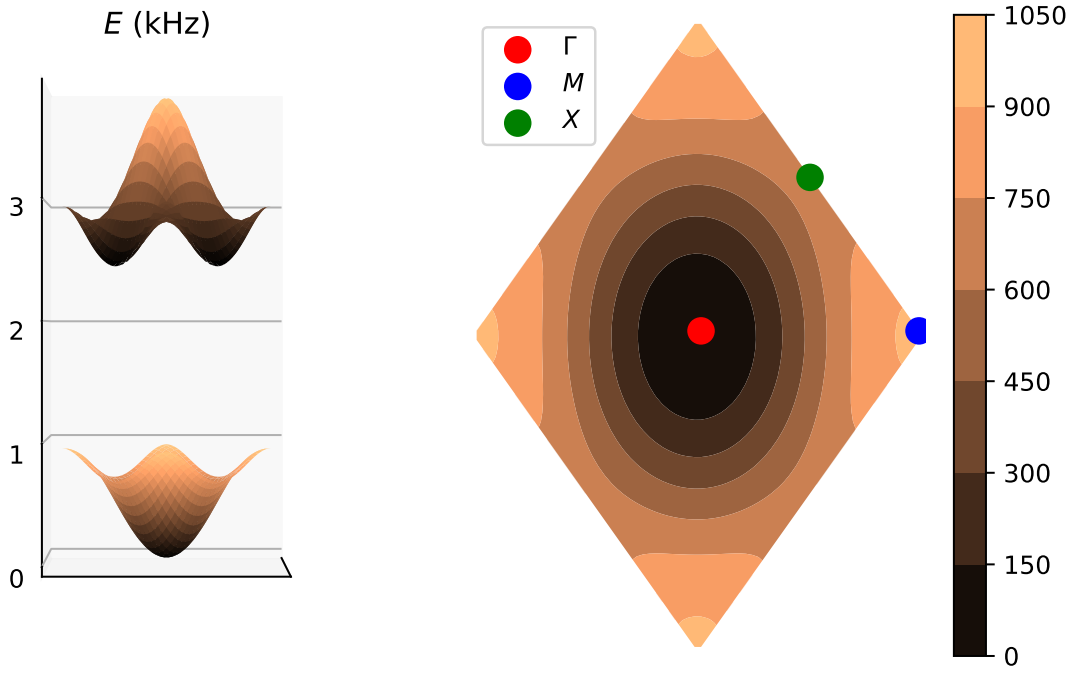

Figure 2.5: Left: Lowest two bands for a 3 E_R lattice with 0.5 E_R out of plane lattice. Right: projection of lowest band onto 2D plane. Γ, K and X points are labeled.

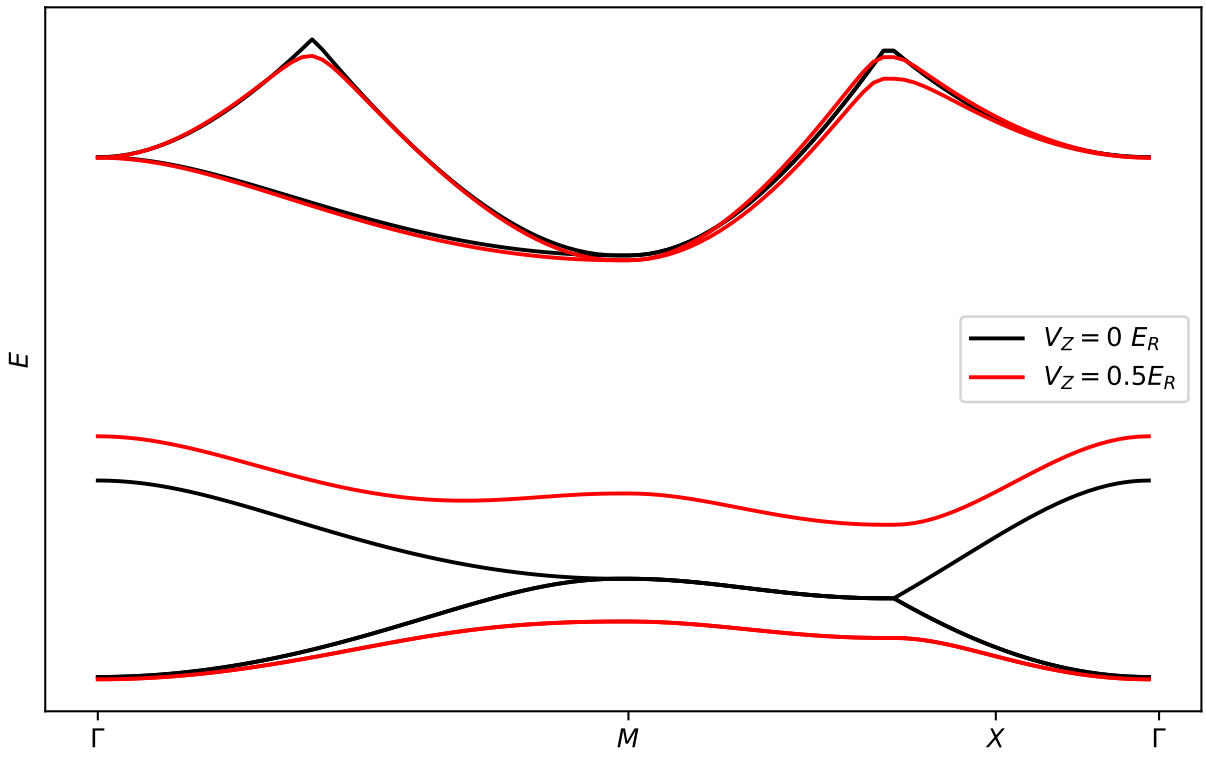

Figure 2.6: Lowest 4 bands for a 3Er lattice for the case of 0 Er out of plane lattice (black) and a 0.5 Er out of plane lattice (red).

2.8 Bose-Hubbard Model

We now revisit the Hamiltonian for atoms in an optical lattice. Taking the 1D situation with delta function interactions that are dominated by s-wave scattering, and an external lattice potential, Eq. 2.13 can be written as

$$\begin{aligned} H = \int dx\ \hat{\Psi}^\dagger(x) \left(\frac{-\hbar^2}{2m}\partial_x^2 + V_0 \sin^2(k_L x) \right) \hat{\Psi}(x) \\ + \int dx\ \frac{g}{2} \hat{\Psi}^\dagger(x) \hat{\Psi}^\dagger(x)) \hat{\Psi}(x) \hat{\Psi}(x) \end{aligned} \tag{2.40}$$

If the lattice potential is strong enough, we can make the tight binding approximation, where the field operators are expanded in a Wannier orbital for each band : $\hat{\Psi}^\dagger(x) = \sum_i w_i(x) b_i^\dagger$. Substituting into the above Hamiltonian results in the Bose-Hubbard Hamiltonian [35]:

$$H = -J \sum_{<ij>} b_i^\dagger b_j + \frac{U}{2} \sum_i n_i(n_i - 1) \tag{2.41}$$

The first term allows for hopping/tunneling of an atom from a site i to a site j. The $< i, j >$ notation indicates that the model accounts only for nearest neighbor tunneling, which has terms for an atom going from site i to $i \pm 1$. The second term is the interaction energy, which is the energy associated with having multiple atoms per site. The tunneling matrix element, J, is given as

$$J = \int dx\, w(x - x_j) \left(\frac{\hbar^2}{2m} \frac{d^2}{dx^2} + V(x) \right) w(x - x_i) \tag{2.42}$$

In the tight binding approximation, we can approximate the sinusoidal potential with a harmonic oscillator, and the on site wannier functions will tend towards the Hermite-Gauss solutions for the harmonic oscillator. Plugging in those basis states into the above equation, which converges at deeper lattice depths, the tunneling can be expressed as

$$J = \frac{4}{\sqrt{\pi}} E_R \left(\frac{V_0}{E_R} \right)^{3/4} \exp\left(-2\sqrt{\frac{V_0}{E_R}} \right) \tag{2.43}$$

This was seen in the previous sections on Optical Lattices, where the numerical band structures flattened out with a higher potential. In this model, a lower J corresponds to less energy needed to tunnel between sites and the wave function delocalizes over many lattice sites, and is known as the superfluid phase. In the limit that J gets large, the energy required to tunnel

becomes too large, so the atoms will localize to individual sites which is known as the Mott Insulating phase [36].

We can additionally calculate the on-site interaction as

$$U = \frac{4\pi\hbar^2 a_s}{m} \int dx |w_n(x)|^4 \approx \left(\frac{V_0}{E_r}\right)^{3/4}. \tag{2.44}$$

The ratio, J/U, can be controlled by changing the lattice depth, and can be used to observe the superfluid to mott-insulator phase transition [37, 38]. In optical lattices, the superfluid to mott-insulator (MI) transition can be seen through the coherence of time of flight images. In the superfluid phase, there is phase coherence in the system and snapping off the lattice will project the atoms onto plane wave components and diffraction peaks are seen. When the MI phase is approached, phase coherence is lost across sites and in the time of flight image, we just see a gaussian thermal cloud after time of flight. An example in our lab is shown below

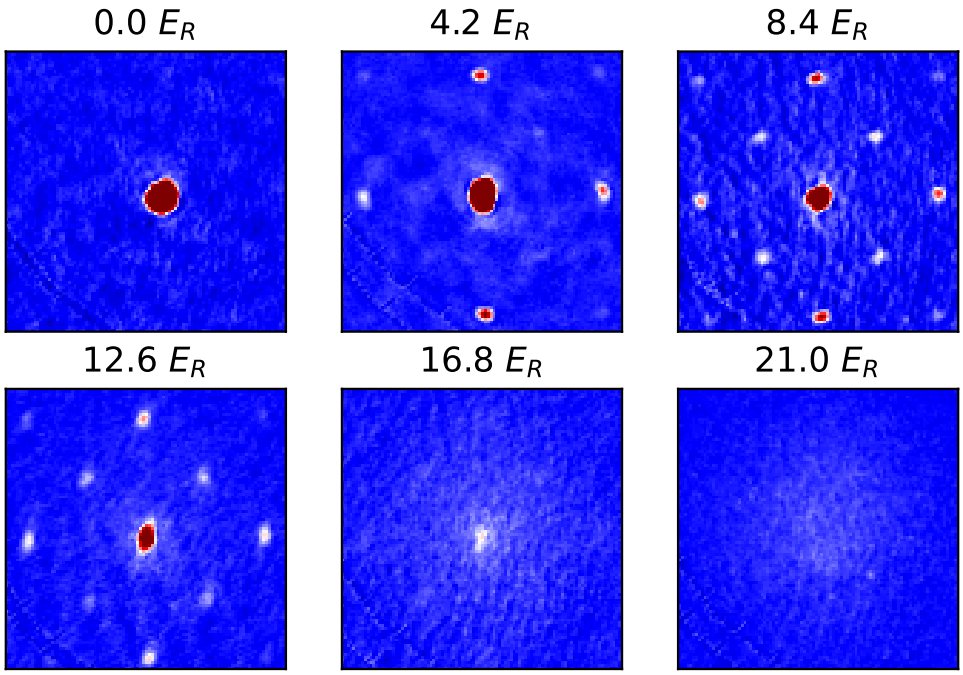

Figure 2.7: Time of flight images for atoms loaded into a variable lattice depth, held for 5ms then snapped off. As the depth is increased, we see an initial diffraction pattern due to the phase coherence. As we go past the transition, we note that the phase coherence is lost and the mott-insulator state is obtained. The presence of the additional diffraction peaks are due to experimental imperfections in the checkerboard lattice alignment.

2.8.1 Checkerboard Tight Binding

The Bose-Hubbard model from the previous section can be further extended to the 2D checkerboard lattice when we restrict ourselves to the lowest two bands of the system. The checkerboard lattice consists of double wells, which are offset in energy by Δ and there are two sites per unit cell, which we denote the a, b sites. Following the same convention as the Bose-Hubbard model (assuming non-interacting, $U = 0$) we can write the first order tight binding limit

as

$$H = -J \sum_i a_i^\dagger \left(b_{i+1} + b_{i+2} + b_{i+3} + b_{i+4}\right) + \Delta \sum_i a_i^\dagger a_i. \tag{2.45}$$

To calculate the band structure, we perform a Fourier transform, $a_i = \sum_q a_q e^{iqx}$ and the Hamiltonian is:

$$H = \Delta \sum_q a_q^\dagger a_q - J \sum_q a_q^\dagger b_q (4\cos(q_x/2)\cos(q_y/2)) + \text{H.C.}, \tag{2.46}$$

This is a 2x2 matrix in the a, b basis, which can be diagonalized to give the tight binding energy bands:

$$E = \frac{\Delta}{2} \pm \frac{\sqrt{\Delta^2 + 64J^2\cos^2(q_x/2)\cos^2(q_y/2)}}{2}. \tag{2.47}$$

The tight binding model can be interpreted as a fit to the exact band structure. To first order, we can see that the ground band does not capture the curvature along the band edge, as shown in Fig. 2.8. As a reference, the exact calculation in the figure is calculated with a total lattice depth of $5E_R$, where $0.5E_R$ ($\approx$ 1.7 kHz) is out of plane, which results in a $q = 0$ gap splitting of 3.2 kHz and an approximate value of J being 80 Hz (taken as 1/4 the total width of the ground band). The resulting best fit for the tight binding gives $J \approx 210$ Hz and $\Delta \approx 2.4$ kHz.

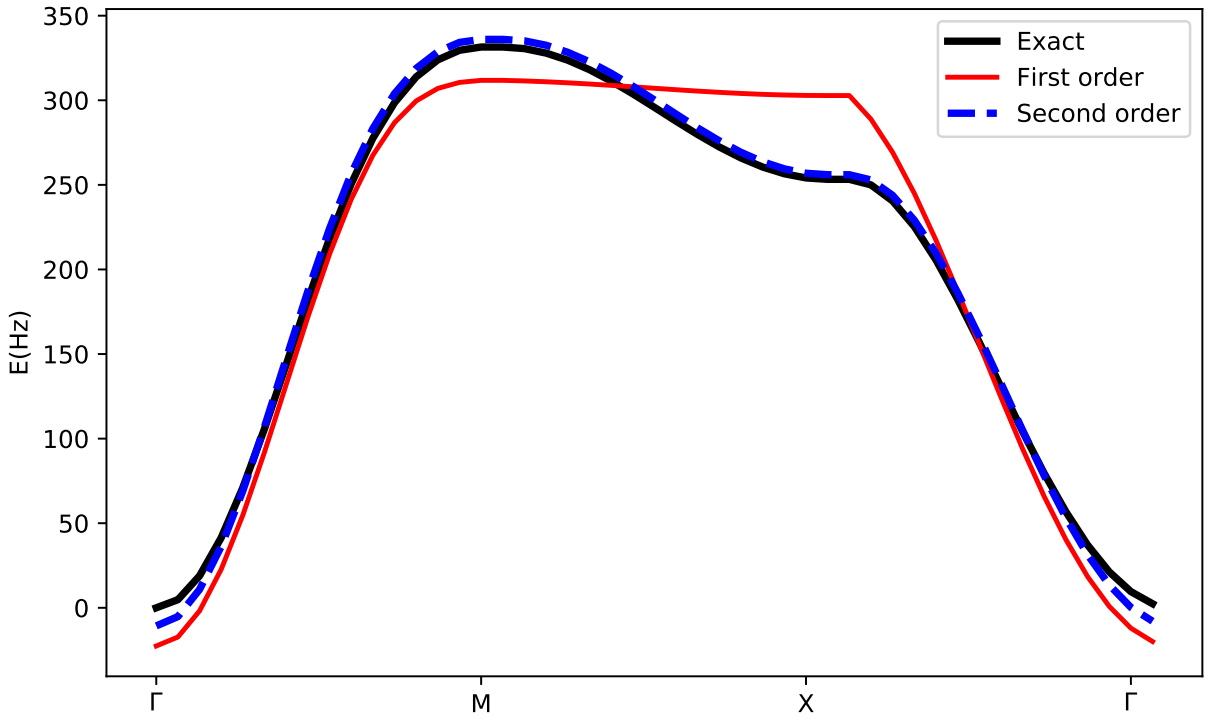

Figure 2.8: Comparing Tight Binding to the full plane wave band structure using only nearest neighbor tunneling. The first order tight binding model appears flat along the band edge and does not completely capture the band, whereas the inclusion of next nearest neighbor tunneling captures the band dynamics very well.

One of the key features of the first order tight binding is that the bands are flat along the edge of the Brillouin zone. In order to see a more qualitative match, we can add in the next nearest neighbor tunneling. This $J_a(J_b)$ term allows for tunneling between an a (b) site and any of the 4 next nearest neighbors, e.g. $H_{NNN} = J_a \sum_{j=1}^{4} a_i^\dagger a_j$. After Fourier transforming the Hamiltonian into momentum space, we end up with a 2x2 matrix for each q:

$$H_2 = \begin{bmatrix} \Delta - 4J_a \cos((q_x+q_y)/2)\cos((q_x-q_y)/2) & -4J\cos(q_x/2)\cos(q_y/2) \\ -4J\cos(q_x/2)\cos(q_y/2) & -4J_b\cos((q_x+q_y)/2)\cos((q_x-q_y)/2) \end{bmatrix} \tag{2.48}$$

The resulting band structure has fourier components along the diagonal axes ($q_x \pm q_y$), which results in the curvature along the band edge that is seen through the exact diagonalization in the plane wave basis. Figure 2.8 shows that even including the second term is enough to approximate the system.

2.9 Artificial Magnetic Fields on a Lattice

The Hubbard model was initially introduced to describe electrons hopping on a lattice. If we treat our Bose-Hubbard system as a charged particle and add in a magnetic field, which is given by the curl of a vector potential, $B = \nabla \times A$, then when the charged particle tunnels from one site to another, it will acquire an Aharanov-Bohm type phase given by $\phi^i_{m,n} = -eA^i_{m,n}$. In the tight binding language, we refer to this phase as the Peierls phase, [39]. The non-interacting tight-binding Hamiltonian can then be expressed as

$$H = -J \sum_{n,m} \left(e^{i\phi^x_{n,m}} a^\dagger_{n+1,m} a_{n,m} + e^{i\phi^y_{n,m}} a^\dagger_{n,m+1} a_{n,m} + \text{H.C} \right) \tag{2.49}$$

A particle that tunnels along a closed loop of one lattice plaquette will acquire a net phase of

$$\Phi = \phi^x_{n,m} + \phi^y_{n,m+1} - \phi^x_{n+1,m} - \phi^y_{n,m} = 2\pi\alpha, \tag{2.50}$$

where the - sign comes from tunneling in the conjugate direction. This phase, Φ, is the flux per unit cell and in the electron/lattice case, the quantity α represents the flux in units of the magnetic flux quanta, h/e.

This phase is assumed to come from the charged particle, but if we extend this to a neutral

particle, then there would be no interaction with the vector potential. The phenomena of an artificial magnetic fields arise when we artificially generate complex tunneling coefficients in the Hamiltonian, as has been demonstrated using raman transitions, or in the case of this thesis, lattice shaking. These techniques result in an atom that tunnels between sites acquiring a phase, so while there is no charge, it acts as if it were a charged particle moving in a magnetic field.

2.9.1 Harper-Hofstadter Hamiltonian

Since we are dealing with an equivalent vector potential, we are, in principle granted the freedom of a gauge choice. The observables, such as energy spectrum and average momentum, are gauge independent, so we can select what suits the system. A typical choice is the Landau gauge, where we only allow for complex tunneling in one direction, namely $\phi_{n,m} = (-\Phi n, 0)$, which has a magnetic field acting along z. In this gauge, the Hamiltonian is

$$H - J \sum_{n,m} e^{-i\Phi n} a^{\dagger}_{n+1,m} a_{n,m} + a^{\dagger}_{n,m+1} a_{n,m} + \text{H.C.} \tag{2.51}$$

The single particle energy spectrum of this model as a function of the flux, α, results in the Hofstadter butterfly [22]. When the flux is a rational fraction, $\alpha = p/q$, the resulting energy structure results in q different subbands, and there is a magnetic brillouin zone, which is q times larger than the lattice cell.

For our artificial field lattice system, the fact that we can turn on and off the gauge field means that the system is in fact not gauge independent. Projective measurements that arise when snapping off the modulation generating the gauge field, depend on the effective gauge of the experiment.

2.10 Periodically Driven Optical Lattices

In order to simulate Floquet physics in an optical lattice, there are various techniques used, including lattice shaking and lattice amplitude modulation. Lattice shaking is performed by periodically displacing the lattice, either through a frequency shift in the lattice light or through a physical displacement of a mirror (typically using a piezoelectric device), whereas amplitude modulation is just changing the lattice power using AOMs or other electronics. While the two techniques result in different effective Hamiltonians, the coupling between lattice bands differs in each scenario.

In these sections, I describe some theoretical treatments of Floquet problems, which are highlighted through different example systems.

2.10.1 Tight Binding Floquet Treatment

As previously discussed, cold atoms in an optical lattice can be treated with the use of a tight-binding model, where we start with a kinetic Hamiltonian: $H = -J\sum_{\langle i,j\rangle} a_i^\dagger a_j$. In the tight-binding Floquet treatment, we start with this kinetic Hamiltonian and add in an additional, time-periodic term. We then find a unitary transformation that can be applied, which rotates out the time dependent component.

Time Dependent Force

Before considering the Floquet treatment of performing a unitary transformation, we start with a simple, intuitive picture in this tight-binding model. In the presence of a time dependent force, $F = K\sin(\omega t)$, q changes based on the semi-classical equation of motion, $\dot{q} = F$. At a given time, the quasimomentum can be expressed as $q = q_0 + F\sin(\omega t)/\omega$ [40]. If the frequency

is fast enough that we can approximate the dynamics with the time averaged dynamics, and recalling that the tight-binding dispersion was given by $E = -2J\cos(q)$, we obtain an effective Hamiltonian

$$H_{\text{eff}} = -2J\frac{1}{T}\int_0^T \cos(q_0 + \frac{K}{w}\sin(\omega t))dt = -2J\mathcal{J}_0(K_0)\cos(q), \tag{2.52}$$

where $\mathcal{J}_n$ is the nth order Bessel function, and a scaled driving strength, $K_0 = K/\omega$ has been introduced. This scaled hopping amplitude is typically referred to as the effective tunneling, $J_{\text{eff}} \equiv J\mathcal{J}_0(K_0)$. The effective band structure is plotted for different drive strengths in Fig. 2.9. When the drive strength reaches 2.4, the band flattens as a result of the Bessel function being 0, and beyond that point, $\mathcal{J}_0$ is negative, so the band inverts, making $q = 0$ the maximum point.

The fact that the effective time averaged dispersion can become flat is known as dynamic localization (coherent destruction of tunneling) and has been shown to occur in cold atom systems [41, 42, 43]. Due to the lower effective J, this Floquet shaking has been used to realize the Mott insulator to superfluid transition [44].

Tilt Modulation

The next case to consider is a double well system, where there are two sites, A and B, with tunneling J and an offset Δ (taken to be on B). We take $\Delta >> J$ and assume there is no tunneling between A and B sites. The Hamiltonian is

$$H_0 = -J\sum_i a_i^\dagger b_i + b_i^\dagger a_i + \Delta\sum_i b_i^\dagger b_i, \tag{2.53}$$

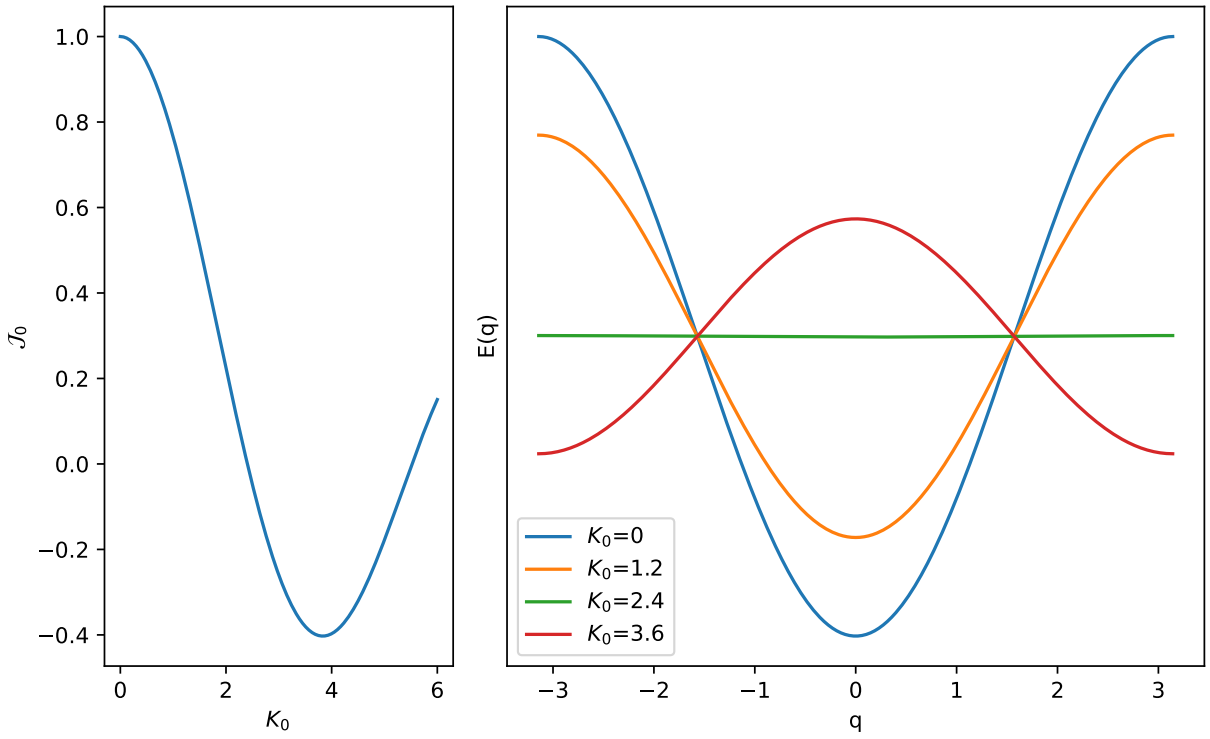

Figure 2.9: Left: $\mathcal{J}_0(K_0)$. Right: Modification of the effective band structure for different K_0. For certain ranges of the drive strength, the band inverts and the minima of the band structure is at the edge of the band.

which can be rewritten in matrix form as

$$H_0 = \sum_i (a_i^\dagger b_i^\dagger) \begin{pmatrix} 0 & -J \\ -J & \Delta \end{pmatrix} \begin{pmatrix} a_i \\ b_i \end{pmatrix} \tag{2.54}$$

Diagonalizing the system gives 2 energies separated by

$$\delta E = E_+ - E_- = \sqrt{4J^2 + \Delta^2}. \tag{2.55}$$

We now allow for modulation of A sites, such that the Hamiltonian is time dependent, with frequency ω,

$$H(t) = H_0 + \alpha \cos(\omega t) a_i^\dagger a_i. \tag{2.56}$$

To analyze this system, we start by moving into a rotated frame to eliminate the total potential ($V(t) = \Delta\ b^\dagger b + \alpha \cos(\omega t) a^\dagger a$), which can be done by using the following rotation:

$$R = \exp\left(\frac{i\alpha}{\omega} \sin(\omega t) a_i^\dagger a_i + i\Delta t b_i^\dagger b_i\right) \tag{2.57}$$

Under this transformation, the new Hamiltonian is given by, $H_t = RHR^\dagger - iR\partial_t R^\dagger$ which will become

$$H_t = -J \exp\left(-i\Delta t + \frac{\alpha}{\omega} \sin(\omega t)\right) a_i^\dagger b_i + \text{H.C.} \tag{2.58}$$

In the case of resonant driving, $\omega = \Delta$, using the HFE, Eq.2.10, it can be seen that the transformed Hamiltonian only has an $H^{[0]}$ contribution, and the effective Hamiltonian is given by (after using

the Jacobi-Anger expansion for Bessel functions)

$$H_{\text{eff}} = -J\mathcal{J}_1\left(\frac{\alpha}{\omega}\right) a_i^\dagger b_i + \text{H.C.} \tag{2.59}$$

Just like in the previous example, there is now an effective tunneling that takes the form of a Bessel function. When we take $\Delta = n\omega$, which is an n-photon resonance, the effective tunneling is given by the nth order Bessel function, $\mathcal{J}_n\left(\frac{\alpha}{\omega}\right)$. The presence of the drive increases the effective tunneling (at low enough α/ω) and can be interpreted as allowing tunneling through absorption of a drive photon. Note that this is the lowest order term in the expansion, which reintroduces coupling between A and B sites. Higher orders in the expansion can be calculated, and are actually necessary in some systems to introduce topological gaps in energy bands [45].

2.10.2 Trotter Method

The previous section introduced two interesting aspects of Floquet engineering in tight binding systems, dynamic localization and renormalization of tunneling, which were solved analytically. In this section, I will describe the Trotter Method for calculating band structures in the Floquet picture. I apply this to an optical lattice subject to amplitude modulation, where the intensity of light seen by the atoms is periodically modulated.

For an amplitude modulated lattice, the Hamiltonian is given by

$$H_{AM} = \frac{p^2}{2m} + (1 + \alpha\sin(\omega t))\, V_{\text{LAT}} = H_0 + H'(t), \tag{2.60}$$

where H_0 is the same static Hamiltonian as previously discussed, and there is now a time de-

pendent contribution $H'(t)$. In section 2.7.2, H_0 was solved in the plane wave basis, and is the starting point for this method. The time evolution operator can be expressed as

$$U(T) = \exp[-\frac{i}{\hbar}\int_0^T (H_0 + H'(t'))\, dt']. \tag{2.61}$$

To numerically calculate this, we break the integral into a discretized product of N steps, where $T = N(\Delta t)$, $U(T) = U_N U_{N-1} \dots U_2 U_1$, with $U_i = \exp[-i(\Delta t)H(t_i)/\hbar]$. The Trotter-Suzuki expansion allows us to expand this as [46]

$$\begin{aligned}\exp[-i(\Delta t)H(t_i)/\hbar] \approx \exp[-\frac{i}{2\hbar}(\Delta t)H'(t_i)] \exp[-\frac{i}{\hbar}(\Delta t)H_0] \\ \exp[-\frac{i}{2\hbar}(\Delta t)H'(t_i)].\end{aligned} \tag{2.62}$$

To calculate the quasi-energy spectrum, this time evolution is calculated in the plane wave basis and then diagonalized, which can then be used to extract the quasi-energy. One thing to note is that since all the energies overlap into a Brillouin zone structure, there are no "lowest energy states", and the labeling of states is not as straightforward as they were in the static case. In order to label, we work under the assumption that in the Trotter picture, the time dependent contribution is sufficiently small, so that it only slightly perturbs the initial states. We can label the Floquet bands by using the overlap of the static eigenvectors with the Floquet ones,

$$|\psi_i^f\rangle = \max_j |\langle \psi_j^f | \psi_i^s \rangle|. \tag{2.63}$$

Note that at sufficiently strong drives, the concept of a particular Floquet state arising from an undriven state loses meaning as the states become heavily mixed.

A sample band structure plot is shown in Fig. 2.10, which shows that the two static bands are dressed (the second band is shifted down by the drive frequency, ω), and the amplitude modulation couples the two bands, resulting in the structure shown in 2.10(b). This figure represents a cut along $q_y = 0$, and it is interesting to note that due to the symmetry of the problem, the full 2D band structure exhibits a ring structure, which is of interest in condensed matter fields [47].

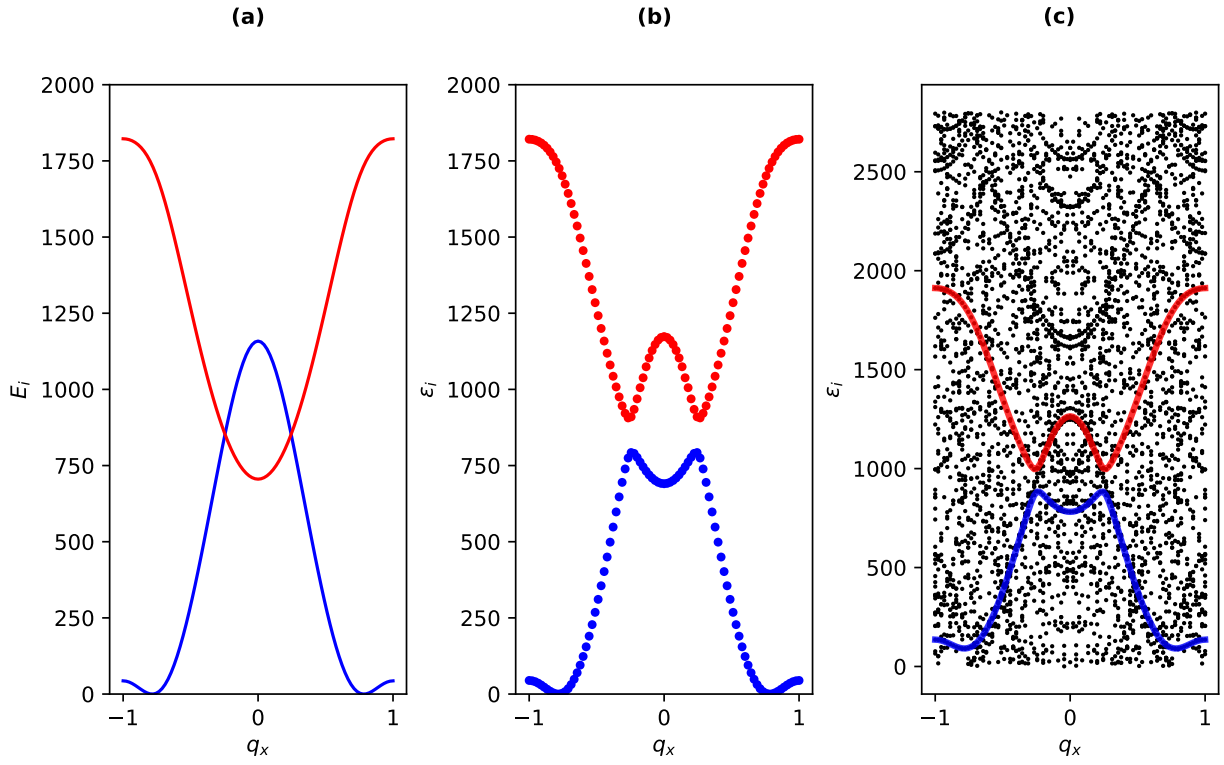

Figure 2.10: Band structure from trotter calculation for $\alpha = 0.12$, $\omega = 2800$ Hz. (a) shows the static bands, with the first excited band (blue) offset by ω. (b) shows the Floquet band structure for stated with maximum overlap with the two lowest bands in the system in the weakly coupled limit. (c) shows the full quasi-energy spectrum for all diagonalized basis states. The lowest two bands are indicated.

2.10.3 Extended Basis

I now present another technique for calculating the Floquet band structures, called the extended basis method. In order to describe this theoretical treatment, I apply it to the case

of a periodically displaced (shaken) lattice. I note that this problem can be solved using the Trotter method as well, but at higher drive amplitudes, the overlap and sorting of bands becomes problematic and computationally expensive.

For this example, the Hamiltonian can be written as

$$H_S = \frac{p^2}{2m} + V_{\text{LAT}}(x + \delta_x \sin(\omega t), y + \delta_y \sin(\omega_t + \phi), t), \tag{2.64}$$

where $V_{\text{LAT}}(x, y)$ is the time dependent lattice potential.

We now introduce the co-moving frame through the unitary transformation $U = \exp[-i\delta \cdot p/\hbar]$. Treating ψ_0 as the untransformed wavefunction, the following unitary transformation moves us into a co-moving frame, $\psi_{cm} = U\psi_0$. Plugging into the Schrödinger equation $i\dot{\psi} = H\psi$ one obtains the following Hamiltonian for the co-moving frame

$$H_{cm} = \frac{p^2}{2m} + V_{LAT}(x, y) - \omega \left(\delta_x \sin(\omega t)p_x + \delta_y \sin(\omega t + \phi)p_y\right) \tag{2.65}$$

We begin by recalling the eigenvalue problem for Floquet modes, Eq. 2.3 and define the quasi-momentum operator to be

$$\hat{Q} \equiv \hat{H}(t) - i\hbar\partial_t, \tag{2.66}$$

such that $\hat{Q}|\phi_{nm}\rangle = \varepsilon_{nm}|\phi_{nm}\rangle$, where the states and energies now are defined with two indices, n originating from the initial Hamiltonian, and m, related to the basis of time dependent periodic functions. In general, if $|u_n\rangle$ are solutions of the time independent Hamiltonian (such as a Bloch wave in the static lattice), then the form of the combined state in the extended basis can be

expressed as:

$$|\phi_{n,m}\rangle = e^{im\omega t}|u_n\rangle. \tag{2.67}$$

By denoting the $|\phi_{n.m}\rangle$, as $|n,m\rangle$, the matrix elements of this operator can be expressed as

$$\langle n'm'|Q|nm\rangle = \langle n'm'|H|n,m\rangle + \hbar m\omega t\delta_{nn'}\delta_{mm'}, \tag{2.68}$$

where the δ functions arise due to the orthogonality of the states for n and m. The first matrix element, $\langle n'm'|H|nm\rangle$ can be further decomposed

$$\langle n'm'|H|nm\rangle = \int_0^T dt\langle n'|H|n\rangle e^{i(m'-m)\omega t} = \langle n'|H_{m'-m}|n\rangle. \tag{2.69}$$

The expression $H_{m'-m}$ represents the fourier components of the co-moving Hamiltonian (2.65). Intuitively, it can be thought of as describing an 'm photon' transition, where we couple two n states that differ in energy by $m\omega$. Since our shaken Hamiltonian has a DC ($\omega = 0$) component, as well as a component at ω, the calculation will involve just two fourier components, and the quasi-momentum operator can be represented as a tri-diagonal block matrix.

$$Q = \begin{bmatrix} H_0 - \hbar\omega \otimes \hat{1} & H_{-1} & 0 \\ H_1 & H_0 & H_{-1} \\ 0 & H_1 & H_0 + \hbar\omega \otimes \hat{1} \end{bmatrix}. \tag{2.70}$$

The calculation of this matrix requires truncation of the time basis (how many m states), and there are some edge effects related to the truncation. For our parameter region, we tend to find that using $m_{\text{max}} = 5$ (11 total time "blocks") results in convergence of the eigenvalues. The

parameter that defines the coupling between the bands, α is given as the Fourier component of the co-moving Hamiltonian (2.65), which is the same as the dimensionless parameter K_0 from the tight binding picture. Figure 2.11 shows an example of the extended basis calculation in the case of a frequency that is less than the resonance condition between the two bands. In this calculation, the number of time basis states was taken to be 2, such that the calculation includes $[-2\omega, -\omega, 0, \omega, 2\omega]$. As shown in the figure, the bands repeat themselves, which can get intricate as the number of time states is increased. In order to isolate the relevant bands, the ground band is taken to be the one closest to the zero energy (where there is no frequency offsets and no coupling included). We note that there are additional levels repelling each other, even with states differing by more than ω which indicates that a tight binding model at high drive will not capture all relevant levels and a more complete description is necessary to understand the entire system.

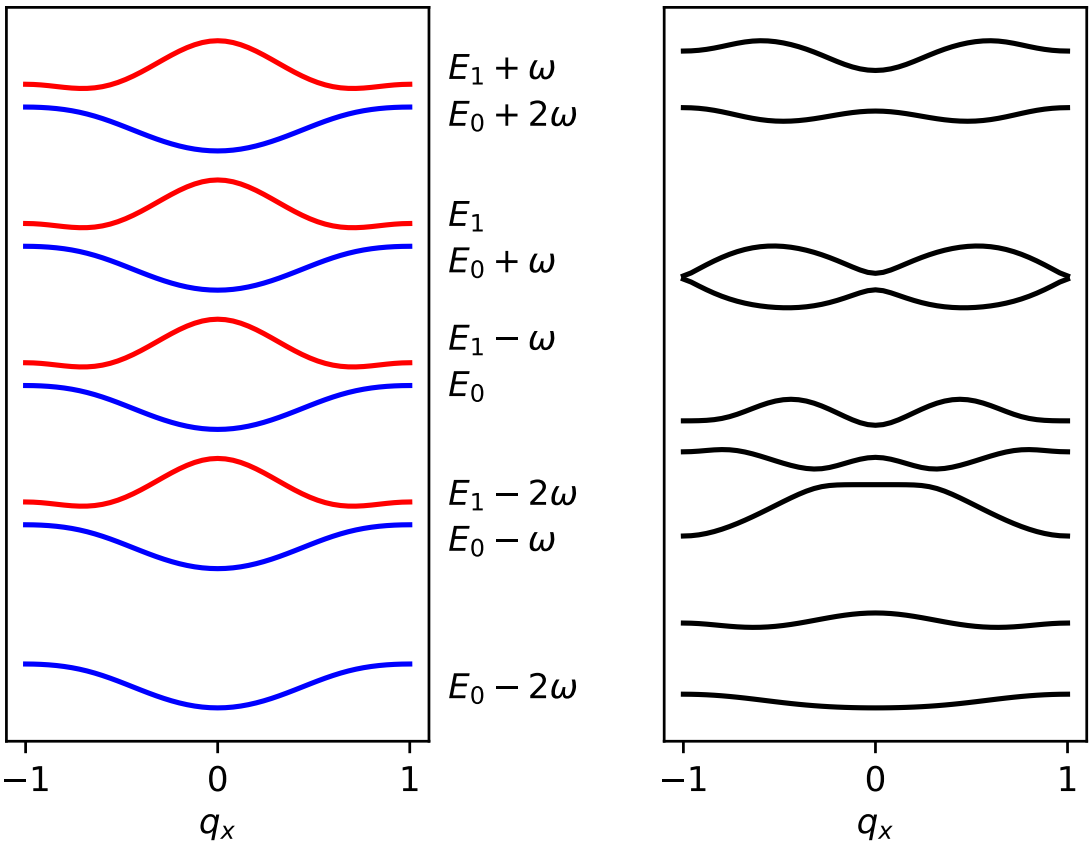

Figure 2.11: Sample bands for extended matrix calculation in the case of no coupling (left) and a coupling strength, α=2.2 (right), using a truncation of 2 time states. This shows the general repeating structure and how the coupling can act to couple different bands.

Chapter 3: Experiment

In this section, I will discuss the experimental apparatus designed for our optical lattice experiments. We employ standard magnetic and optical trapping techniques to trap an atomic cloud at sub-doppler temperatures. Bose-Einstein Condensation is achieved through RF evaporation of magnetically trapped atoms, followed by evaporative cooling in an optical dipole trap

Details about the experimental apparatus beyond the brief overview found here can be found in the PhD thesis of Roger Brown [48].

3.1 Vacuum System

3.1.1 Atom Source and Oven

Our vacuum system for the experiment consists of an oven chamber and a UHV chamber. The oven chamber contains a 5g rubidium source within a 1.33" conflat bellows, which is connected to the "bright wall", which is a 4" nipple kept at a higher temperature, designed to prevent migration of the Rb metal to that port of the oven. While operating, the oven is kept at 85 C, and the bright wall is kept at 105 C. The bright wall is connected to a standard spherical octagon chamber, which is attached to a Varian ion pump, which pumps at 125 L/s to achieve pressures in the low 10^{-10} Torr. The atomic beam is directed from the source to a pinch off tube

within the bright wall through a Uniblitz shutter, which is mounted to another pinch-off tube with a Swage-lok fitting, allowing for the atomic beam to be mechanically shuttered with an external TTL pulse. The final piece of the oven system is the cold cup, which is a copper piece thermally contacted through a special designed copper feed-through to a peltier unit on the outside of the vacuum chamber. The hot side of the peltier unit is water cooled and flushed with nitrogen, while the cold cup is kept at a temperature close to -18 C, which collects any of the atomic beam that is not collected through the pinch off tubes. A hole in the cold cup allows for a collimated atomic beam to pass through the cup and towards the main chamber. A pneumatic gate valve is used to separate the oven from the Zeeman slower, which directs atoms from the source to the UHV chamber.

3.1.2 UHV Side

The UHV chamber is another Spherical Octagon with 8 ports and 2 custom bucket windows, designed to allow for closer placement of magnetic coils and optics and is attached to a Varian ion pump (55 L/s), and an ion gauge. The top of the UHV chamber contains a titanium cartridge which is used for titanium sublimation pumping. In order to avoid coating the windows on the vacuum side, hand adjustable flags are installed that are rotated prior to pumping the titanium, which cover and protect the windows.

3.2 Magnetic Fields

The experimental apparatus uses a magnetic quadrupole trap, which is generated from a pair of anti-Helmholtz coils along the vertical axis. At the center of the trap, the magnetic gradient

is 1.05 G/A·cm while additional shim coils along all three directions provide a bias field and allows for the center of the quadrupole trap to be shifted in space. To allow for fast switching, the power supply for the quad coils, held at a constant 15V, capable of 440 A, is controlled using a water cooled MOSFET bank, capable of switching the current in ≈ 1 ms. The water cooling is interlocked to the current supply through flow switches, ensuring that the current supply is not on while the water is off.

3.3 Laser Systems

3.3.1 Cooling Light

Our experiment relies on the cooling and trapping of ^{87}Rb, specifically on the D_2 line. The relevant level structure is shown in Fig. 3.1. We initially lock our master laser to the crossover peak between the $|F = 2\rangle \rightarrow |F' = 2\rangle$ and $|F = 2\rangle \rightarrow |F' = 3\rangle$ using saturated absorption spectroscopy. The cooling light addressing the $|F = 2\rangle \rightarrow |F' = 3\rangle$ transition is beatnote locked to the master source. The master is also used to beatnote lock the repump laser to the $|F = 1\rangle \rightarrow |F' = 2\rangle$ transition. The cooling and repump locking systems are both controlled by voltage controlled oscillators, which can be dynamically adjusted during an experiment and the intensity of the light being sent to the experiment are controlled through AOMs. Additional mechanical shutters allow for total blocking of light to the experiment.

3.4 Microwave and RF

In the presence of a magnetic field, the hyperfine states will split into $2F+1$ zeeman levels, meaning that the $5S_{1/2}$ level splits into 8 different zeeman levels, 3 from the $F = 1$ and 5 from

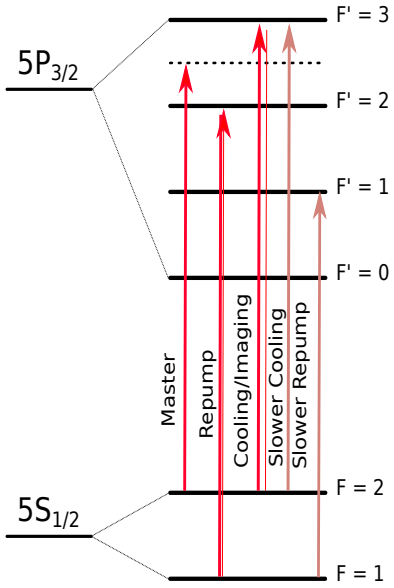

Figure 3.1: ^{87}Rb levels used for cooling and trapping.

the $F = 2$. The initial magnetic trapping of the BEC results in a pure $|F = 1, m_F = -1\rangle$ condensate. The splitting between the F = 1 and F = 2 without the zeeman sublevels is $\approx$ 6.8 GHz, a frequency in the microwave regime. The use of microwaves allows for control over the internal state of our atoms.

In order to reach a frequency of 6.8 GHz, we start with a Rhode and Schwartz frequency synthesizer, which generates 13 dBm of 3.438 GHz microwaves. The signal is frequency doubled and then mixed with an RF signal generated from a DDS device and sent to an amplifier, which then passes through a stub tuner and then to a homemade copper horn. A TTL switch before the amplifier allows for fast switching and control during experimental sequences.

The frequency seen by the atoms is controlled by the output of the RF signal from the DDS. An example microwave spectroscopy is shown for the $|F = 1, m_F = -1\rangle \rightarrow |F = 2, m_F = -2\rangle$ transition with a 155 μs pulse. These spectra are fit to the standard Rabi formula (3.1) for a two level system, where the only free parameters are the center frequency and the coupling strength.

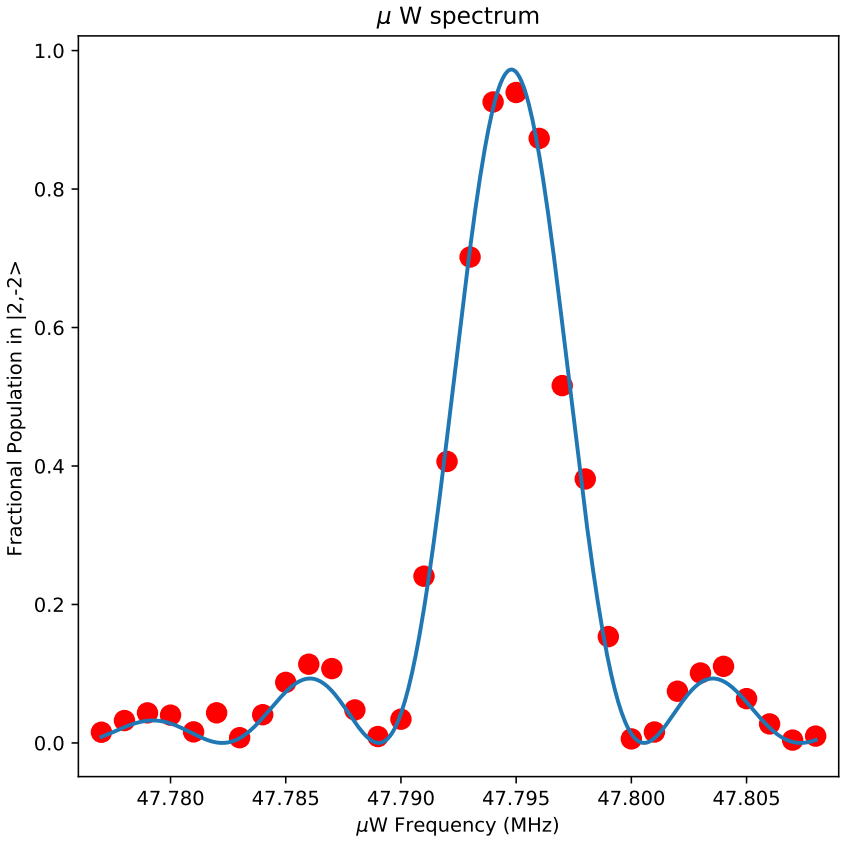

Figure 3.2: Typical μW spectrum for the $|F = 1, m_F = -1\rangle \rightarrow |F = 2, m_F = -2\rangle$ transition. The frequency is the value sent from the DDS device to be mixed with our microwave source.

$$Pop(\omega; \Omega, \omega_0, T_{pulse}) = \frac{\Omega^2}{\Omega^2 + (\omega - \omega_0)^2} \sin^2\left(\pi T_{pulse} \sqrt{\Omega^2 + (\omega - \omega_0)^2}\right) \tag{3.1}$$

3.5 Imaging

The experiment has two different imaging options. The first is a Point Grey Flea3, which is set up to image perpendicular to direction of gravity. The second camera, a Princeton Images PIXIS, is set below the atoms, allowing for analysis of the x-y plane after a time of flight (typically 27 ms).

Our images are obtained through standard absorption imaging. We take 3 sequential im-

ages: probe with atoms (ATOMS), probe with no atoms (NO_ATOMS) and then a background (BG), which has no probe light. Using Beers law, which states the absorbance scales as $I(z) = I_0 \exp(-ODz)$, we obtain the optical depth as

$$OD = -\ln\left(\frac{\text{ATOMS-BG}}{\text{NO\_ATOMS-BG}}\right) \tag{3.2}$$

3.6 Computer Control

The experimental sequences are programmed through Setlist, which is an in-house LabView-based program that is responsible for generating the desired ramps and triggers. Analog/digital outputs are generated through National Instruments DAQ devices, which communicate to our Setlist through the National Instruments DAQmx driver. Calculations of ramp values are done on the backend, either through LabView or MatLab.

3.7 Optical Lattice

The optical lattice is formed in a bow tie configuration, resulting in a 4-beam lattice as shown in Fig. 3.3, which is a single beam retroreflected back on itself. The light is produced by a tunable MBR Ti-Saph laser, which is pumped with a 10 W Verdi (532 nm) and fiber coupled from a separate optical table to the experimental apparatus. An adjustable waveplate allows for adjustment of powers between the 2D optical lattice and the vertical optical lattice.

The bowtie configuration is used due to its phase stability, despite having more than 3 (2D+1) beams. Any phase noise will act on all four beams simultaneously, resulting in a total displacement of the lattice, with no change to the lattice unit cell structure. Our setup uses two

Pockels cells, which are electro-acoustic modulators (EOMs) that change the polarization of light based on the voltage that is applied to the crystal. For our lattice setup, light in the x-y plane will result in a 2D lattice with spacing $\lambda/2$, whereas light out of the plane (z direction) results in a 2D lattice with spacing λ. The total lattice seen by the atoms will be the combination of these two lattices, as discussed in section 2.7.2. Computer control of the voltage on the input Pockels cell sets the ratio of in-plane and out of plane light. The voltage applied to the 2D Pockels cell translates the position of the out of plane lattice, allowing for different lattice geometries and double well structures.

In order to precisely control the intensity of the lattice beams, a small amount of light is picked off after the fiber and sent to a photodiode. The photodiode signal is sent to the DDS device, which has digital feed back circuitry to stabilize the lattice AOM at the desired (dynamically adjustable) amplitude.

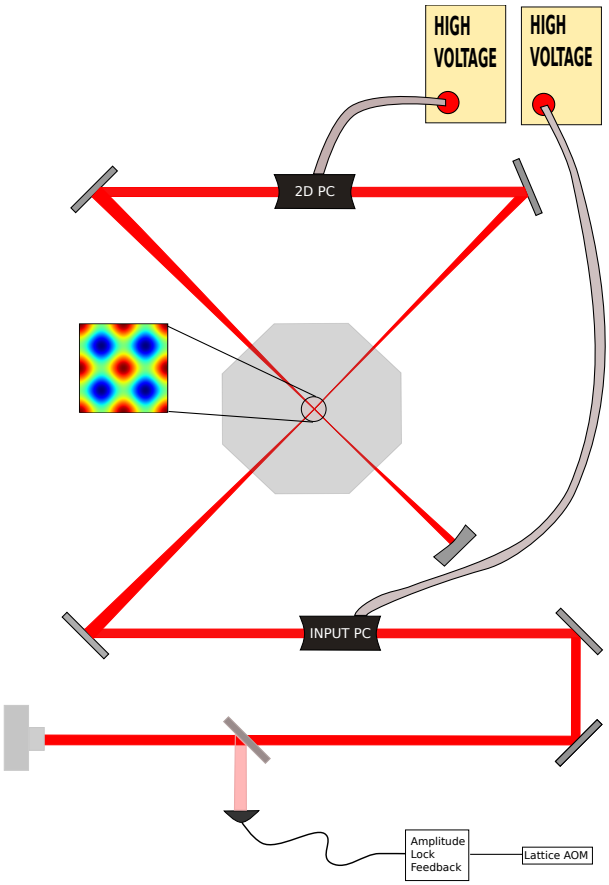

Figure 3.3: Experimental configuration of the bowtie optical lattice.

3.7.1 Optical Lattice Calibration

In order to calibrate the depth of our optical lattice, we perform a standard Raman-Nath diffraction pulse [49]. The Raman-Nath approximation is valid for the case when the lattice pulse time, t, is shorter than the approximate harmonic oscillation period for the lattice, which is a valid assumption for our lattice depths of up to $50E_R$ and pulse times of $2\mu s$. After pulsing the lattice of depth V_0 for a time t, the relative population of atoms that are transferred to the 1st

order diffraction peak can be approximated as

$$P_1/P_0 = \frac{\mathcal{J}_0(V_0 t/2)}{\mathcal{J}_1(V_0 t/2)} \tag{3.3}$$

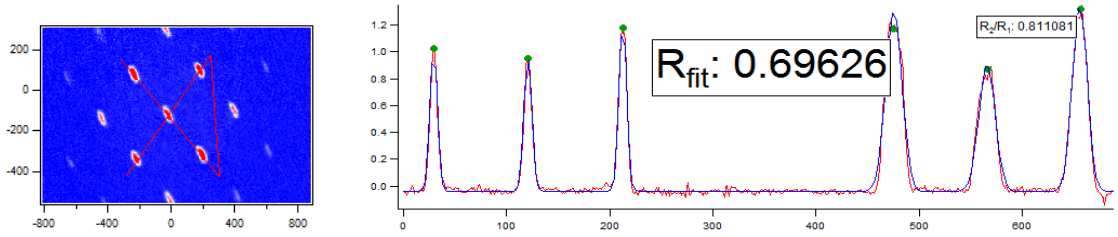

Figure 3.4: Example image of lattice diffraction as well as a cross-section indicating the relative populations in the first order. In this image, the imbalance between the cross-sections along the diagonals indicates that there are slightly different depths along the x and y directions. This can be due to slight alignment imperfections or power imbalances.

Figure 3.4 shows a sample image of lattice diffraction as well as the line profile of the atomic peaks after diffracting the lattice on for $2\mu s$. The resulting integrated peak magnitudes give the relative populations (the R fit value gives the relative population in the first order). By solving this value for Eq. 3.3, we find that this particular run gave a lattice depth of approximately $72E_R$. By combining this with the signal on the photodiode, this gives a reference for lattice intensity as a function of voltage, which we can control for experimental runs.

3.7.2 Tilt Calibration

In order to calibrate the offset between the checkerboard sublattices, we follow the technique described in [34]. For a checkerboard lattice with an offset Δ between neighboring sites, the potential is ramped on in a time that is adiabatic with respect to vibrational spacing, but not

adiabatic with respect to tunneling in the lattice. For our experiment, we ramp on the lattice to a depth of $30E_R$ in $200\mu s$, which loads into both sublattices, even though the ground state for large tilts has atoms in one sublattice. The wavefunction is therefore a combination of atoms occupying both sublattices and the different sublattices acquire a phase Δt. By holding the atoms in the lattice for a variable time, the phase of the wavefunction in the sublattices oscillates, giving rise to oscillations in the amplitude of the diffraction peaks. We fit the visibility between the diffraction peaks to a damped sine wave, from which we can determine the tilt between neighboring sites.

The tilt calibration procedure is typically done with large lattice depths of $30E_R$, which results in a frequency fast enough to measure before thermalization occurs and interaction induced phase coherence is lost. In order to extrapolate the measured tilts, we assume a linear scaling of tilt with the lattice intensity, which is an approximation, as single particle tunneling and mean field effects in the lattice can result in slightly different tilts (we find that these higher order effects are small, and the tilts agree with values obtained through parametric spectroscopy techniques, to within experimental accuracy). We also note that this is for a BEC prepared at $q = 0$ meaning that in the band picture, this gives the $q = 0$ gap and does not contain any information about the bandwidths or gaps at non-zero q.

3.8 Tripod Piezo Mounts

The primary physics in this thesis relies on periodically shaking, or modulating the position of the optical lattice. Given the bowtie lattice geometry is a single retro-reflected beam that is phase stable, using a scheme such as modulating an AOM to adjust the frequency of one arm would not work. The shaking performed relies on physically modulating the position of the

lattice by moving the mirrors as shown in Fig. 3.5.

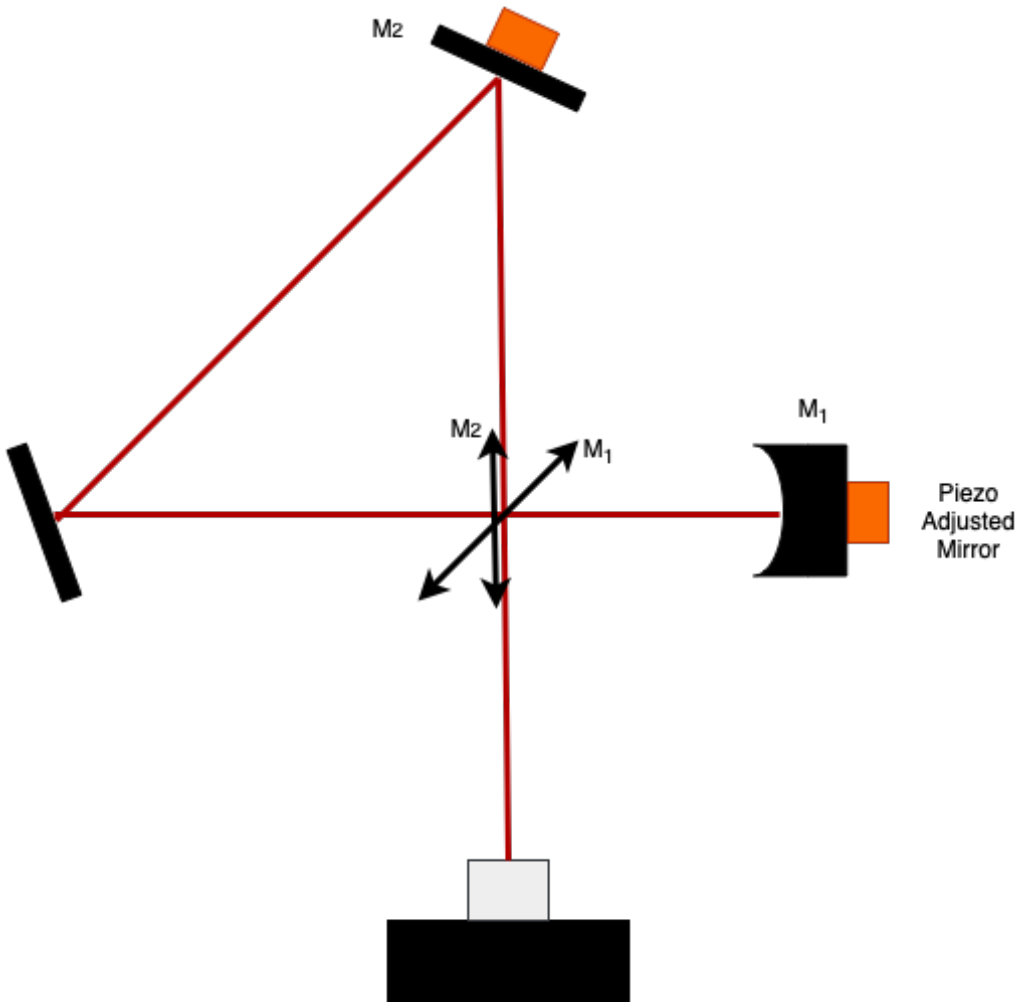

Figure 3.5: Schematic showing the position of the two tripod piezos. The linear combination of the two displacements results in an arbitrary displacement of the lattice. The arrows indicate the lattice motion resulting from shaking the associated piezo mirror.

3.8.1 Lattice Displacement

Flat Mirror

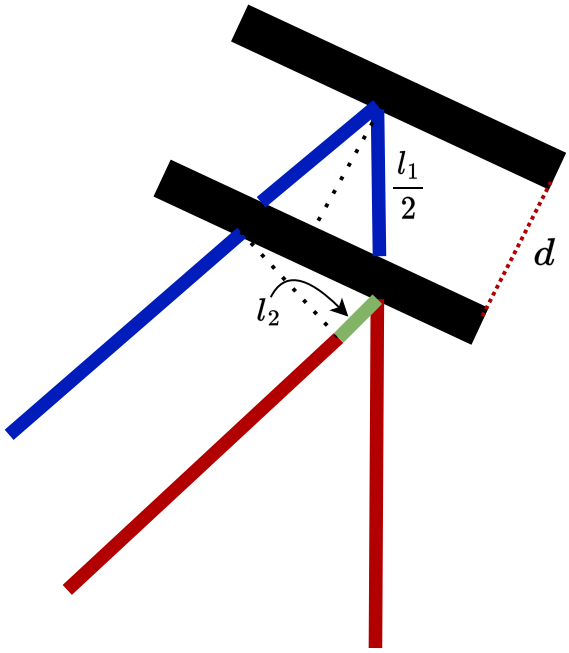

Figure 3.6: Geometry of flat mirror displacement. When the piezo moves a distance d, the initial optical path, as shown in red, gets an additional phase from the optical path $l_1 - l_2$.

When moving the flat mirror (M_2), the path length can be seen in Fig. 3.6. After moving a distance d, the total path length is given by $\Delta\ell = \ell_1 - \ell_2$, where

$$\ell_1 = \frac{2d}{\cos(\pi/8)} \tag{3.4a}$$

$$\ell_2 = 2d\sin(\pi/8)\tan(\pi/8) \tag{3.4b}$$

The total path length after a displacement, d, of the mirror is given by

$$\Delta\ell = 2d\cos(\pi/8). \tag{3.5}$$

In the four beam lattice, k_1 is unaffected, k_2 and k_3 acquire a phase $\phi = k\Delta\ell$ and k_4 acquires 2ϕ. The total intensity (recalling $k_{1/2} = -k_{3/4}$ and $|k_i| = k$) is given by:

$$I(x,y) = |\hat{x}\left(e^{ik_2x+i\phi} + e^{-ik_2x+i\phi}\right) + \hat{y}\left(e^{ik_1y} + e^{-ik_1y+2i\phi}\right)|^2 = 4 + 2\cos(2kx) + 2\cos(2ky + 2\phi) \tag{3.6}$$

In terms of the mirror displacement, the intensity is

$$I(x,y) - I_0 = 2\cos(2kx) + 2\cos(2k(y + 2d\cos(\pi/8))) \tag{3.7}$$

Periodically shaking the flat mirror translates the lattice along the y direction (direction of k_1/k_4 lattice) and the physical displacement is $2d\cos(\pi/8)$.

Retro Mirror

The geometry for the retro mirror (M_1) is a bit simpler. Since the beam is normally incident, when the mirror is moved by a distance d, the path difference is $2d$ and the phase is $\phi = 2kd$. In this case, k_1 and k_2 are unaffected, while k_3 and k_4 each acquire an additional phase ϕ. The total intensity is

$$I(x,y) = |\hat{x}\left(e^{ik_2x} + e^{-ik_2x+i\phi}\right) + \hat{y}\left(e^{ik_1y} + e^{-ik_1y+i\phi}\right)|^2. \tag{3.8}$$

After some algebra, this becomes

$$\begin{aligned} I(x,y) - I_0 &= 2\cos(2kx - \phi) + 2\cos(2ky - \phi) \\ &\rightarrow (\cos(2k(x-d)) + \cos(2k(y-d))) \end{aligned} \tag{3.9}$$

This shows that displacing the mirror will result in the lattice moving along the (x+y) direction.

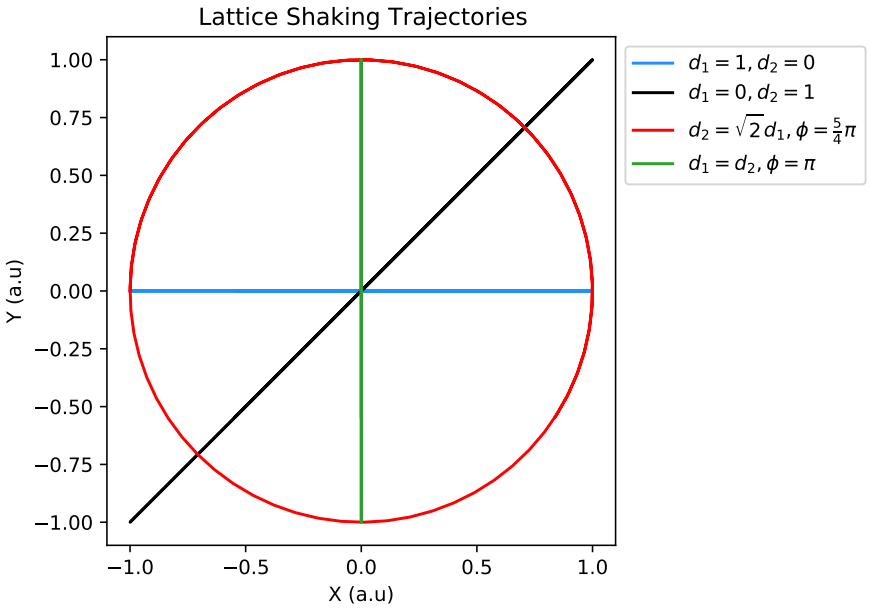

Figure 3.7: Shaking trajectories for different mirror driving parameter combinations.

Combined Shaking

Given the geometry of the lattice, we are unable to decouple the mirror shaking into two orthogonal dimensions. In this section we look at the form of the shaking needed to produce a circular trajectory. When the flat mirror is moved a distance d_1, the lattice is translated a distance $\delta_1 = 2d_1 \cos(\pi/2)$ along the y direction. The retro mirror, when translated a distance d_2, results in a lattice displacement of $\delta_2 = d_2$ along x and y. If both are periodically varied, $d_i = d_i \cos(\omega t + \phi_i)$, the total displacement of the lattice can be expressed as (setting $\phi_1 = 0$ without loss of generality)

$$\begin{bmatrix} x(t) \\ y(t) \end{bmatrix} = \begin{bmatrix} \delta_1 \cos(\omega t) + \delta_2 \cos(\omega t + \phi) \\ \delta_1 \cos(\omega t) \end{bmatrix} \tag{3.10}$$

The position of the lattice in 2D can be arbitrarily set, and Fig. 3.7 shows a set of different

parameters that can be used to create different 2D trajectories. Circular shaking, which is particularly of interest, requires a relative phase of 1.25π between the two shaking of the two mirrors with a ratio of the displacement amplitudes of $\delta_2/\delta_1 = \sqrt{2}$.

3.8.2 Design

To perform the shaking, we designed a translatable mirror, which consists of three individually controlled piezo actuators in a tripod configuration. This design was the focus of the 2018 paper, [50], and was inspired based on interaction with the Esslinger group. The use of three piezos in the tripod configuration instead of a single one allows for control of steering errors, which can become important when dealing either with sensitive systems, such as cold atoms, or in setups where there are long optical paths, and slight angular deviations can result in large physical displacements of the beam. It was found by experience that the use of a single piezo mounted to a mirror would result in a tilt as well as a displacement, resulting in undesired steering.

The system design can be seen in Fig. 3.8. Our design consists of a steel "bullet" which has a mass of $310g$, designed to be a mechanical insulator and remove low frequency resonances. The choice of steel in lieu of potentially heavier materials such as tungsten, was made as a compromise between density, cost and ease of machining. The backside of the steel support is cut such that it can be placed into a standard 1-inch optical mount, a requirement for fine-tuning the beam direction. We include a thin 1 mm, ceramic disk onto the face of the steel bullet, to act as an electrical insulator between the piezo and the steel. The piezos are Noliac NAC2012, which are 3 mm x 3 mm in size, have a capacitance of 65nF, and a maximum displacement of $3.3\mu m$. The three piezos are epoxied to the ceramic insulator in a tripod configuration with a standard Loctite

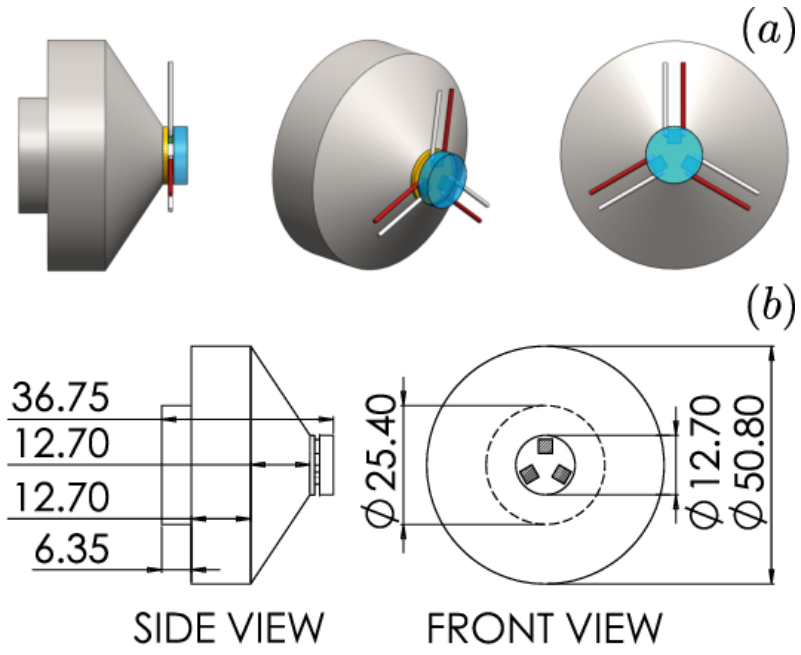

Figure 3.8: Design of the tripod mirror system. (a) shows the heavy steel "bullet" design that fits into a standard mirror mount. There is a small ceramic layer in between the steel and piezo. (b) shows the technical specs of the steel bullet.

epoxy from any hardware shop and the other side of the piezos were then epoxied to the mirror. In an effort to make sure that the epoxy was fully cured, the epoxying was done over different days. Each epoxy bond was given over 24 hours to cure, in order to make sure there was no free movement, which could introduce unwanted noise into the device.

The independent control of the piezo displacements needed to control the beam steering was provided by an electronic circuit that allows for the relative tuning of the three applied voltages based on a trimpot. By adjusting the trimpots, the relative fractional displacement can be adjusted, which allows for fine control of the reflected beam direction as the mirror is displaced.

The circuit is shown in Fig. 3.9.

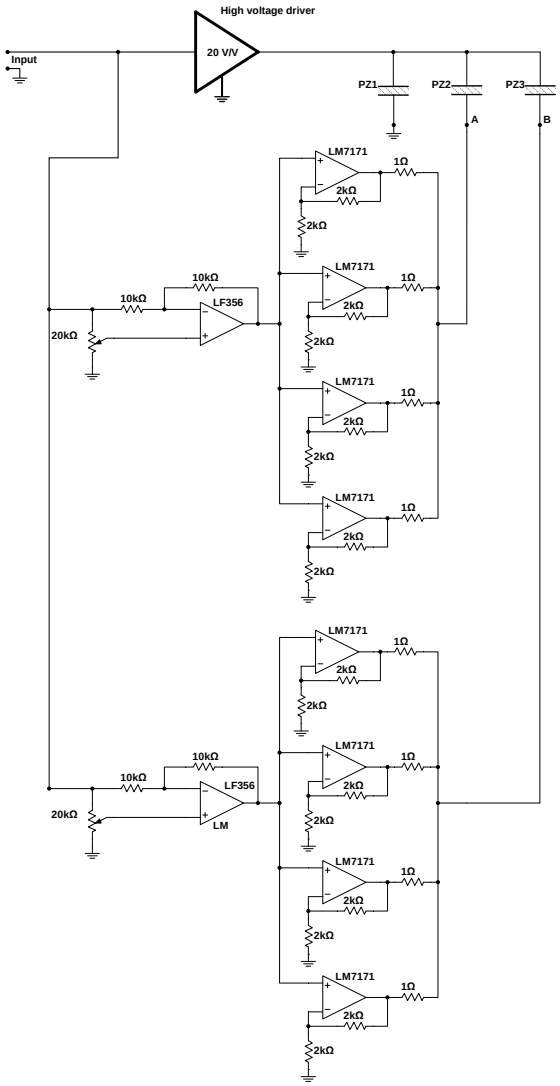

Figure 3.9: Electronics board for controlling the three tripod piezos. After the High Voltage Amplifier, which gives a 20 V/V amplification, the fractional signal to each of the individual piezos is controlled by the value of individual trimpots on the board.

3.8.3 Piezo Characterization

Frequency Response

Given that the typical energy scales of cold atom systems are in the kHz range, it is desirable

that the piezo design works in this range, with up to 20kHz response bandwidth being our goal. To test the frequency response of the mirror displacement, which reveals mechanical resonances that may be present in the system, we used a Bode 100 Network Analyzer to measure the response to a given input signal. The setup used for measurement is shown in Fig. 3.10. The tripod mirror was placed in a Michelson interferometer, which has arms of approximately 10 cm, short enough to avoid any steering. The other arm of the interferometer had a separate piezo mirror, which was used solely for feedback stabilization of the low frequency fringe drifts of the interferometer.

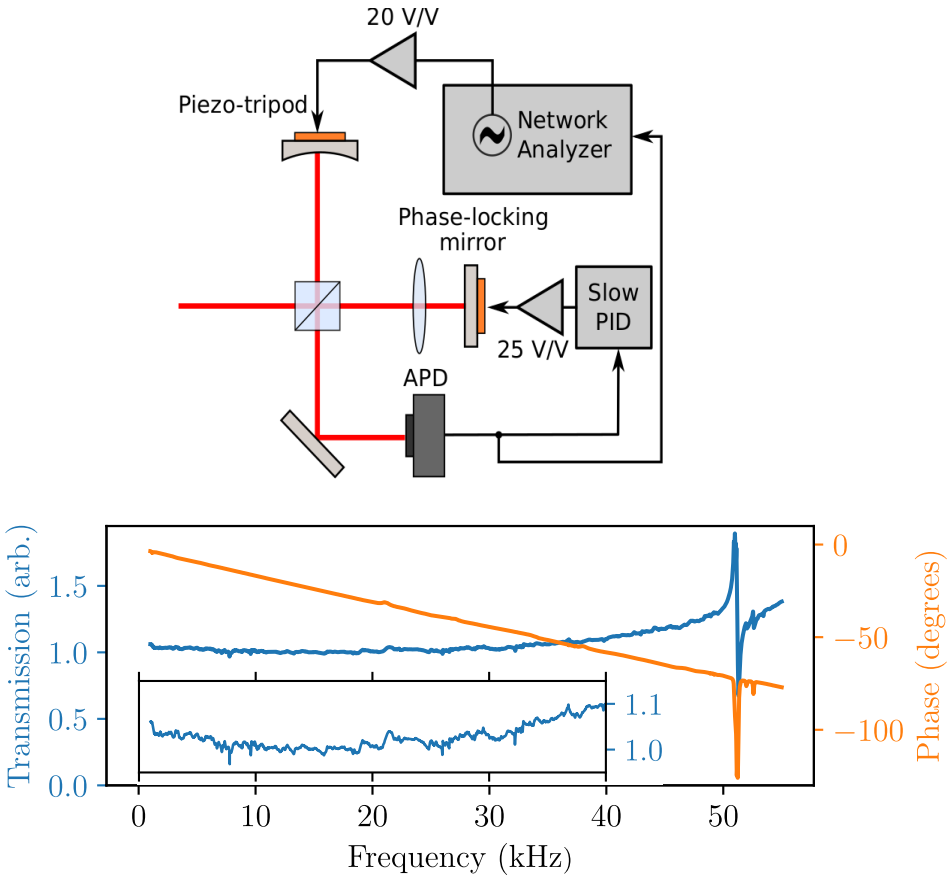

Figure 3.10: Experimental setup and mechanical response for mechanical resonances. The inset in the lower panel indicates how flat the response is up to 40 kHz.

The response is remarkably flat for frequencies up through 40 kHz, which we deemed suitable for the cold atom experiments that are performed later in this thesis.

Displacement

Characterization of the displacement of the tripod configuration was done using the same interferometer setup as shown in Fig. 3.10, just with the phase locking mirror set at a fixed position. By driving the tripod arm with a triangular voltage signal, we observed interference fringes on the APD and counting how many of these fringes occur in a period determines the physical displacement of the mirror An example measurement is shown in Fig. 3.11.

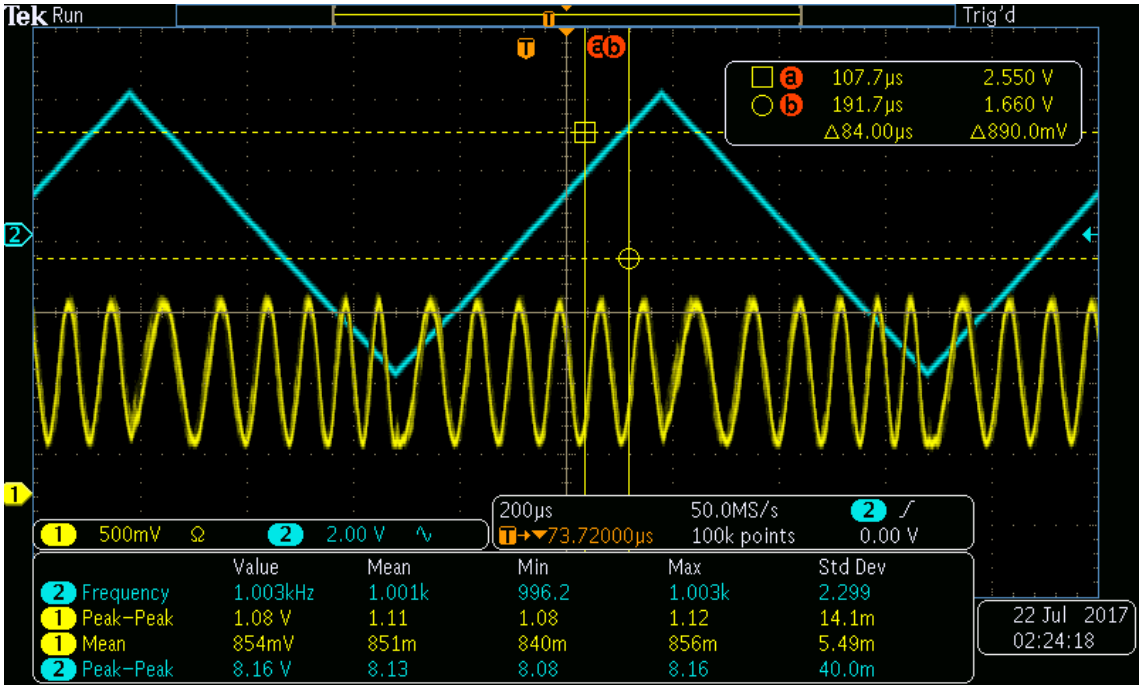

Figure 3.11: By driving the tripod mirror with a periodic triangular voltage, interference fringes pass on the detector. This example shows the signal produced by driving the piezo at 1kHz, with a maximum voltage of 160V. This particular measurement shows 12 fringes pass in a ramp, which corresponds to a displacement of 2.34 microns.

Based on our experimental determination, we found that the maximum displacement is approximately 2 μm at frequencies up to 8 kHz. To maximize the lifetime of the mirror, we added a software control in the system such that the product of the voltage and the frequency do not exceed a certain threshold. The displacement measurements over various frequencies are shown in Fig. 3.12.

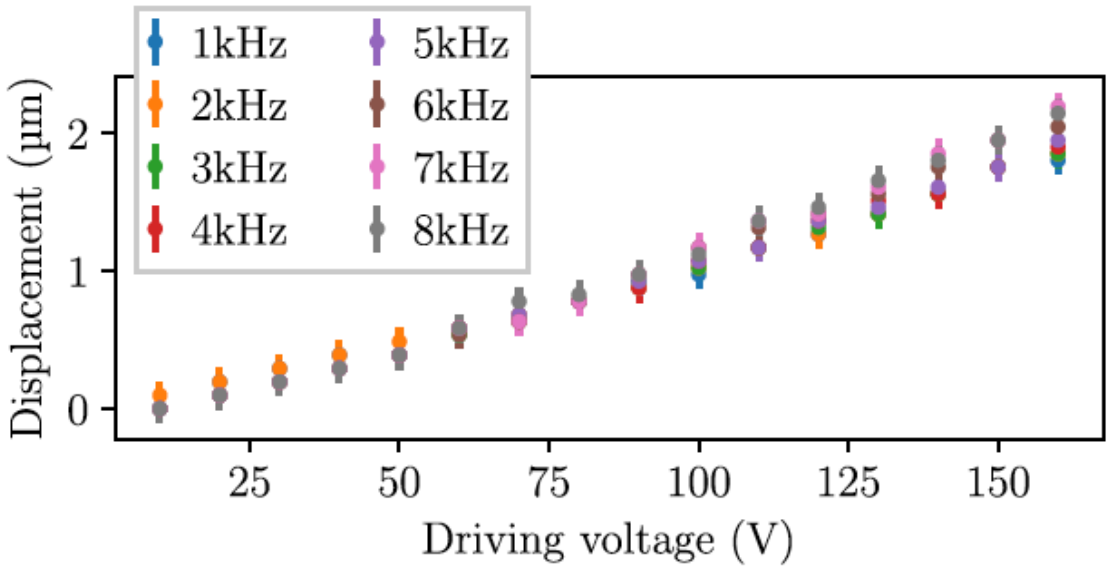

Figure 3.12: Measurement of piezo displacement vs drive voltage for various frequencies. We observe that all frequencies in this range can achieve a linear displacement up to about 2 microns.

Steering

We performed test experiments to check that the steering of the tripod mirror was in fact an improvement on a single piezo mirror. To check the static beam steering response, we place a beam profiler at a distance of 12.4 m away from the testing mirror, which allows us to measure small displacements from the steering angle. A DC voltage was applied and at each voltage, a set of 10 images with 1s exposure are taken and averaged. The beam profiler performs a fit of the centers using a 2D gaussian profile, and the extracted position allows us to determine the steering angle. The results, shown in Fig. 3.13, show that just adding the tripod piezo design, with equal voltages, can improve the steering by a factor of 20, and by optimizing the relative ratios of the voltages driving the piezos, steering can be reduced further to a factor of 60.

The final test for calibrating the system is to determine the performance in the actual cold atom experiment when driven with an AC signal. As discussed in section 3.7.1, lattice diffraction provides a measure of the lattice depth seen by the atoms. The diffraction of the lattice depends

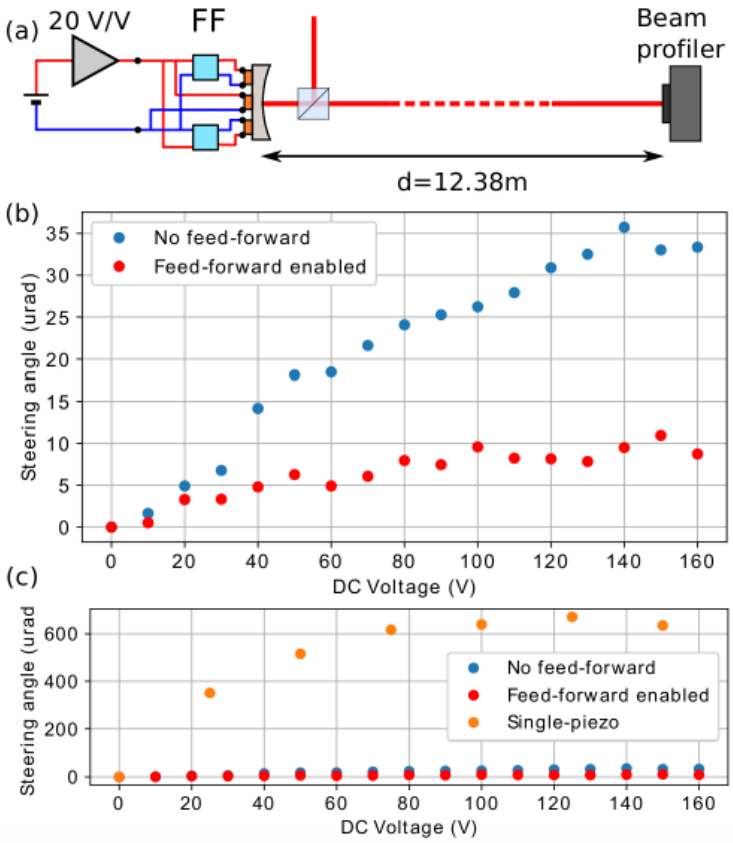

Figure 3.13: Measurement of DC steering angle vs drive voltage. (a) shows the experimental setup for measuring the center of the optical beam. (b) indicates the improvement from fine-tuning the relative voltages through the feed forward system, (c) A comparison of the two designs with respect to just using a single piezo mirror.

on the co-propogating beam's overlap with the atomic cloud. In the case of a large steering error from the piezo, we expect that the lattice intensity seen by the atoms would decrease, as the beam steers away from the position of the cloud. Using the atoms as a test for the steering, we re-checked the DC voltage and compared the resulting lattice intensity, as found from the first order diffraction. At the DC voltage, the single piezo quickly lost diffraction signal, with the lattice depth decreasing to half the original value at half of the maximum displacement.

The tripod design with the feed forward activated was impressively stable up to the maximum displacement, as shown in Fig. 3.14. To test the steering for AC driving, we periodically drove the piezo mirrors at a given frequency and performed a $2\mu s$ lattice pulse at various drive phases. As shown in the figure, at an example drive of 2kHz, the lattice depth remained flat, within error, throughout a full driving cycle of the piezo, which is indicative that the steering is not an issue for the cold atom system.

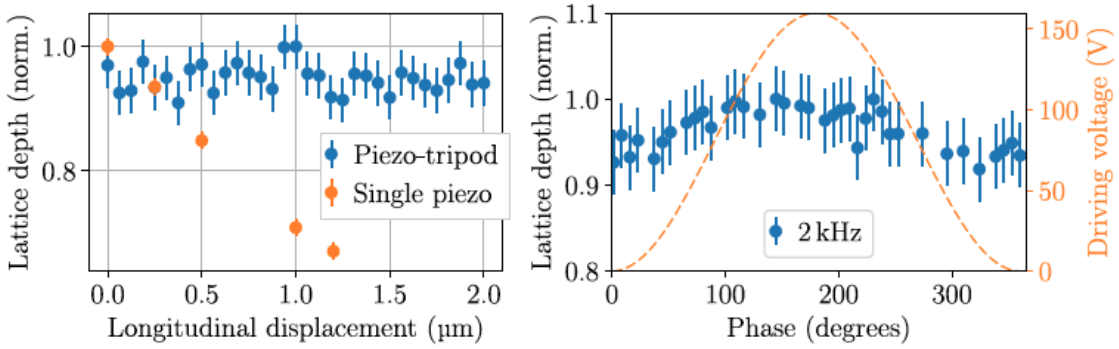

Figure 3.14: Determination of lattice steering on the lattice by measuring intensity seen by atoms. Left panel shows the results of applying a static DC voltage to the retro reflected mirror. The performance for a single piezo is notably bad, while the tripod design is significantly better, showing the same lattice intensity across the whole range of displacements. The right figure shows the results of lattice diffraction at various phases of the shaking at a frequency of 2kHz. The resulting lattice intensities show a very slight modulation slightly out of phase with the piezo drive. The deviation across the piezo drive cycle does not exceed the error, so we conclude the frequency dependent steering effects were small.

Chapter 4: Parametric Heating in Periodically Driven Optical Lattice

Heating in periodically driven systems in an interesting problem. In principle, periodic driving provides an infinite source of energy that can be transferred to the system. The most likely result is that the system heats towards an infinite temperature [14]. Remarkably, there are situations in which the drive induced heating does not immediately lead to the system reaching infinite temperature, such as bichromatic drives [51] or prethermal and disordered states [17, 52, 53, 54]. The detailed understanding of heating in interacting many-body systems is an outstanding theoretical question. In this section, I address our studies of one such heating mechanism in these periodically driven systems, which is the emergence of parametric instabilities.

4.1 Theory

The basis for theoretically understanding the emergence of the parametric heating mechanism was discussed in [55]. The high level approach is to treat the time dependent problem at a mean field level and then calculate time dependent fluctuations on top of the time dependent mean field solution, using a "Floquet-Bogoliubov" treatment. The starting point is a tight binding Bose-Hubbard Hamiltonian with a periodically driven term [56]. We present the theoretical approach using the example of a 1D optical lattice, but the results are easily extended to the 2D case we studied experimentally. The Hamiltonian is given by:

$$H = -J \sum_{<n,m>} a_n^\dagger a_m + a_m^\dagger a_n + \frac{U}{2} \sum_m n_m(n_m - 1) + K\cos(\omega t) \sum_m m n_m, \tag{4.1}$$

where J is the tunneling energy, U is the on-site interaction energy and K is the periodic drive strength.

In the mean-field limit of a condensate, we replace the quantum field on site n, a_n, with a constant classical field, $\alpha_n/\sqrt{N}$, representing the condensate, with N total atoms. Substituting this approximation into the Heisenberg equations of motion, one obtains the equations for the classical amplitudes:

$$i\partial_t \alpha_n = -J(\alpha_{n+1} + \alpha_{n-1}) + g|\alpha_n|^2\alpha_n + K\cos(\omega t) n \alpha_n, \tag{4.2}$$

where $g = U\rho$ is an effective interaction term with ρ being the number of atoms per site, and the amplitudes obey the normalization $\sum_i |\alpha_i|^2 = N$. As discussed in Section 2.1, the drive results in a renormalized hopping amplitude, and the initial wave function $a_n^0(t)$ will be the solution of the effective GPE

$$-J\mathcal{J}_0(K/\omega)(a_{n+1}^0 + a_{n-1}^0) + U|a_n^0|^2 a_n^0 = \mu a_n. \tag{4.3}$$

In this effective equation of motion, the time dependent drive term has been eliminated, but the tunneling is renormalized to an effective $J_{\text{eff}} = J\mathcal{J}_0(K/\omega)$

The ground state condensate wave function will be a bloch wave with either $q_0 = 0$ or $q_0 = \pi$, where the momentum of the ground state depends on the value of the effective tunneling. If $\mathcal{J}_0(K/\omega) > 0$, then the ground state momentum will be $q_0 = 0$, but when $\mathcal{J}_0(K/\omega) < 0$, the

band structure is inverted and the ground state wave function is the bloch wave at $q_0 = \pi$.

Given the initial condensate wave function, one is interested in the stability of the fluctuations, δa_n on top of the condensate a_n^0:

$$a_n(t) = a_n^0(t)(1 + \delta a_n(t)). \tag{4.4}$$

This mode is plugged into the equation of motion (4.2) and linearized by ignoring terms proportional to $|\delta a_n|^2$, which results in coupled equations for $\delta a_n(t)$ and $\delta a_n^*(t)$:

$$\begin{aligned} i\partial_t \delta a_n(t) = \frac{-J}{a_n^0(t)} \left(a_{n+1}^0 \delta a_{n+1} + a_{n-1}^0 \delta a_{n-1}\right) + K\cos(\omega t) n \delta a_n + 2U|a_n^0|^2 \delta a_n \\ + U|a_n^0|^2 \delta a_n^* - i\frac{\partial_t a_n^0}{a_n^0}\delta a_n \end{aligned} \tag{4.5}$$

as well as the complex conjugate. Recalling the initial state was given as $a_n^0 = e^{iq_0 n}$, one can remove the periodic driving term by performing a time dependent gauge transformation,

$$a_n(t) \to a_n(t) e^{-in\alpha \sin(\omega t)}, \tag{4.6}$$

where $\alpha = K/\omega$. The transformed amplitudes with the additional fluctuation are substituted into Eq. 4.2

$$i\dot{\delta a_n} = -J\left(e^{iz}\delta a_{n+1} + e^{-iz}\delta a_{n-1}\right) + 2U\rho\delta a_n + U\rho\delta a_n^*, \tag{4.7}$$

where I introduce $\rho \equiv |a_n^0|^2$ and $z \equiv q_0 - \alpha\sin(\omega t)$. We now perform the standard Bogoliubov

transformation on the fluctuation term δa_n

$$\delta a_n = \sum_q u_q(t)e^{iqn} + v_q^*(t)e^{-iqn}, \tag{4.8}$$

which results in a Bogoloubov-de Gennes (BdG) equation:

$$i\partial_t \begin{pmatrix} u_q \\ \\ v_q \end{pmatrix} = \begin{pmatrix} E(q,t)+g & g \\ \\ -g & -E(q,t)-g \end{pmatrix} \begin{pmatrix} u_q \\ \\ v_q \end{pmatrix}, \tag{4.9}$$

where the effective, time averaged 'energy' is given by $E(q,t) = 4J\sin(q/2)\sin\left(q/2 + q_0 - \alpha\sin(\omega t)\right)$ and the interaction parameter $g \equiv U\rho$. The effective time averaged $E(q,t)$ can be expressed as $-2J\cos(q + q0 + \alpha\sin(\omega t)) + 2J\cos(q_0 + \alpha\sin(\omega t))$, which is equivalent to the difference between the Bogoliubov energy on top of the BEC and the energy of a BEC at q_0. The matrix appearing in this expression contains the periodic time dependence of the system. To study the dynamics, the initial system is time evolved one period to determine the propagator matrix, $\mathcal{U}$. Following Floquet theory, the quasi-energies of the system, ϵ_q are related to the eigenvalues, λ_q of the propagator through the relation $\lambda_q = e^{-i\epsilon_q T}$.

Considering the case where the quasi energy contains both a real and imaginary part $\epsilon_q = r_q + is_q$, the time evolution of the system will be $e^{-ir_q t}\, e^{s_q t}$, which displays oscillatory behavior in the real part, but can exponentially grow (decay) in the case where s_q is positive (negative). These Lyapunov exponents, where the quasi energy contains a positive imaginary component, are indicative of a dynamical instability, where there is an exponential growth of an excitation/mode at a given q.

Since each mode can have an imaginary part that contributes to the dynamical instability, a

good measure of the system response is the growth rate of the most unstable mode,

$$\Gamma_{\text{mum}} = \max_q s_q. \tag{4.10}$$

The reasoning for this selection is that in the long time limit, the exponential behavior will be dominated by the largest value, as shown in [55]. In realistic systems, this model is an oversimplification due to the interactions between the growing modes, which mix in other modes as time evolves.

Following the techniques presented in [55, 57], we can map the BdG equations, 4.9, into a parametric oscillator. To do so, we express the time averaged energy as

$$E_{\text{avg}}(q) = \sqrt{4|J_{\text{eff}}|\sin^2(q/2)(4|J_{\text{eff}}|\sin^2(q/2) + 2g)}, \tag{4.11}$$

which is obtained by time averaging the effective GPE, Eq. 4.3, with $J_{\text{eff}} = J\mathcal{J}_0(K_0)$. As noted in [55], this time averaged energy corresponds to the zeroth order Floquet quasienergy. The full transformation can be broken into two parts, the first diagonalizing the time averaged component:

$$\begin{pmatrix} u_q \\ v_q \end{pmatrix} = \begin{pmatrix} \cosh(\theta_q) & \sinh(\theta_q) \\ \sinh(\theta_q) & \cosh(\theta_q) \end{pmatrix} \begin{pmatrix} u'_q \\ v'_q \end{pmatrix} \tag{4.12}$$

where $\cosh(2\theta_q) = \left(4|J_{\text{eff}}|\sin^2(q/2) + g\right)/E_{\text{avg}}(q)$ and $\sinh(2\theta_q) = g/E_{\text{avg}}(q)$. The second

transformation, which transforms into a frame rotating at $2E_{\text{avg}}$, is given by

$$\begin{pmatrix} \tilde{u}'_q \\ \tilde{v}'_q \end{pmatrix} = \begin{pmatrix} e^{2iE_{\text{avg}}(q)t} & 0 \\ 0 & 1 \end{pmatrix} \begin{pmatrix} u'_q \\ v'_q \end{pmatrix}. \tag{4.13}$$

The equation of motion can then be expressed as

$$i\partial_t \begin{pmatrix} \tilde{u}'_q \\ \tilde{v}'_q \end{pmatrix} = \left[E_{\text{avg}}(q) + W_q(t) + \frac{g}{E_{\text{avg}}} \begin{pmatrix} 0 & h_q(t)e^{-2iE_{\text{avg}}(q)t} \\ -h_q(t)e^{2iE_{\text{avg}}(q)t} & 0 \end{pmatrix} \right] \begin{pmatrix} \tilde{u}'_q \\ \tilde{v}'_q \end{pmatrix} \tag{4.14}$$

which are equivalent to the equations describing a parametric oscillator, with $W_q(t)$ a diagonal matrix that time averages to 0 and $h_q(t)$ is a real-valued function which can be expressed as a fourier series using the Jacobi-Anger identity, and the relation, $\mathcal{J}_\ell(x) + \mathcal{J}_{-\ell}(x) = 0$:

$$h_q(t) = 4J \sin^2(q/2) \sum_{\ell=-\infty}^{\infty} \mathcal{J}_{2\ell}(K/\omega) e^{2i\ell\omega t}, \tag{4.15}$$

which contains only even harmonics of the drive frequency.

Using the analogy of a parametric oscillator, we can map the oscillator's eigenfrequency, ω_0 to the time averaged dispersion, E_{avg} and use the substitution $\omega_{po} = 2\omega$ (po indicating parametric oscillator). From the classical results, the oscillator will display a parametric instability for $\omega = 2\omega_0$. Given that each q has a different average E, each mode can be treated as an independent parametric oscillator. Additionally, because the Fourier expansion of h_q contains an infinite number of harmonics, the resonance will occur once any even harmonic, $2\ell\omega$, becomes equal to $2E(q)$. For sufficiently low interaction strengths, one can approximate the function h_q

to the second harmonic ($\ell = 1$ Fourier component). The last term in 4.14 can be expressed as

$$\frac{8J\mathcal{J}_2(K/\omega)\sin^2(q/2)g}{E_{\text{avg}}}\begin{pmatrix} 0 & \cos(2\omega t)^{-2iE_{\text{avg}}(q)t} \\ -\cos(2\omega t)e^{2iE_{\text{avg}}(q)t} & 0 \end{pmatrix} \tag{4.16}$$

From the classical parametric oscillator [58], and the substitutions above, the instability rate can be expressed as

$$s_q = \frac{4J\mathcal{J}_2(K/\omega)\sin^2(q/2)g}{E_{\text{avg}}}\sqrt{1-\left(\frac{(\omega - E_{\text{avg}})E_{\text{avg}}}{4J\mathcal{J}_2(K/\omega)\sin^2(q/2)g}\right)^2}, \tag{4.17}$$

In the long time limit, the dynamics will be governed by the most unstable mode which is the highest value of s_q.

At first order, the emergence of a parametric instability can be seen in the case where $E_{\text{avg}} \approx \omega$. In this scenario, our condensate effectively absorbs a drive photon and excites a resonant Bogoliubov mode, which grows exponentially with a rate given by:

$$\Gamma_q = \frac{4J\mathcal{J}_2(K/\omega)\sin^2(q/2)g}{\omega} \tag{4.18}$$

At second order, the instability can occur in a region around the resonance point and the maximally unstable mode has a rate given by

$$\Gamma = \frac{|\mathcal{J}_2(K/\omega)|\, g}{|\mathcal{J}_0(K/\omega)|\, \omega}\left(\sqrt{g^2+\omega^2} - g\right). \tag{4.19}$$

In this treatment of the 1D shaken optical lattice, there is a cutoff in the drive frequency. When ω becomes greater than E_{avg}, the $q = \pi$ point will be maximally unstable, but an excitation

would violate energy conservation. In a system with weak confinement in directions perpendicular to the lattice, a 1D lattice would consist of an unbounded energy spectrum in the transverse degree of freedom. When the drive frequency exceeds the maximum excitation energy, the system can become unstable at the maximum dispersion, namely $E_{\text{avg}}(q = \pi)$, and the difference will be absorbed into the transverse direction. This was the subject of [59], which measured parametric instabilities in a driven 1D system.

4.1.1 Driving in 2D

Our experimental system allows us to realize a 2D optical lattice with arbitrary 2D driving trajectories. In addition, the system is a lattice of tubes, meaning there is a transverse degree of freedom along the z direction. In this section, we follow the methodology from [55, 60] and go through the key results for the 2D system.

Similar to the 1D case, we consider the time dependent GPE on a square lattice in the tight binding limit:

$$\begin{aligned} i\partial_t a_{m,n} = -J(a_{m,n+1} + a_{m,n-1} + a_{m-1,n} + a_{m+1,n}) + U|a_{n,m}|^2 a_{m,n} \\ + a_{m,n} K(m\sin(\omega t) + \epsilon n \sin(\omega t + \phi)) \end{aligned} \tag{4.20}$$

where ϵ, ϕ represent the shake trajectory. When $\epsilon = 0$, we consider shaking along the x direction only, and when $\epsilon = 1$, a phase of 0 ($\pi/2$) results in diagonal (circular) shaking. The treatment of the mode functions, is the same as in Eq. 4.9, but each drive will have a different dispersion, $E(q, t)$ and a different Fourier decomposition of h_q. For the following, we consider just the case when the normalized drive amplitude, $K_0 \equiv K/\omega < 2.4$, which corresponds to the effective

tunneling, J_{eff} being positive.

X Shaking

For the case of shaking along one single direction, $\epsilon = 0$, the BDG equation gives the following values for $E(q,t)$ and $h_q(t)$

$$E(q,t) = 4J\left(\sin(q_x/2)\sin(q_x/2 - K\sin(\omega t)/\omega) + \sin^2(q_y/2)\right), \tag{4.21}$$

$$h_q(t) = 8J\sin^2(q_x/2)\sum_{\ell=1}^{\infty}\mathcal{J}_{2\ell}(K/\omega)\cos(2\ell\omega t) \tag{4.22}$$

When $\omega > \sqrt{4J_{eff}(4J_{eff}+2g)}$, the most unstable mode occurs for $q = (\pi, 0)$, and the associated rate is given by

$$\Gamma_x = \frac{4J\mathcal{J}_2(K/\omega)g}{\omega}. \tag{4.23}$$

When ω is less than that effective bandwidth, the maximally unstable mode occurs at a specific q [55], and the rate is given by

$$\Gamma = \frac{|\mathcal{J}_2(K/\omega)|\, g}{|\mathcal{J}_0(K/\omega)|\, \omega}\left(\sqrt{g^2+\omega^2} - g\right). \tag{4.24}$$

Diagonal Shaking

For diagonal shaking, $\epsilon = 1$ and $\phi = 0$, the expressions for E and h_q are given by

$$E(q,t) = 4J\left(\sin(q_x/2)\sin(q_x/2 - K\sin(\omega t)/\omega) + \sin(q_y/2)\sin(q_y/2 - K\sin(\omega t)/\omega)\right) \tag{4.25}$$

$$h_q(t) = 8J\left(\sin^2(q_x/2) + \sin^2(q_y/2)\right)\sum_{\ell=1}^{\infty}\mathcal{J}_{2\ell}(K/\omega)\cos(2\ell\omega t) \tag{4.26}$$

When the frequency exceeds the saturation frequency (which is different from the saturation frequency for the linear driving), the maximally unstable mode for the diagonal shaking occurs at the corner of the band, $q = (\pi, \pi)$ and the rate can be expressed as

$$\Gamma_{\text{diag}} = \frac{8J\mathcal{J}_2(K/\omega)g}{\omega} = 2\Gamma_x. \tag{4.27}$$

When the frequency does not exceed the saturation, and is resonant with a given mode, the rate is equivalent to Eq. 4.27. Because the maximally unstable mode occurs at the band edge, the saturation frequency is actually equal to the effective Bogoliubov bandwidth, unlike the x-only drive.

Circular Shaking

In the case of circular shaking, $\epsilon = 1$, $\phi = \pi/2$, E and h_q are given by

$$E(q,t) = 4J\left(\sin(q_x/2)\sin(q_x/2 - K\sin(\omega t)/\omega) + \sin(q_y/2)\sin(q_y/2 + K\sin(\omega t)/\omega)\right), \tag{4.28}$$

$$h_q(t) = 8J\left(\sin^2(q_x/2) + \sin^2(q_y/2)\right)\sum_{\ell=1}^{\infty}\mathcal{J}_{2\ell}(K/\omega)\cos(2\ell\omega t) \tag{4.29}$$

When the frequency exceeds the saturation frequency (which is different from the saturation frequency of the 1D drive), the maximally unstable modes occur at $q = (\pi, 0)$ and $q = (0, \pi)$ and

the rate is given by

$$\Gamma_{\text{diag}} = \frac{4J\mathcal{J}_2(K/\omega)g}{\omega} = \Gamma_x. \tag{4.30}$$

Just like in the diagonal drive, when the frequency is less than the saturation frequency, the rate is given by Eq. 4.27.

In summary, the three different shaking configurations result in different q points for the maximally unstable mode. For diagonal driving, the saturation frequency is equal to the effective bandwidth and for circular or linear driving, the saturation frequency will be slightly less than the effective bandwidth. When the drive frequency is less than the critical frequency, the rates are expected to be the same, but when the drive frequency exceeds the critical value, one expects the linear and the circular drives to have the same rate, but the diagonal drive should have rates at twice the value.

4.2 Experiment

Having gone through the background theory behind the parametric instabilities and the expected rates, we now describe the results we obtained. The experimental used our lattice (described in Sec. 3.7) in a simple 2D, $\lambda/2$ configuration, shaken in different 2D trajectories.

To compare the theoretical predictions to what we can experimentally observe, we note that our experiment begins with a BEC, which has atoms condensed into the a_0 mode and the parametric instability was a maximum growth of a mode a_q, which has a rate Γ_q. Since this mode evolves as $a_q = e^{\Gamma_q t}$, the actual observable quantity, which is $|a_q|^2$ will grow at a value $2\Gamma_q$, resulting in a depletion of the initial condensate, which is measured through the condensate fraction. For short times, the decay rate should be a concave down function, namely $1 - e^{\Gamma t}$, but

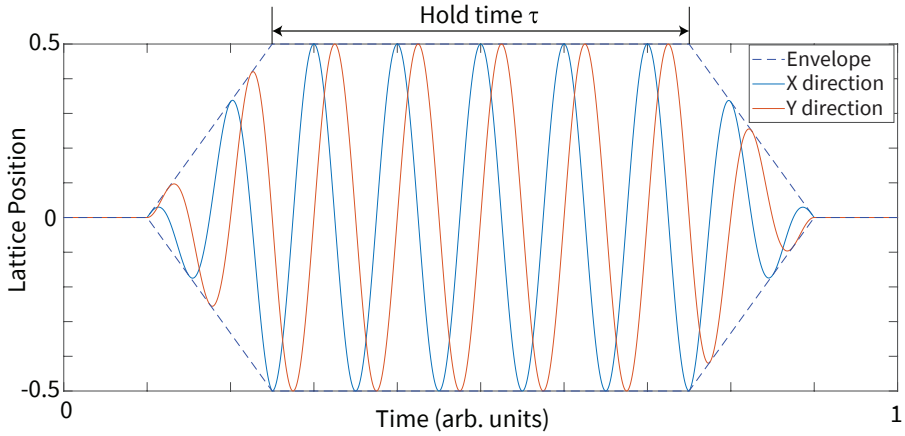

Figure 4.1: Schematic showing lattice driving of the individual piezo mirrors. The hold time is chosen to be multiple steps of the shaking period, in order to eliminate any micromotion effects.

interactions and thermalization on fast timescales result in exponential decay of the condensate, namely $a_0(t) = a_0 e^{-\Gamma t}$.

The experimental sequence used for extracting the rates is as follows: in roughly 2ms, the piezos are ramped to their desired shaking amplitudes. The ramp up time is chosen to be an integer multiple of the period, so the time varies for different conditions, but the end phase is the same. This time is typically 5-10 periods. Once the shaking is on, we hold for a variable time, which is also chosen to be integer multiples of the period in order to eliminate any potential effects due to micro motion that occurs during the drive. After the variable time, the shaking is then ramped off in a couple drive periods. This procedure is shown below.

In order to measure the condensate fraction, we perform a 2D fit to the atomic distribution after time of flight. We fit to a sum of Thomas-Fermi and thermal distributions, which gives a measure of condensed fraction of atoms. We observe an exponential decay of the condensate fraction with time, and we extract a rate by fitting an exponential decay. An example decay curve is shown in Fig. 4.2, where we extract a decay rate of 31.6 (8) s^{-1}.

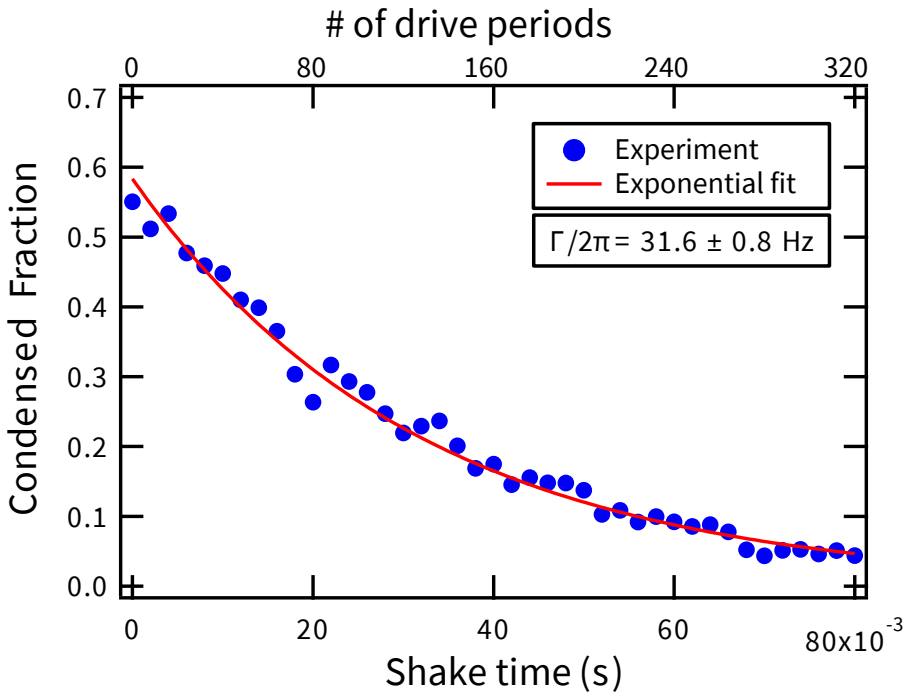

Figure 4.2: Sample exponential decay observed for shaking procedure. Condensate fraction determined through a 2D fit of optical depth after time of flight.

4.3 Experimental Results

In this section, we discuss the results of the experiments to measure the condensate decay as a function of various parameters in the system, indicating the presence of parametric instabilities in the periodically driven optical lattice.

4.3.1 Lattice Depth Dependence

One of the key features of the parametric instability in the high frequency regime is the linear scaling in the quantity gJ, as opposed to the Fermi Golden Rule (FGR) theory, where heating rates are expected to scale as$(gJ)^2$. To test the scaling, we measured heating rates at two different drive frequencies of $\omega/2\pi$ =4 kHz, 2.5 kHz with a fixed drive strength of $K_0 = 2.1$. To adjust the parameters g, J, we varied the lattice depth and used a numerical band structure

calculation to determine J and g. This experiment was performed for the x only driving and the diagonal driving, and the scaling is shown in Fig. 4.3.

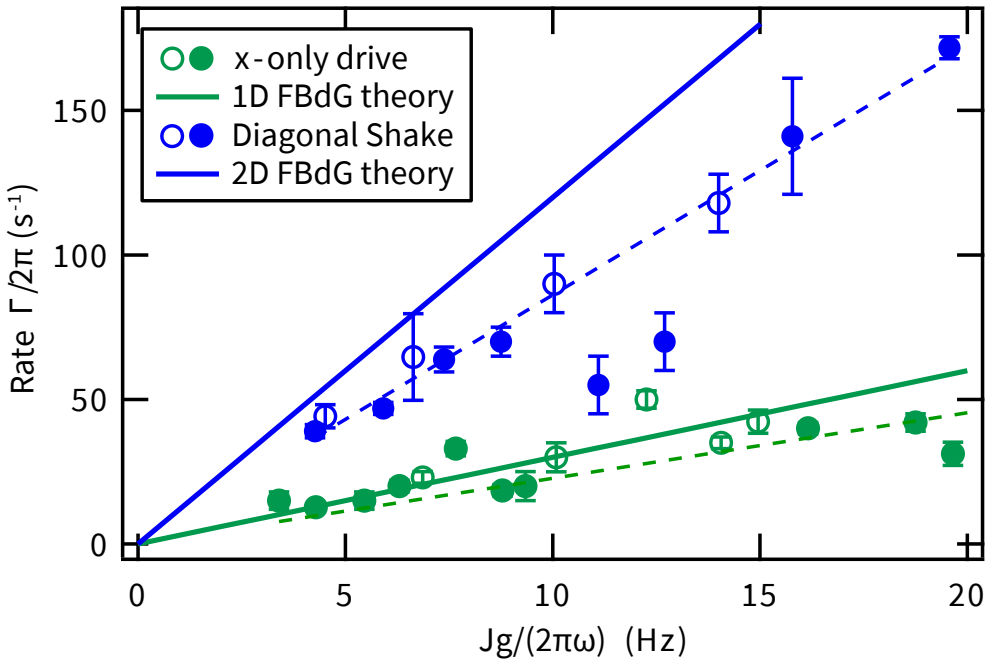

Figure 4.3: Measured decay rates for $K_0 = 2.1$, ω =4kHz (filled circles) and $\omega = 2.5$kHz (empty circles) at various lattice depths, compared to parametric instability theory. The horizontal axis is $Jg/(\omega)$, since the parametric instability theory predicts the mode's growth rate to be linear in J, g and $1/\omega$. The dashed lines are linear fits to the data.

From the data, we can clearly see that there is a linear dependence of the combined lattice quantity. For the 1D shake, the theoretical prediction matches well to the observed decay rates and in the 2D experiments, we clearly see a linear relationship, but at a slightly different slope than experimentally predicted.

4.3.2 Drive Amplitude Dependence

In order to determine the dependence of the heating rates on the drive amplitude, K_0, we perform decay measurements at a lattice depth of $11E_R$ and a drive frequency of 2.5 kHz for the three trajectories. The 2.5 kHz drive frequency is chosen as a fixed value that exceeds the

effective bandwidth, and is also far from the 21 kHz lattice vibrational spacing, which ensures that the single band tight binding picture is accurate. In this regime, we expect the heating rates to scale as $\mathcal{J}_2(K_0)$.

When K_0 is greater than ≈ 2.4, the effective bandwidth becomes negative and $q = 0$ is unstable. To perform experiments with $K_0 > 2.4$, we apply a force using the magnetic quadrupole trap, which accelerates the BEC into the stable regime. To minimize the heating and loss due to the instabilities arising from the static band curvature, [61], we synchronized the BEC acceleration with the shaking amplitude ramp. The timing is chosen such that at the instant $K_0 = 2.4$ during the ramp of the drive, the quasimomentum crosses the instability point in the Brillouin zone, $q \approx 0.6$.

We summarize the results from the experiment in Fig. 4.4. The first observation is that the x-only shake follows the $\mathcal{J}_2$ behavior up to the band inversion point. Beyond that value, we accelerate the BEC to $q = (\pi, 0)$, and we find that the heating deviates from the expected values. This is not a surprise, as there is quite a large amount of heating that occurs during the acceleration stage.

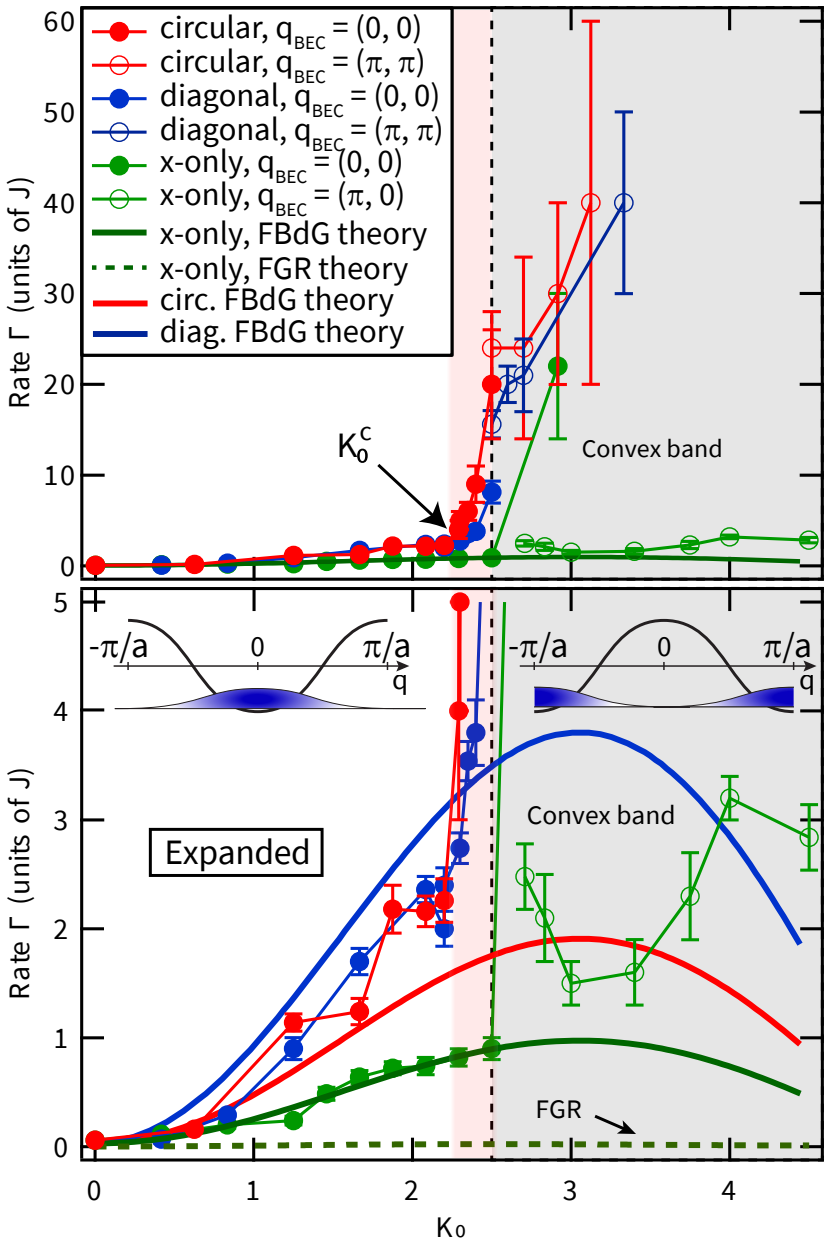

Figure 4.4: $\Gamma(K_0)$**:** Comparison between circular (red), diagonal (blue) and x-only (green) drives for $V_0 = 11\ E_R$ and $\omega = 2\pi \times 2.5$kHz. The rates are in units of $J = 2\pi \times 50$Hz, shown full scale (top) and zoomed in (bottom). The parametric oscillator theory is shown for each drive as solid lines, and the 1D FGR-based scattering theory is shown as the green dashed line (zoom only). Filled circles indicate data taken at $\mathbf{q} = (0, 0)$, while open circles indicate data taken at $\mathbf{q} = (\pi, \pi\ (0))$ to keep the BEC in the stable region of the band (illustrated with the bottom plot cartoon). A dramatic increase in the rate occurs at the critical K_0 value for the circular and diagonal drives, highlighted by the light red region.

For the 2D drives, we find that the heating rates are roughly the same for both diagonal

and circular drives, despite the prediction that diagonal driving should be twice as fast. While there is a numerical deviation from the theoretical prediction, we see that the general dependence qualitatively follows the $\mathcal{J}_2$ dependence.

While the heating rates are expected to blow up when the band inverts for $\mathcal{J}_0(K_0) < 0$, we find that the rate explosion occurs at a lower critical drive strength, $K_0^c < 2.4$. As will be discussed later, we actually find that there is a surprising change in frequency dependence once we reach this critical amplitude.

Critical Drive Amplitude

The explosion of heating rates at lower K_0 than the single-particle inversion value, $K_0 = 2.4$ suggests effects that are not captured in the parametric instability theory. We investigate the dependence of the critical amplitude as a function of the drive frequency in Fig. 4.6. The critical value of the drive strength is found by scanning K_0 at a fixed drive time and observing where there is a kink in the surviving condensate fraction, indicating significantly increased loss. An exemplary scan is shown in Fig. 4.5. We find the critical value by fitting two lines with variable slopes and whose intersection point is a fit parameter. The critical value is taken to be the value of where the slope change occurs.

Figure 4.6 shows the resulting critical K_0 values as a function of the drive frequency, ω. While not entirely understood, we find a phenomenological relationship between the two parameters given by:

$$\mathcal{J}_0(K_0^c) = \frac{g}{\omega}. \tag{4.31}$$

We speculate that the rate explosion for $K_0^c < 2.4$ is due to finite frequency effects. In the typical Bose-Hubbard picture, the highly correlated regime occurs when $g/J_{eff} > \simeq 1$. On the

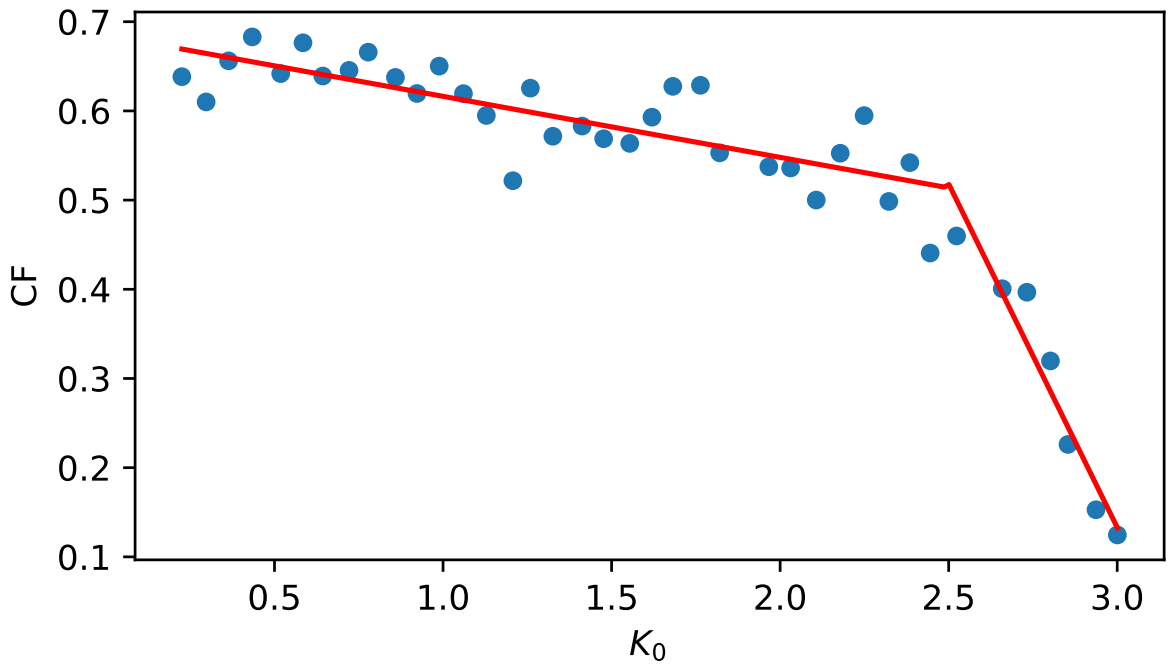

Figure 4.5: Single scan of the condensate fraction against K_0 at a fixed frequency and fixed time. The critical K_0 value is determined to be where the heating rate increases, which is seen as the kink in the figure.

other hand, when one considers high frequency expansions of the driven Bose-Hubbard model, the first order Floquet corrections scale as J/ω. If we set the scale so that this product is 1, we recover Eq. 4.31. While this is not necessarily an argument that this relationship should hold, we do find very good agreement between the experiment, which is likely indicative that the onset of strong correlations with sufficient Floquet corrections between the time averaged approximation are important to explain the behavior.

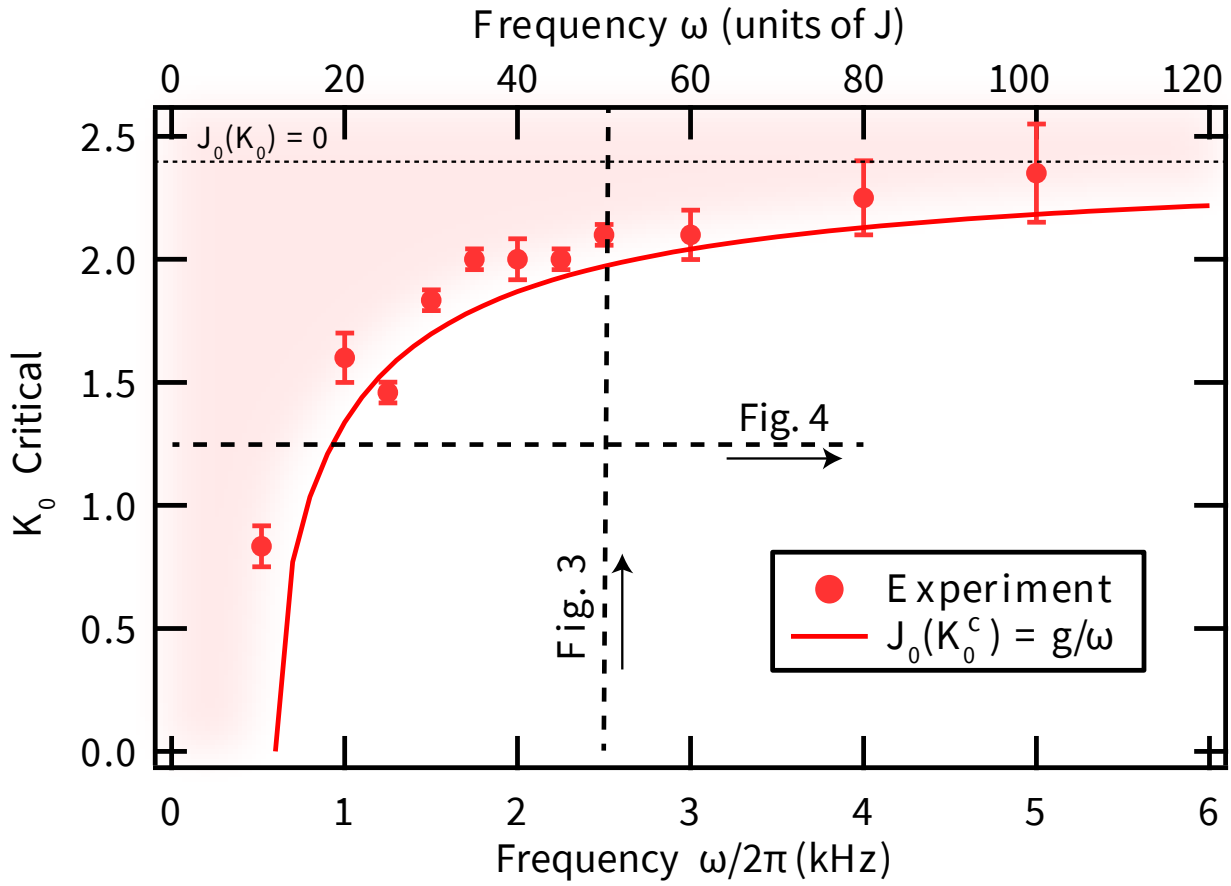

Figure 4.6: Measured critical K_0 value for various frequencies. We observe that for high frequencies, this value approaches the expected 2.4 (where the band inverts). The solid red curve is a phenomenological relationship described in this chapter, that captures this behavior both qualitatively and quantitatively well.

4.3.3 Frequency Dependence

The next parameter dependence we investigate is the dependence of the heating rate on the drive frequency. As described earlier, there exist two frequency regions, the first is where the drive frequency is less than a critical value, and we can directly excite a mode which is unstable. The second, where the frequency exceeds the critical value, excites an unstable mode corresponding to the maximum of the Bogoliubov spectrum. Measurements were performed experiments at a lattice depth of $V_0 = 11E_R$ and a drive strength of $K_0 = 1.5$ and are summarized in Fig. 4.7.

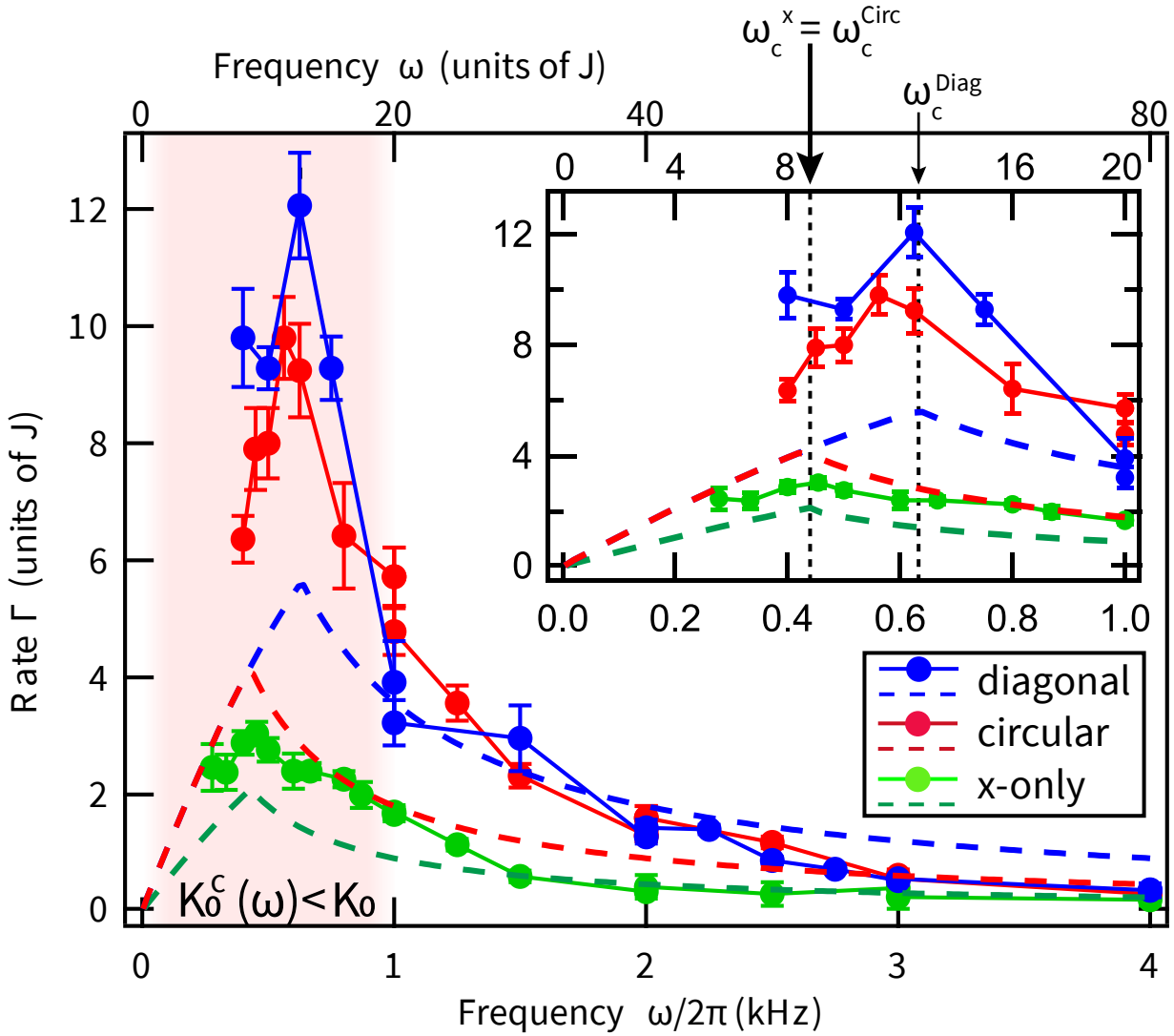

Figure 4.7: $\Gamma_{\rm cf}(\omega)$ for the three drive trajectories at $K_0 = 1.25$ and $V_0 = 11\ E_R$. The parametric oscillator theory $\Gamma_{\rm mum}(\omega)$ is shown for each trajectory as dashed lines. The theoretical cusp positions are marked as vertical black dashed lines. The value we use for g is fit to the x-only drive cusp, and is close to the expected value from a Bose-Hubbard type calculation. Rate explosion occurs at low frequencies when $K_0 > K_0^c(\omega)$, represented as the light red zone.

We see that for all three drive trajectories, there is an increase of the heating rate with the drive frequency. This is due to the frequency matching a resonance condition within the effective bandwidth and creating an unstable excitation. When the drive frequency exceeds this critical frequency, we find that there is an ω^{-2} dependence to the rates, whereas the theory predicts the rate to go as ω^{-1}. Beyond the critical K_0 value, we find that the ω^{-1} dependence is recovered.

An example is shown in Fig. 4.8, where the rates at $K_0 = 1.25, 2.3$ have different frequency dependence.

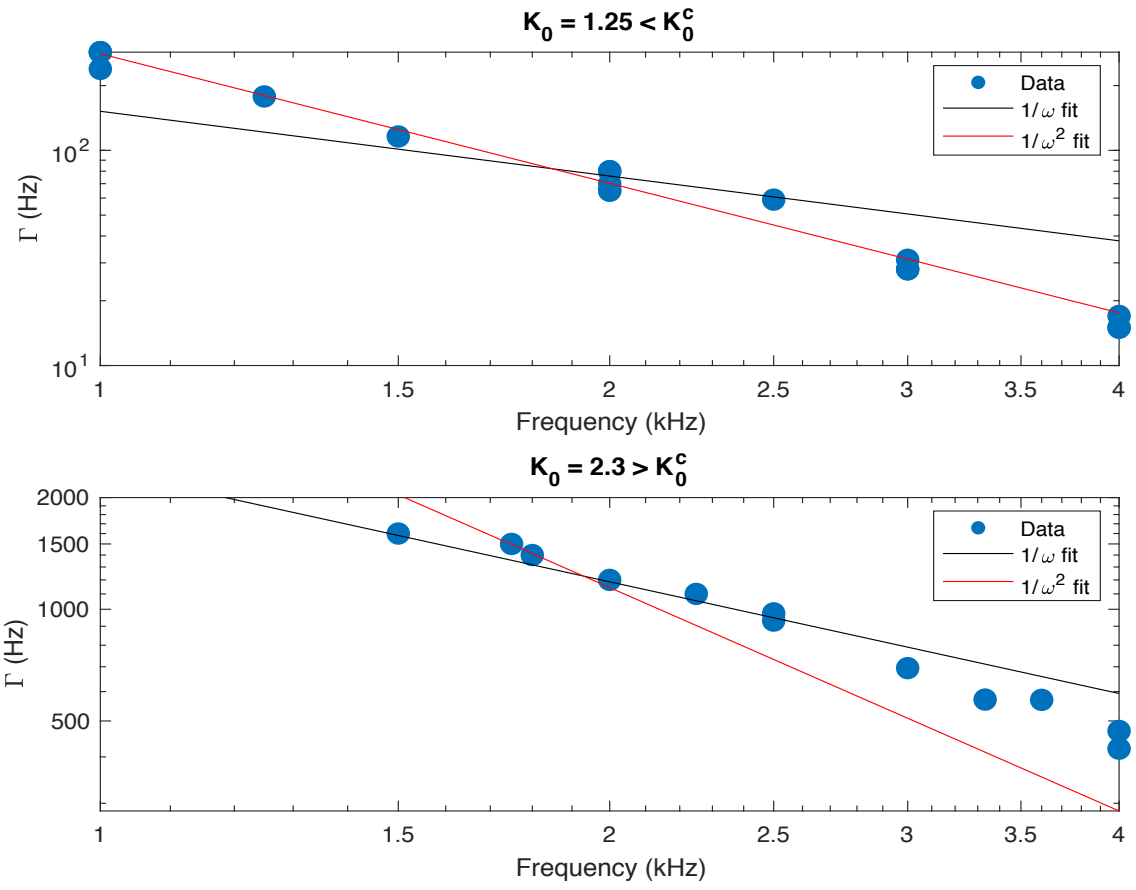

Figure 4.8: Example decay rates below and above the critical drive strength. When $K_0 < K_0^c$, we find that there is an ω^{-2} dependence, whereas when $K_0 > K_0^c$, we find that there is an ω^{-1} dependence.

4.3.4 Comparison With Fermi Golden Rule

As briefly mentioned throughout this section and in some figures, we find that our heating rate measurements generally agree with the parametric oscillator treatment, with the exception being the ω^{-2} dependence at lower K_0. Another general approach is based on the Fermi Golden Rule treatment [62]. As detailed in this work, there exist heating processes involving scattering

to higher bands as well as interactions within the same band. The estimate of the heating rate for an intraband, ℓ photon resonance, which couples two particles from (q, q) to $(q - k, q + k)$, is given from this work as:

$$\Gamma = \sum_k \frac{2\pi}{\hbar} |C^\ell(k, q)|^2 \rho \tag{4.32}$$

where C^ℓ is the scattering matrix element for an ℓ photon resonance and ρ is the density of states. The estimate for the matrix element will scale as $\mathcal{J}_\ell(K_0)/(\ell\omega)$. Given that the density of states will be independent of the drive parameters, we can substitute this dependence, which are the results shown in the previous figures. The magnitude of the rates estimated using this approach are on the order of 30 times less than what is observed, which indicates that the heating is better described by the appearance of unstable parametric resonances.

Chapter 5: Relaxation into Floquet Prethermal Condensates

In order for a periodically driven system to provide a useful simulation, it should not heat on timescales shorter than the timescale of the experiment of interest. At the same time, the interaction driven dynamics should be fast enough to allow for equilibrating in the effective Floquet system. Several studies have shown that prethermal conditions can be satisfied for systems with bounded energy spectra in the high frequency limit[15, 18, 19, 20].

For lattice systems, the bands of interest are often reasonably isolated, but when considering the Floquet system, higher lying bands can be coupled through a higher order resonance, which can result in heating. In the weakly interacting limit, periodically driven, isolated lattice systems have been used to simulate artificial gauge fields [4, 45, 63, 64, 65] and spin-orbit coupling, and engineer interesting band structures [1, 47, 66]. For these systems, Floquet prethermalization is not guaranteed, and heating depends on specific details of the system. Previous Floquet-engineered experiments using Bose Einstein condensates have implicitly relied on the existence of a Floquet pre-thermal timescale, since the BEC had to be stable long enough to prepare it in a Floquet state [63, 67, 68, 69, 70, 71, 72, 73].

Here, we experimentally study interaction-induced thermalization of bosons subject to a Floquet-engineered effective Hamiltonian. By quenching the system between different Floquet-induced artificial gauge fields with different equilibrium ground states, we observe Bose conden-

sation of quench-excited atoms on time scales faster than heating. We explore two effective field configurations: a staggered 2π-state with topologically trivial band structure related to the field-free state by a gauge transformation; and a nontrivial staggered π-flux model, in which the band displays minima at two inequivalent points in the lowest Brillouin Zone (BZ). In both cases, when the gauge-field quench is applied to a Bose Einstein condensate, the resulting sudden shift of the equilibrium ground state quasi-momentum leads to fast heating followed by re-condensation at the new band minima of the *effective* Hamiltonian of the driven system. Finally, we observe collision-induced relaxation between the two the inequivalent minima of the π flux model.

5.1 Theory

A detailed study of the Floquet band structures is not only important for understanding what physics can be realized, but it is also essential for navigating through parameter space and getting to the desired physics. In this section, we introduce the theoretical descriptions of for our circularly driven optical lattice in both the tight binding limit and the extended basis picture.

In order to introduce the $n\pi$-flux model, we first revisit the two level tight binding description from Eq. 2.53. Following [45], we add in a circular drive, which acts on each site, making the driven tight binding model:

$$H = \sum_i \sum_{\mu=1}^{4} a_i^\dagger b_\mu + \Delta \sum_i b^\dagger b_i - \sum_{i \in \mathcal{A}\cup\mathcal{B}} \left(F(t)\cdot r_i\right) a_i^\dagger a_i + \text{H.C.}, \tag{5.1}$$

where $\mathcal{A}, \mathcal{B}$ represent the two different sublattices with energy offset Δ, and $F(t)$ is the driving force that couples the two sublattices. The geometry of the lattice is shown in Fig. 5.1.

The lattice unit cell consists of two sites, which we label $\mathcal{A}$-sites and $\mathcal{B}$-sites. The ele-

mentary lattice vectors are $\mathbf{a_1}$ and $\mathbf{a}_2$, where $|\mathbf{a}_i| = \lambda/\sqrt{2}$ and λ is the wavelength of the lattice beams. The reciprocal lattice vectors are defined by $\mathbf{a}_i \cdot \mathbf{b}_j = 2\pi\delta_{ij}$, so that $|\mathbf{b}_i| \equiv k_L$, where $k_L = \sqrt{2}k_R$ and $k_R = 2\pi/\lambda$ is the single photon recoil momentum of light with wavelength λ.

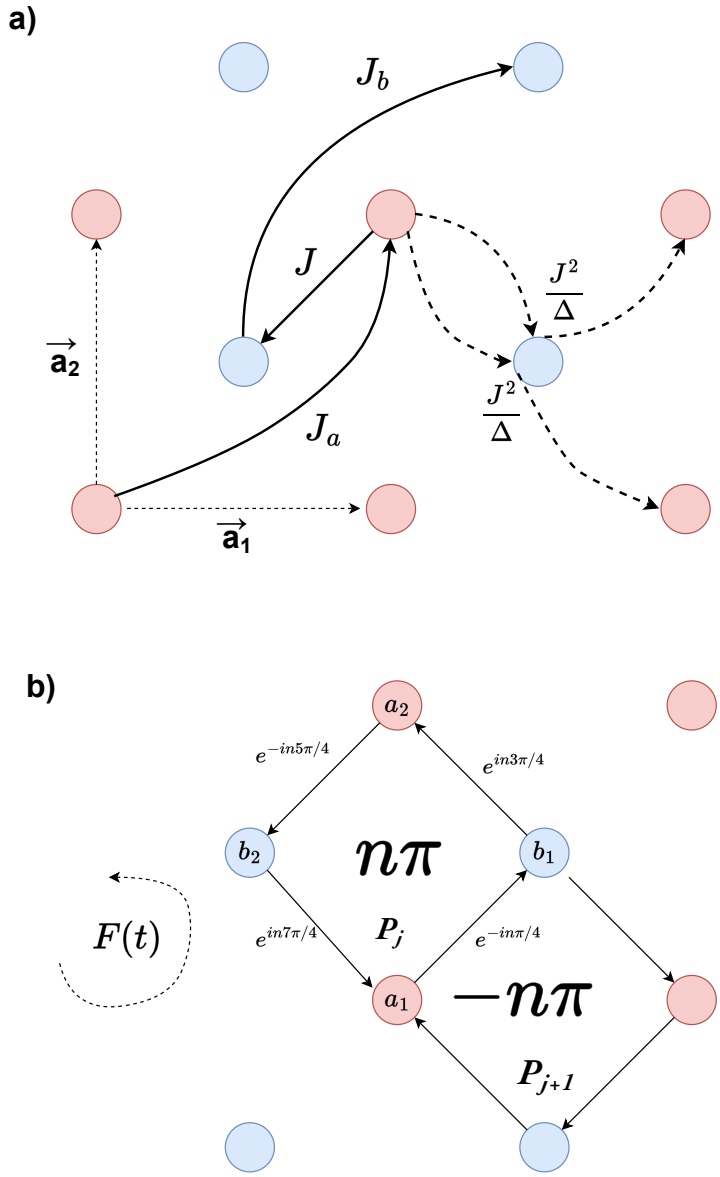

Figure 5.1: Schematic of the effective lattice. (a) Static tunneling terms: The two sublattices (red and blue) are offset in energy by $\hbar\Delta$. The tunneling processes up to order J^2 are indicated. Each site is coupled to its four nearest neighbors on opposite sublattice with coupling strength J. In the presence of Δ, direct first-order tunneling is suppressed, leaving resonant second-order tunneling to next-nearest neighbors on the same sublattice, which scales as $\sim J^2/\Delta$. For consistency, direct next-nearest neighbor tunneling processes, with strengths J_a and J_b that scale as $\sim J^2/E_R$, are also included. (b) Effective gauge field model: The periodic drive, $F(t)$ restores nearest-neighbor tunneling between different sublattices, with complex tunnel coefficients along the edges of each plaquette ($\mathcal{P}_j$), as shown. Near-resonant driving, $\Delta \simeq n\omega$, results in an effective two band system that exhibits a staggered-$n\pi$ flux.

For circular shaking, the driving force takes the form $F(t) = K\left(\cos(wt)\hat{x} + \sin(\omega t)\hat{y}\right)$. In order to generalize the theory to multi-photon resonances, we make the following definition $\delta = \Delta - n\omega$. Performing a unitary transformation $U(t) = \Pi_i \exp(-i\chi_i(t)a_i^\dagger a_i)$, one obtains a transformed Hamiltonian:

$$H = -J\sum_{i\in\mathcal{A}}\sum_{\mu=1}^{4}\exp(iK_0\sin(\omega t-\phi_\mu)-iN\omega t)b_{i+\mu}^\dagger a_i + \delta\sum_\mu b_\mu^\dagger b_\mu, \tag{5.2}$$

where ϕ_μ represents the lagging phases. The first term in Eq. 5.2, can be seen as a time dependent tunneling term, which we can express as a Fourier series using the Jacobi-Anger expansion:

$$J_\mu(t)/J = \sum_\ell \mathcal{J}_{\ell+n}(K_0)e^{-i(\ell+n)\phi_\mu}e^{i\ell\omega t}. \tag{5.3}$$

In the high frequency limit, the tunneling element is given by the time average of $J_\mu(t)$, which is just the $\ell = 0$ component.

$$\langle J_\mu(t)\rangle = J\mathcal{J}_n(K_0)e^{-in\phi_\mu}. \tag{5.4}$$

A sample time averaging of the phases is shown in Fig. 5.1. Given that a complex conjugate is associated with tunneling in opposite directions, we see that the phase accumulated by a particle tunneling around one plaquette (for n=1) is given by $\frac{\pi}{4}(-1+3-5+7) = \pi$.

An interesting feature of this tight binding model is that when we allow for the n photon resonance, the phase acquired, ϕ_μ is given as $n\phi_\mu$, so the net phase on a plaquette is $n\pi$. We also note that similar to [74] we can write this tight binding model in real space as

$$H = \sum_{\mathcal{P}} e^{-i\pi/4}b_1^\dagger a_1 + e^{3i\pi/4}a_2^\dagger b_1 + e^{-5i\pi/4}b_2^\dagger a_2 + e^{7i\pi/4}a_1^\dagger b_2 + \text{H.C.}, \tag{5.5}$$

where $\mathcal{P}$ indicates a sum over plaquettes and $a_{1/2}, b_{1/2}$ indicate the site of a plaquette as shown in Fig. 5.1.

In order to further analyze the system, we perform a spatial Fourier transformation into quasimomentum space:

$$a_q^\dagger = \sum_{\mathcal{A}} a_i^\dagger e^{i\mathbf{q}\cdot r_i} \tag{5.6a}$$

$$b_q^\dagger = \sum_{\mathcal{B}} b_j^\dagger e^{i\mathbf{q}\cdot(r_j-\delta_1)}. \tag{5.6b}$$

Following [45], we find that the momentum space Hamiltonian can be expressed as

$$H = -J\sum_q b_q^\dagger a_q \sum_{\ell=-\infty}^{\infty} \underbrace{\mathcal{J}_{n+\ell}(K_0)G_{n+\ell}(\mathbf{q})}_{H_\ell} e^{i\ell n\omega t} + \delta\sum_q b_q^\dagger b_q + \text{H.C.}, \tag{5.7}$$

where the structure factors, G_s are given by:

$$G_s(\mathbf{q}) = 1 + e^{-is\pi/2}e^{i\mathbf{q}\cdot\mathbf{a_1}} + e^{is\pi}e^{i\mathbf{q}\cdot(\mathbf{a_1}+\mathbf{a_2})} + e^{is\pi/2}e^{i\mathbf{q}\cdot\mathbf{a_2}}. \tag{5.8}$$

The first 3 G_s are shown in Fig. 5.2

Following the high frequency expansion from Eq. 2.10, we can write this Hamiltonian as $H = H_F^{[0]} + H_F^{[1]} = H_0 + \frac{1}{\omega}\sum_{\ell=1}^{\infty}\left(\frac{1}{\ell}\right)[H_\ell, H_{-\ell}]$, where

$$H_0 = -J\sum_q \left(b_q^\dagger a_q\, \mathcal{J}_n(K_0)G_n(\mathbf{q}) + a_q^\dagger b_q \mathcal{J}_n(K_0)G_n^*(\mathbf{q})\right) \tag{5.9}$$

is the time averaged component. At this lowest order, the bands for this system are mirror sym-

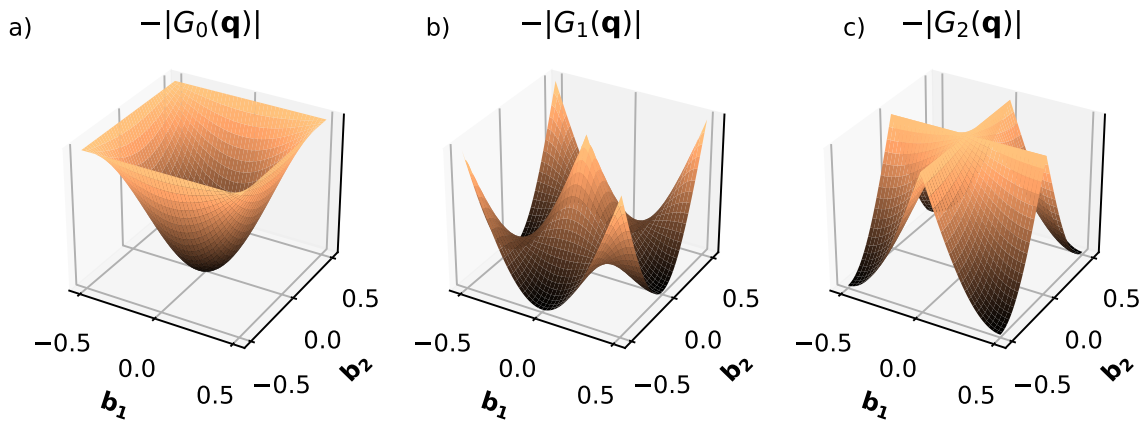

Figure 5.2: First three structure factors, $G_s(\mathbf{q})$, displayed as $-|G_s(\mathbf{q})|$, which is the shape of the bands at first order in the high frequency expansion.

metric and are given by

$$\varepsilon_{\pm} = \pm J|\mathcal{J}_n(K_0)G_n(\mathbf{q})|. \tag{5.10}$$

The higher order Floquet contribution is given by

$$H_F^{[1]} = \frac{J^2}{\omega}\sum_{\ell}\frac{1}{\ell}\left(\sum_q(-b_q^\dagger b_q + a_q^\dagger a_q)\underbrace{\left[\mathcal{J}_{\ell-n}^2(K_0)|G_{n-\ell}(\mathbf{q})|^2 - \mathcal{J}_{n+\ell}^2(K_0)|G_{n+\ell}(\mathbf{q})|^2\right]}_{\mathcal{B}_\ell(K_0,\mathbf{q})}\right), \tag{5.11}$$

which can be treated as a two level system for each quasi-momentum. Writing H as $\psi^\dagger\mathcal{H}\psi$ where $\psi = (a_q, b_q)^T$ is a spinor in the sublattice basis, gives a 2x2 matrix for each q,

$$\mathcal{H}_q = \begin{pmatrix} \frac{J^2}{\omega}\sum_\ell\left(\frac{1}{\ell}\right)\mathcal{B}_\ell(K_0,\mathbf{q}) & -J\mathcal{J}_n(K_0)G_n(\mathbf{q}) \\ -J\mathcal{J}_n(K_0)G_n^*(\mathbf{q}) & \delta - \frac{J^2}{\omega}\sum_\ell\left(\frac{1}{\ell}\right)\mathcal{B}_\ell(K_0,\mathbf{q}) \end{pmatrix} \tag{5.12}$$

Diagonalization of $\mathcal{H}_q$ gives the two energy bands.

Due to the K_0 dependence of H_0, the lowest order (in $1/\omega$) term, $\mathcal{J}_n(K_0)|G_n(\mathbf{q})|$ vanishes as $K_0 \to 0$. The next order term, $H_F^{[1]}$, scales as $J\mathcal{J}_0(K_0)/\omega \to J/\omega$, which is dominant in

the low drive limit. However, given that $n\omega \approx \Delta \gg J$, one can always find a K_0 where H_0 is dominant.

The condition, set by H_0, that the effective flux is $n\pi$ through a plaquette will result in different quasimometum for which the bands are minima. The staggered-2π case ($n = 2$) has a single minimum at the point $q_{\text{min}} = M = \frac{1}{2}(\pm\mathbf{b_1} \pm \mathbf{b_2})$, see Fig. 5.2(c) where the band structure is proportional to $-G_2(\mathbf{q})$. This band is equivalent to the zero flux case, Fig. 5.2(a), up to a gauge transformation that translates $\mathbf{q}' \to \mathbf{q} + \frac{1}{2}(\pm\mathbf{b_1} \pm \mathbf{b_2})$. While the low energy physics confined to the driven lattice is gauge-independent [75], for synthetic magnetic fields, the underlying gauge is experimentally accessible and has physical significance. In particular, a sudden shift in the band minimum from $\mathbf{q} = \Gamma \equiv (0, 0)$ to point M will cause heating and require rethermalization to relax to the new, shifted ground state.

For the staggered-π case ($n = 1$), the ground band has two degenerate minima at inequivalent points in the BZ (See Fig. 5.2(b). The two-fold degeneracy persists in the presence of interactions, and is indicative of non-zero flux [76]. In the gauge appropriate for our experimental realization, the minima occur at $q_{\text{min}+} = X_+ = \pm\frac{1}{2}\mathbf{b_1}$ and $q_{\text{min}-} = X_- = \pm\frac{1}{2}\mathbf{b_2}$. When $\delta = 0$, there are two inequivalent Dirac points ($\mathbf{q}_{\text{D}i}$), where the gap to the second band (not shown in Fig. 5.2) closes linearly with $|\mathbf{q} - \mathbf{q}_{\text{D}i}|$. The bands are topologically non-trivial exactly at the gap closing.

5.1.1 Next Nearest Neighbor Tunneling

In order to fully capture the behavior, we also consider the Floquet treatment of the next nearest neighbor tunneling. In the static case, as described in section 2.8.1, there are tunneling

terms, J_a, J_b, which allow for tunneling of the form $-J_a a_i^\dagger a_{i+\mu} - J_b b_i^\dagger b_{i+\mu}$ (μ indicating any of the 4 next nearest neighbors through the other sublattice). Performing the same unitary transformation for either of these terms, we see that driving modifies the two site tunneling such that the Fourier decomposition is

$$J_{a/b,\mu} = J_{a/b} \sum_\ell \mathcal{J}_\ell(2K_0) e^{-i\ell\phi_\mu} e^{i\ell\omega t} \tag{5.13}$$

The appearance of $2K_0$ arises due to the distance between the sites being $2d$, which results in $F \cdot r$ doubling. Since tunneling is between same sites, Δ is irrelevant and ℓ is not shifted to $\ell \pm n$ as with the coupling between different sublattices. It is intuitive to note that the time averaged component will be $J_{a/b}\mathcal{J}_0(2K_0)$, which is the same order Bessel function as with the renormalization of the static bands in the square lattice (with the difference that the argument is $2K_0$).

Performing the Fourier transform into momentum space, we obtain the next nearest neighbor contribution for the time-averaged component of H:

$$H_{NNN,A/B} = -J_{a/b}\, \mathcal{J}_0 \left(2\cos(\mathbf{q}(\mathbf{a_1} + \mathbf{a_2})) + 2\cos(\mathbf{q}(\mathbf{a_1} - \mathbf{a_2}))\right) \tag{5.14}$$

Making the following definitions,

$$H_1 = J\mathcal{J}_n(K_0) G_n(\mathbf{q}) \tag{5.15a}$$

$$H_2 = \frac{J^2}{\hbar\omega} \sum_\ell \frac{1}{\ell} \left[\mathcal{J}^2_{\ell-n}(K_0)|G_{n-\ell}(\mathbf{q})|^2 - \mathcal{J}^2_{n+\ell}(K_0)|G_{n+\ell}(\mathbf{q})|^2\right] \tag{5.15b}$$

$$H_{ab} = \mathcal{J}_0(2K_0) \left(2\cos(\mathbf{q}(\mathbf{a_1} + \mathbf{a_2})) + 2\cos(\mathbf{q}(\mathbf{a_1} - \mathbf{a_2}))\right), \tag{5.15c}$$

the 2x2 Hamiltonian can be expressed as

$$H_q = \begin{bmatrix} -H_2 - J_a H_{ab} & H_1 \\ H_1 & \delta - J_b H_{ab} + H_2 \end{bmatrix}. \tag{5.16}$$

Diagonalization of this Hamiltonian gives the following energy bands

$$\varepsilon_{\pm}(\mathbf{q}) = \frac{1}{2}\left[\delta - 2H_2 - H_{ab}(J_a + J_b) \pm \sqrt{4|H_1|^2 + (\delta + H_{ab}(J_a - J_b))^2}\right] \tag{5.17}$$

5.1.2 Extended Basis Picture

The tight binding description from Eq. 5.17 is only an approximation to the full lattice description. The inclusion of second order tunneling, which scale as $J_a \propto J^2/E_R$, are required, as they are dominant at low drive strengths. At high drive strengths, the two band model breaks down as a result of coupling to higher bands. In order to account for higher bands and the driving-induced shifts, one can treat the problem in the extended basis, as discussed in section 2.10.3. In the co-moving frame, the Hamiltonian for the periodically driven lattice can be expressed as

$$H_{cm} = \frac{p^2}{2m} + V_{LAT}(x, y) - \omega\left(\delta_x \sin(\omega t) p_x + \delta_y \sin(\omega t + \phi) p_y\right) \tag{5.18}$$

Recalling the matrix elements of the extended basis Hamiltonian are given by

$$\langle n'm'|H|nm\rangle = \int_0^T dt \langle n'|H|n\rangle e^{-i(m'-m)\omega t}, \tag{5.19}$$

from the expression, Eq. 5.18, the terms $H_{\pm 1}$ can be expressed, for a circular drive ($\delta_x = \delta_y, \phi = \pi/2$), as

$$H_{\pm 1} = K_0(p_x + ip_y), \tag{5.20}$$

where the complex momentum arises from the circular driving (this can be extended to include a factor of $e^{i\phi}$ for other drive trajectories), representing the coupling between two states in H that differ by ω. It is of interest to note that in the tight-binding model, we put in an n-photon resonance by hand, whereas in the extended basis, there are no direct $n\omega$ couplings, as the Fourier component of the drive at $n\omega$ is 0. We note that the same multi-photon resonance bands will show up, but these result from intermediate couplings.

The numerical computation of the full extended basis results in a system of $(2n_T + 1) \times (2n_L + 1)^2$ lattice bands, where n_T, n_L are the number of time and lattice states used in the truncated problem. For typical values of $n_T = 5, n_L = 5$, this results in 1331 bands calculated. To find the relevant bands of interest, one can see that the lowest $(2n_T + 1)$ bands at $\omega = 0$ are adiabatically connected to the ground band of the static lattice as $\omega \to 0$. The particular state adiabatically connected to the ground band in the dressed picture will be unshifted, which means at a fixed frequency, the static ground band will be close in energy to that undriven value.

Fig. 5.3 shows an example of how the $\mathbf{q} = [\Gamma, M, X_+]$ points evolve for the bands at $K_0 = 1.5$ as a function of ω. At $\omega = 0$ Hz, the clusters of different solutions represent the static bands, with a Floquet multiplicity of $2n_T + 1$. The offset bands in a particular cluster are a numerical result of truncating the full Hamiltonian at a fixed number of blocks. As the drive frequency is increased, the higher bands are dressed resulting in crossings, many of them avoided

as a result of coupling between the dressed bands.

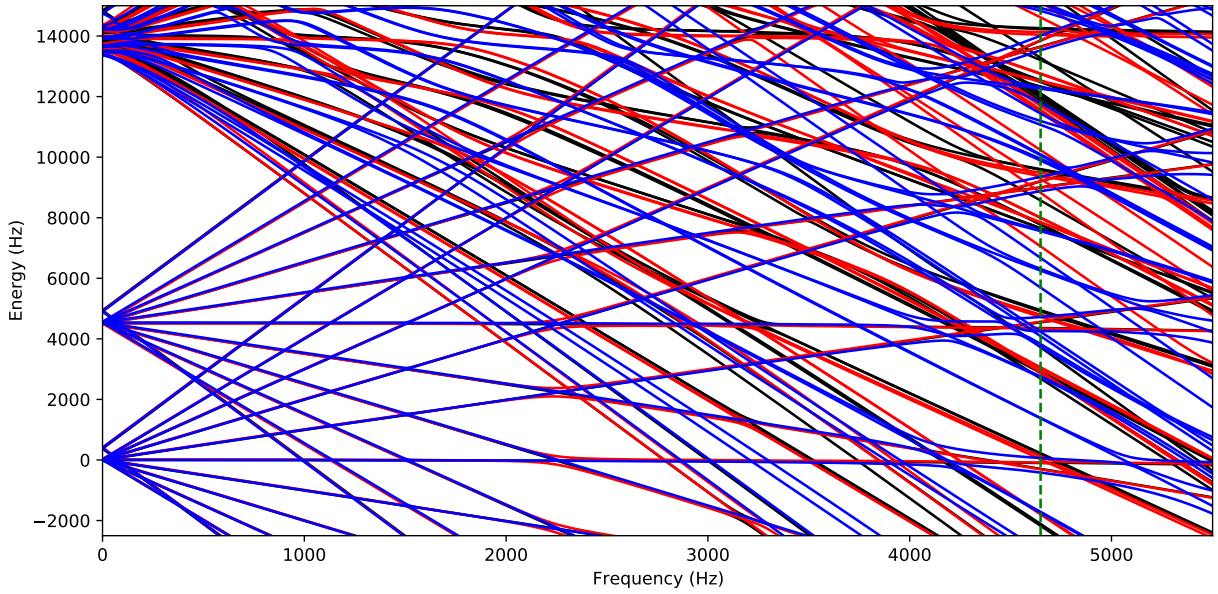

Figure 5.3: Plot of energy bands at $\mathbf{q}$=Γ (red), M (black) and X_+ (blue) as a function of the drive frequency at a fixed $K_0 = 1.5$. The vertical green dashed line indicates the $\mathbf{q} = \Gamma$ energy gap between the static bands.

An interesting observation from the frequency dependence is that in the presence of driving, the frequency at which the Dirac point occurs (where the bands linearly cross), shifts away from the tight binding value of Δ, which we approximately take to be the $\mathbf{q} = \Gamma$ gap between the two static bands. Figure 5.4 shows how the dressed band gap changes as a function of the drive strength. At $K_0 = 0$, the dressed bands at $\mathbf{q} = \Gamma$ are separated in energy by $\Delta - \omega$. As the drive strength increases, the gap shifts, and this frequency becomes resonant at different K_0. This effect is a result of coupling to higher bands and is therefore not directly captured in the tight-binding model. In the tight binding model, adjusting the drive strength only adjusts the coupling strengths, not the resonance condition. Performing experiments in this regime, such as exploring topological band structures, which have topological regimes for parameter regimes on the order of 100 Hz, would require careful calibration of these K_0 shifts.

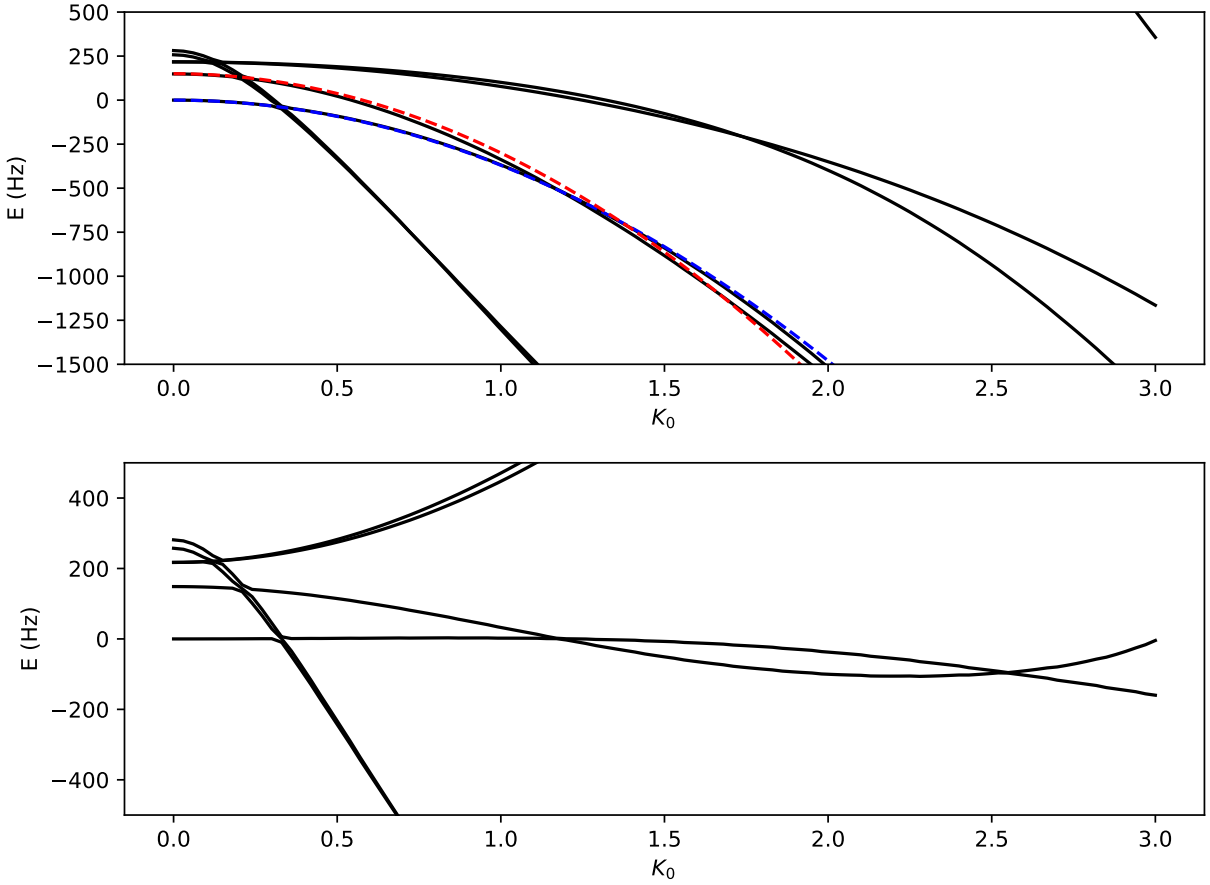

Figure 5.4: K_0 dependent shifts for a fixed ω = 4500 Hz at $\mathbf{q} = (0, 0)$, which is 180 Hz detuned from the static gap. The top image shows the raw numeric calculations, which have a $-K_0^2$ dependence. The red (blue) line represents a quadratic fit to the lower (upper) band in the two level system. The lower panel is the same information, just subtracting out the quadratic K_0 dependence from the blue curve in the upper panel. Note that there is still a downward slope on the relevant energy band as K_0 increases. This is a result of higher band couplings and additional corrections needing to be accounted for in the high driving limit.

5.1.3 Mapping Tight Binding to Extended Basis

The tight binding description can be considered a good parameterization of the full behavior in the limit of isolated bands. We can use the extended basis calculations for a comparison to see when and how the tight binding model fails. In the full extended basis picture, the coupling to higher bands results in several effects. First, off-resonant coupling to higher bands modifies the effective tight binding parameters, which must be accounted for in order to correctly navigate through parameter space. In addition, the coupling to higher bands breaks the symmetry between the $\mathcal{A}$ and $\mathcal{B}$ sites: the $\mathcal{B}$ sites are more strongly coupled to the excited bands, which leads to larger micromotion, for example. More consequentially, resonant n-photon coupling gives rise to dramatic shifts in the band shapes and direct heating to higher bands.

These effects can be seen in Fig. 5.5, which shows the extended basis calculation of the Floquet quasi-energies as a function of drive frequency, ω, at $\mathbf{q} = [\Gamma, M, X_{\pm}]$, the three different points within the BZ where the bands exhibit minima. Fig. 5.5(a) shows the lowest quasi-energies in the full extended system, where the boxes indicate the regions near the ω, 2ω resonance conditions. Zooming into the $n = 1$ resonance, Fig. 5.5(b), one can see that the frequency at which the two bands cross at $\mathbf{q} = 0$ (black lines) is no longer equal to the $K_0 = 0$ resonance condition (green dashed line), indicating a shift in the tight-binding δ. In addition, avoided band crossings are evident for all three $\mathbf{q}$ in the BZ. Fig. 5.5(c) shows the band structure calculated near resonance (black curve) as well as the tight binding fit (red curve). We find that there are many avoided-crossing couplings for the $n = 1$ resonance, which results in significant heating when loading the condensate into the Floquet lattice. There are regions in parameter space below resonance, however, that don't have strong higher band coupling and yet still have band minima at

the staggered π-flux condition $\mathbf{q} = X_+$. These regions, which produce well isolated bands with minimal coupling, are explored in Fig. 5.6

With a detailed understanding of the single particle Floquet band structure, we are able to identify conditions where artificial gauge fields are present and to accurately navigate through parameter space in order to prepare initial states in the artificial fields.

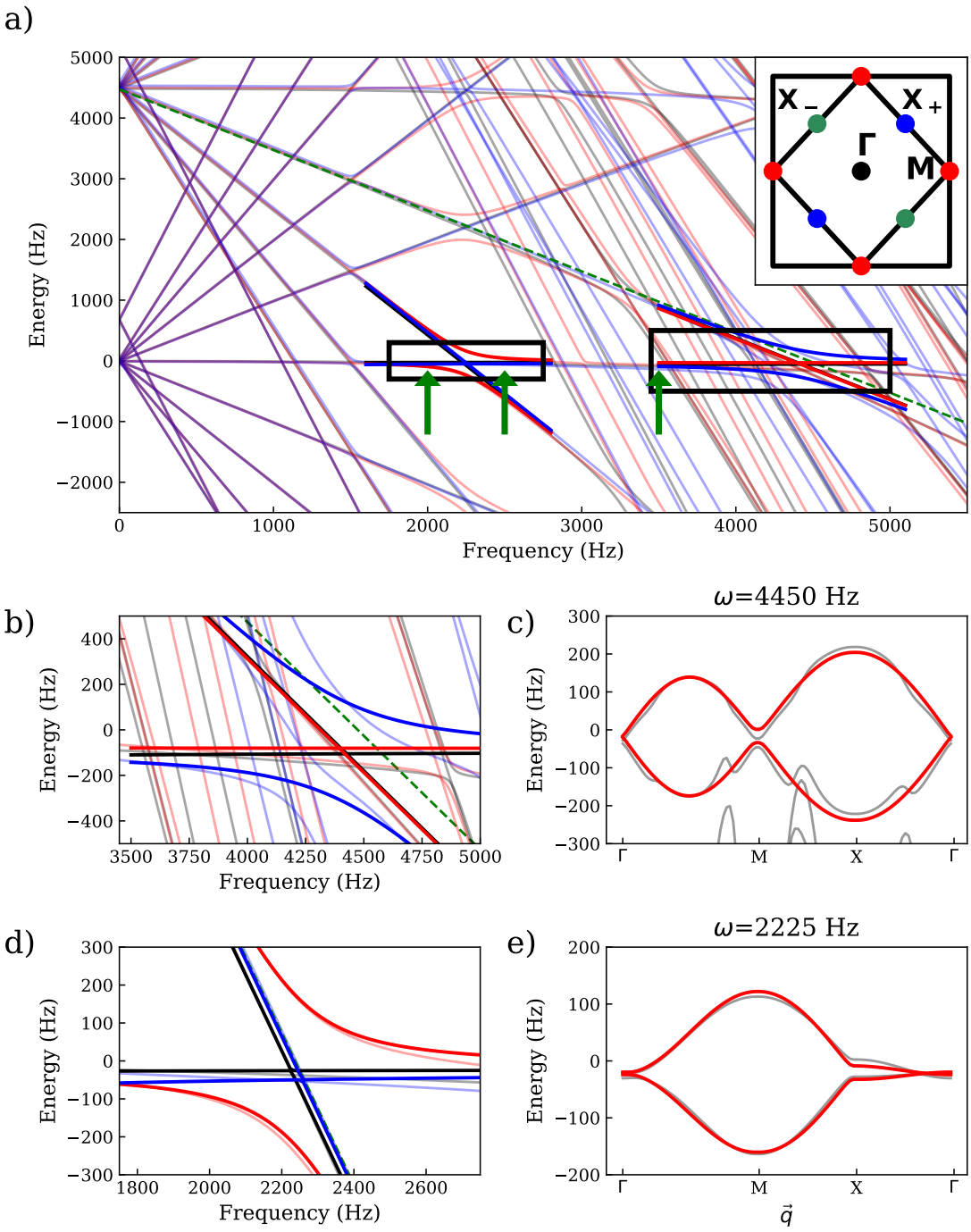

Figure 5.5: Extended basis calculation of the Floquet quasi-energy spectrum vs. drive frequency ω, shown for $\mathbf{q} = \Gamma$ (black), $\mathbf{q} = M$ (red) and $\mathbf{q} = X$ (blue) at $K_0 = 2.0$. Transparent lines indicate the extended basis calculation and solid lines indicate a tight binding fit. (b),(d) show the spectra zoomed into the black rectangular regions in (a). The green dashed lines indicate the line $\Delta - \omega$. (c) and (e) show the resulting bands along the symmetry line ($\Gamma - M - X - \Gamma$) at a fixed frequency for the full matrix calculation (black) and the tight binding approximation (red). The green arrows in (a) represent the load conditions in Fig. 5.6

5.2 Experiment

In a first set of experiments, we adiabatically load the BEC, initially at $\mathbf{q} = 0$ in the static lattice, into a shaken lattice. These experiments allowed us to characterize the Floquet lattice, and proved that there were conditions at strong driving where equilibrating in an effective field is possible.

5.2.1 Adiabatic Loading

Frequency Space

We begin with a condensate at $\mathbf{q} = \Gamma$ and turn on the lattice shaking in a fixed amount of time, which was chosen to be 12ms, corresponding to 24-40 drive periods. Measurements were taken at various drive frequencies in a $7.2E_R$ total final lattice depth, with a $\mathbf{q} = \Gamma$ gap between the two lowest bands equal to $h \times 4.7$ kHz. Figure 5.6 shows the resulting time of flight images obtained after the 12ms ramp into the Floquet lattice at a fixed frequency, followed by an abrupt turn off of the lattice. The presented images are an average over individual images taken at different drive phases, since the micromotion during a drive phase results in the instantaneous momentum composition varying dramatically within a drive period.

The change in the condensation quasimomentum at different drive frequencies can be attributed to the change in effective flux. Below the $n = 2$ resonance, for sufficient drive amplitudes, the condensate occurs at the single minimum associated with the staggered 2π flux in our gauge. This can be seen in the TOF image in Fig. 5.6(a), where the condensate in the single minimum, within the space-periodic BZ, is projected onto the four free particle momenta $\frac{1}{2}(\pm\mathbf{b}_1 \pm \mathbf{b}_2)$ before the TOF measurement.

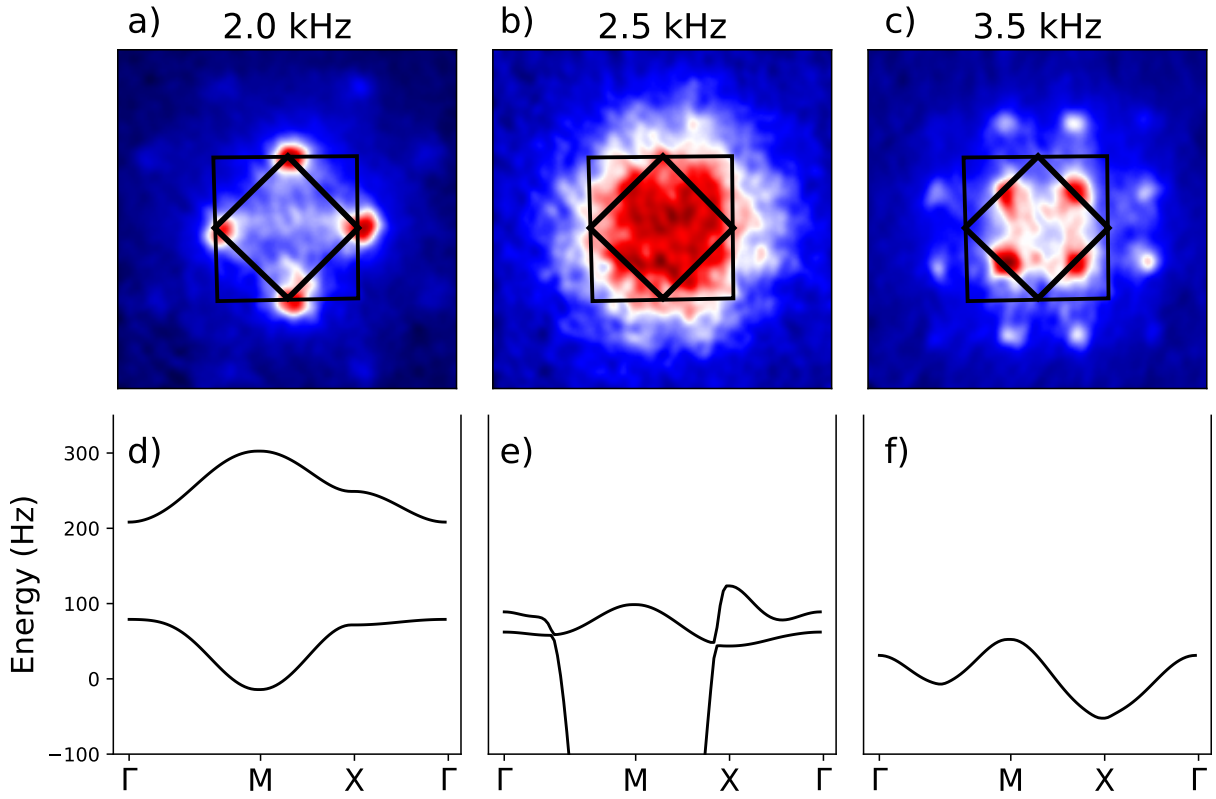

Figure 5.6: a-c: Micromotion-averaged time-of-flight images of condensates loaded adiabatically into the Floquet lattice at different drive frequencies. In all cases, the states were prepared by ramping on the shaking in 12 ms at fixed frequency to a final drive strength $K_0 = 2$. The frequencies were a) $\omega = 2\pi$ 2.0 kHz $/ < \Delta/2$, b) $\omega = 2\pi$ 2.5 kHz $\omega \simeq \Delta/2$ and c) $\omega = 2\pi$ 3.5 kHz$< \Delta$. The frequencies chosen are represented in Fig. 5.5 (a) as the green arrows

Below the $n = 1$ resonance, the condensate occurs at the two inequivalent minima associated with the staggered π flux. For the ideal staggered π-flux model, the condensate is expected to be "fragmented", since there is no density spatial modulation when the two condensates are present, which would prefer a particular superposition of the $X_\pm$ states. For a fragmented BEC, one would not expect a well-defined relative phase or relative population of the condensates [77]. We found that while the ratio of population in X_+/X_- was sensitive to the ellipticity of the drive, for a fixed drive pattern the condensate consistently relaxed into a well-defined relative population of X_+ and X_-, with small fluctuations around the measured ratio. This lack of fluctuations was

also observed in [63], and is indicative (although not conclusive) of a non-fragmented condensate. We experimentally find that when we adiabatically load into the condition where the population are approximately balanced (which occurs for circular shaking), turning off the drive and projecting back to the static lattice results in a rotation of the condensate between the $X_{\pm}$ points. This effect essentially measures the initial relative phase of the $\mathcal{A}$ and $\mathcal{B}$ components of the X_{+} and X_{-} states, as is shown in Fig. 5.7. We observe oscillations between the two equivalent $\mathbf{q}$ points for both $X_{\pm}$. Although the measurement cannot provide information about the relative phase of the X_{+} and X_{-} components, we find that the relative population is approximately constant, as displayed in the histogram (Fig. 5.7 (d)).

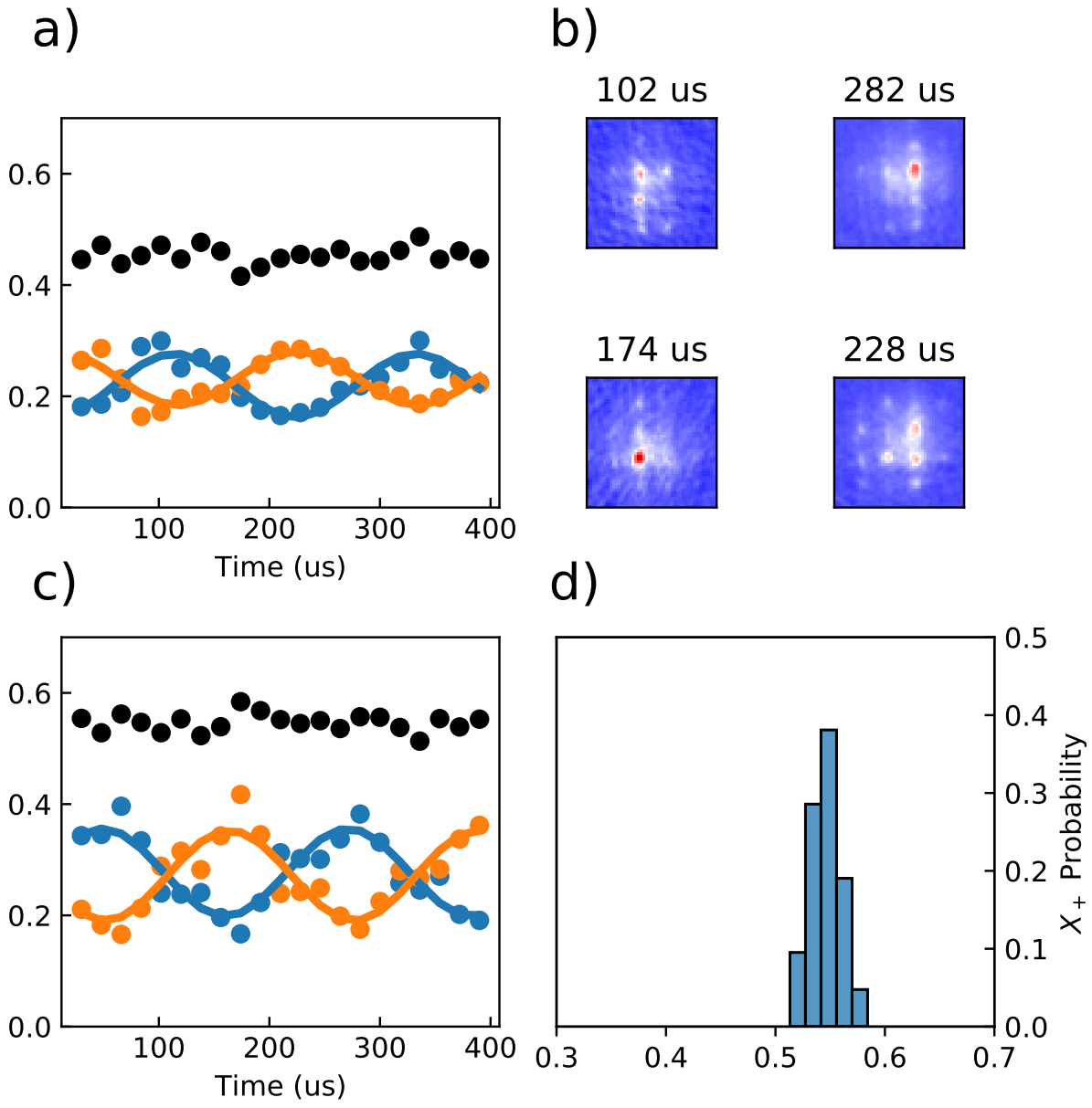

Figure 5.7: Dynamics of a condensate adiabatically loaded into $X_\pm$ and quenching back to the static lattice. We observe oscillations within X_+ (a) and X_- (c), representing the phase evolution at the static lattice tilt, $\Delta(\mathbf{q} = X)$. (d) shows that there are small fluctuations around ratio of populations over time.

K_0 Space

For the ideal case band structure (Eq. 5.10), the band minima associated with the staggered flux appear for any non-zero drive K_0. At small K_0 the second order terms are dominant, and one

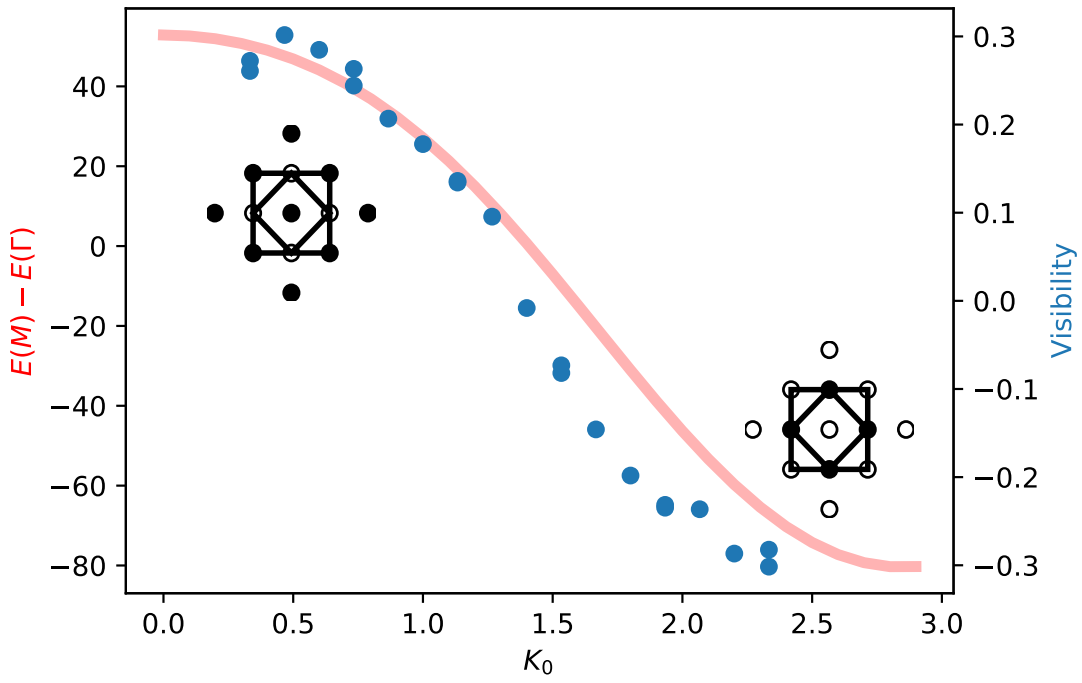

Figure 5.8: Visibility between $\mathbf{q} = \Gamma$ and $\mathbf{q} = M$ vs K_0. The red data indicate the measured visibility between the two $\mathbf{q}$ points. The black curve indicates the energy difference vs K_0, showing that the inversion of band minima is dependent on both ω and the drive strength.

needs a sufficient drive to make the flux terms dominant. At a given frequency, the band minimum will therefore depend on the drive strength, where stronger strives lead to the flux terms being dominant. For the 2π staggered flux, which has an ideal-case minimum at M, there is a region in low K_0 where $E(\Gamma) < E(M)$. We observe this change in minima with drive frequency in Fig. 5.8, where we adiabatically load at $\omega/2\pi$ =2kHz to a given K_0 in 12ms and measure a visibility between the populations at $\mathbf{q} = \Gamma$ and $\mathbf{q} = M$. We find the visibility between the $\mathbf{q}$ points varies with K_0 as the energy difference of the two minimum switches sign. In order to have the 2π flux terms dominate the spectrum, the drive must reach values of $K_0 \simeq 2.5$.

Ramp Time

The timescale for adiabatic loading experiments was chosen to optimize the condensate in the band minima. We found that beyond a 12 ms ramp time, there were no additional improve-

ments in the time of flight images. The effect of varying the ramp time is shown in Fig. 5.9, where too short a time results in the condensate either being at the $\mathbf{q} = \Gamma$ point, or a mostly thermal cloud starting to condense at the minima.

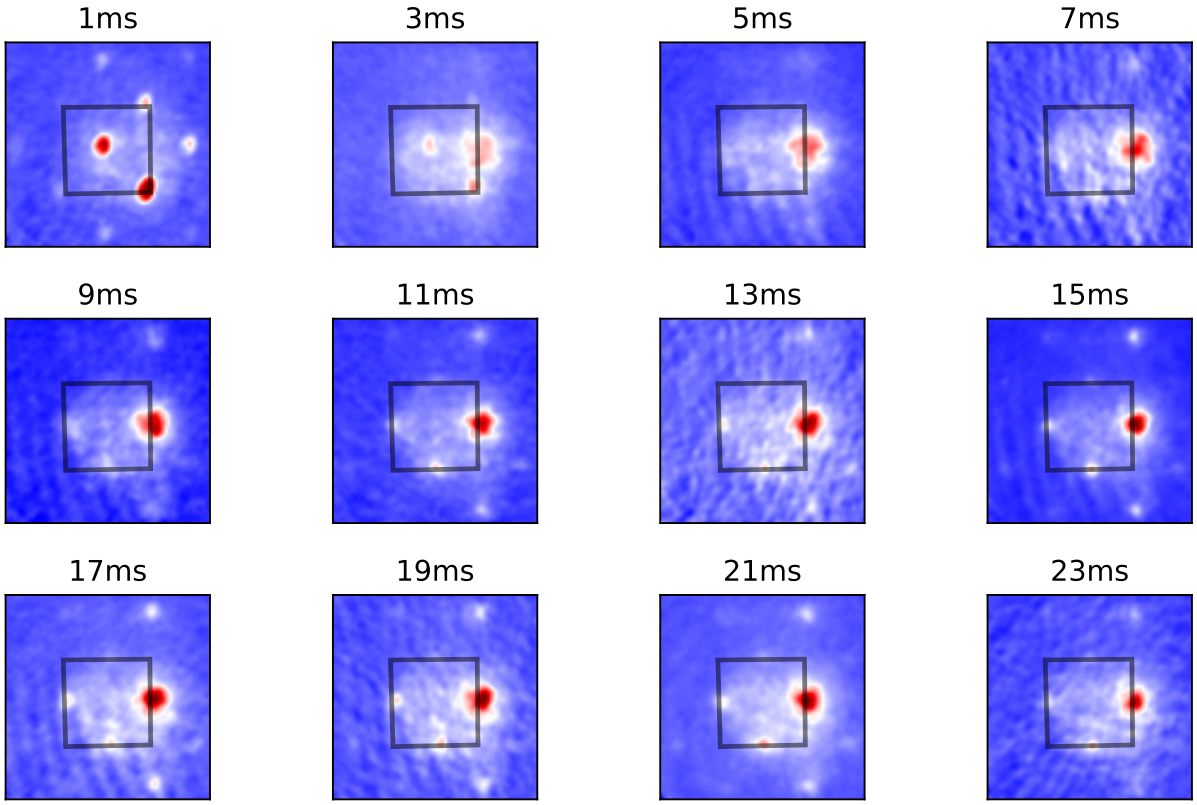

Figure 5.9: Thermalization of condensate into the $\mathbf{q} = M$ point as the ramp time is increased at K_0=2 and $\omega/2\pi$=2kHz. The images were taken at the same fixed end phase of the drive.

5.2.2 Heating from Band Sweeps

The near resonance conditions, $n\omega \simeq \Delta$, are clearly the most interesting conditions to study, however we found that coupling to higher bands outside $\mathcal{A}$ and $\mathcal{B}$, complicated studies, particularly near $\omega \simeq \Delta$. In this section, I discuss an experiment that studies the band crossings in the Floquet system by performing Laundau-Zener sweeps through the Dirac points. By preparing our atoms in one of the Floquet bands by ramping up the drive off-resonantly, and then sweeping

the frequency. If a strongly coupled band is present, a fraction of atoms will be transferred to the excited band. We experimentally observed the Landau-Zener transition across the $n = 2$ resonance for a $7.2E_R$ lattice, with the undriven $\mathbf{q} = \Gamma$ gap of $\Delta = 5.25$ kHz. The Floquet band that we load into depends on the initial condition ($\omega < \Delta/2$ or $\omega > \Delta/2$), so we performed the sweep starting from both sides of resonance.

Red→ Blue

We begin with a BEC at $\mathbf{q} = \Gamma$, K_0 and ramp on the drive in 12ms at 2.5 kHz ($\omega < \Delta/2$) and $K_0 = 2$. The frequency is ramped to the final value in a fixed 5ms and then a bandmap procedure is performed, which converts the population in a given BZ into its free particle equivalent, to observe the populations. Sweeping through resonance results in a transfer of atoms into both the second and third static band, whereas we expect the second band to become populated.

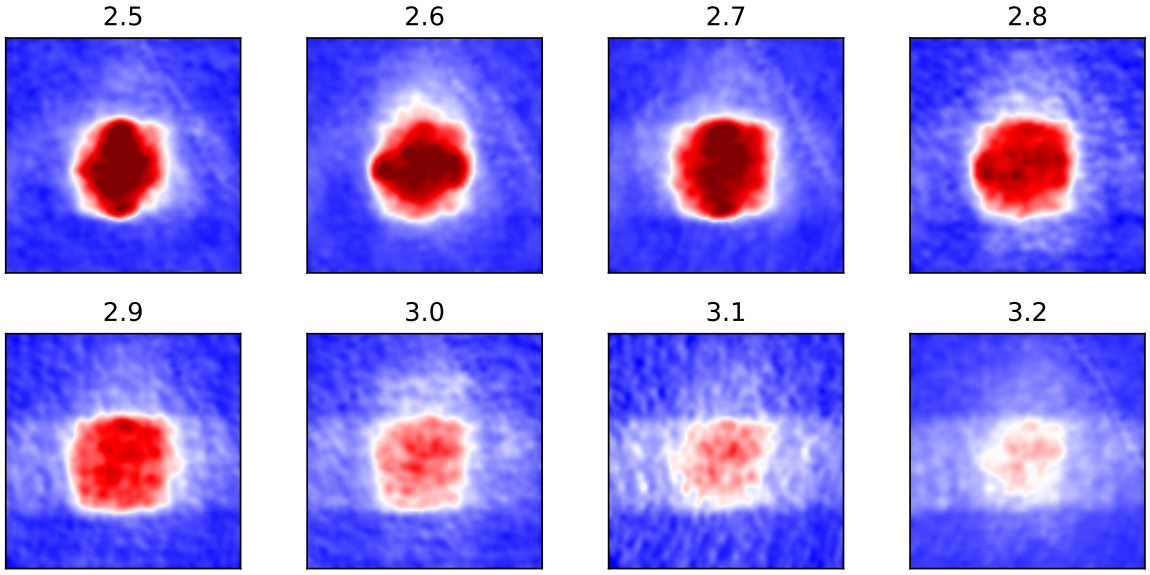

Figure 5.10: Sweeping the drive frequency from 2.5 kHz to a different final value across the $n = 2$ resonance, where $\Delta = 5.25$ kHz.

Blue → Red

For the case of starting with $\omega > \Delta/2$, we ramped K_0 from 0 to 2 in the same 12ms, and then swept the frequency to the final value. By starting above resonance, we adiabatically load into the other relevant Floquet band and expect transfer to the second band again. We observe that there is no transfer out of the initial band for these sweeps.

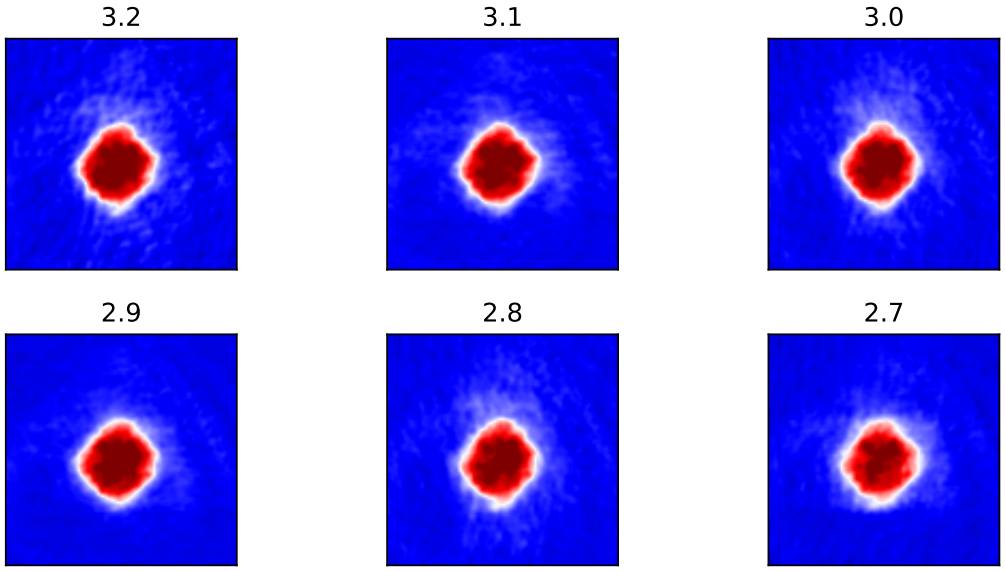

Figure 5.11: Sweeping the drive frequency from 3.3 kHz to a different final value across the $n = 2$ resonance, where $\Delta = 5.25$ kHz.

This is an interesting observation that the population transfer depends on the initial condition. As shown in Fig. 5.12, we see that there are higher band couplings that happen right beyond the crossing. By starting at a frequency higher than the crossing, we avoid that coupling, which results in atoms staying in the lowest band. This experiment is another indication that the two level tight binding model does not capture the full picture, and that inclusion of more levels is needed to properly describe the system.

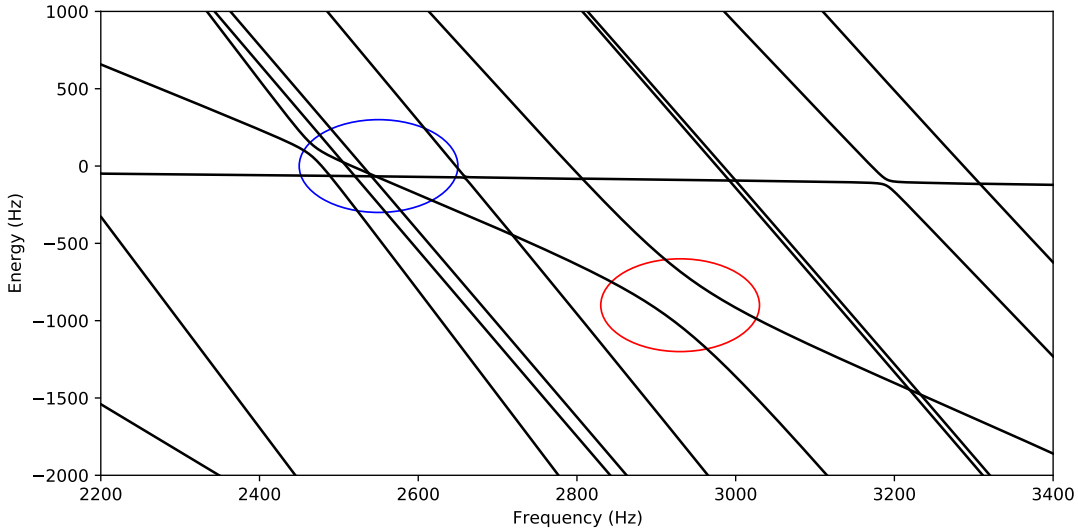

Figure 5.12: Extended basis frequency plot for only $\mathbf{q} = \Gamma$. This shows many avoided crossings, with the blue circle indicates the $n = 2$ crossing, as well as an unavoided crossing with a higher level, as shown in the red circle. When starting at a frequency higher than resonance, this path is not adiabatically connected to the ground state, so we do not observe the heating due to this.

5.2.3 Pre-thermal Relaxation

Having characterized the Floquet lattice and determined conditions without much heating, but also a clearly dominant gauge field, I discuss one of the main results of this thesis, the study of BEC dynamics after quenching into the Floquet bands. We find that the atoms recondense at a low temperature state, even in the presence of high drives, indicating a pre-thermal state during which collisional dynamics operate within the Floquet effective Hamiltonian on timescales faster than that of the Floquet heating timescale.

In order to observe the relaxation dynamics, we quench on the drive, projecting the atoms into the Floquet bands. Starting with an undriven BEC, we quench on the Floquet drive at $\omega/2\pi =$ 2kHz by ramping K_0 from 0 to 2 in 500μs (1 period). The drive is then held for an integer number of periods and the relaxation from $\mathbf{q} = \Gamma$ to $\mathbf{q} = M$ is observed. The choice of integer

steps is selected so that the end phase is constant, and micromotion effects are the same for all measurements. We see an initial relaxation, with recondensing timescales on the order of 2-4 ms, followed by a longer time decay of the atoms. The longer timescale heating is not unexpected due to the strength of the drive. This behavior is shown in Fig. 5.13, where the total fraction of atoms in the $\mathbf{q} = M$ point is displayed as a function of time.

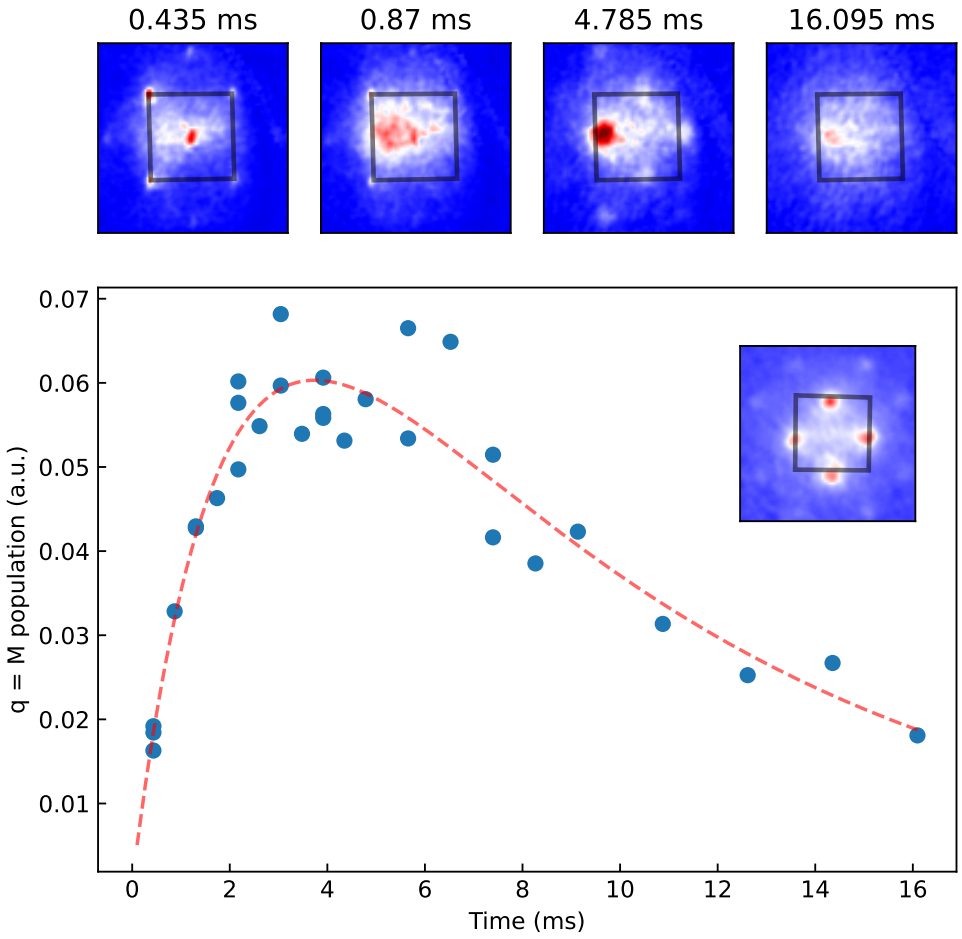

Figure 5.13: Observation of BEC relaxation dynamics near the $n = 2$ resonance. By quenching on the drive, the BEC initially heats out of $\mathbf{q} = \Gamma$ and relaxes into the $\mathbf{q} = M$ points. The plot shows the amplitude (arb. units) of the $\mathbf{q} = M$ peaks. The data in this figure was taken at integer period steps to avoid micromotion. The fit is a sum of a fast exponential growth along with a slower time exponential decay.

For the $n = 1$ resonance, the heating is so strong that a 1 period quench does not result

in the BEC relaxing into the band minima. In order to avoid this heating during preparation of the initial state, we first ramp on the drive at 3.5 kHz in 3ms, which is 500 Hz detuned from the desired value. The 3ms is chosen so that there is still a reasonable fraction of condensed atoms at $\mathbf{q} = \Gamma$ after the ramp, in order to set the initial condition close to a BEC in the "wrong" state. The frequency then is ramped to the desired value of 4kHz in 250us (approximately 1 period) and the shaking continues for an integer number of periods. The relaxation dynamics for the near $n = 1$ case are shown in Fig. 5.14, where the insets show sample images that are phase averaged to display all 4 $\mathbf{q}$ minima. In this experiment, we see similar prethermal dynamics, where there is an initial relaxation on the order of ≈ 3 ms, and then a longer time decay.

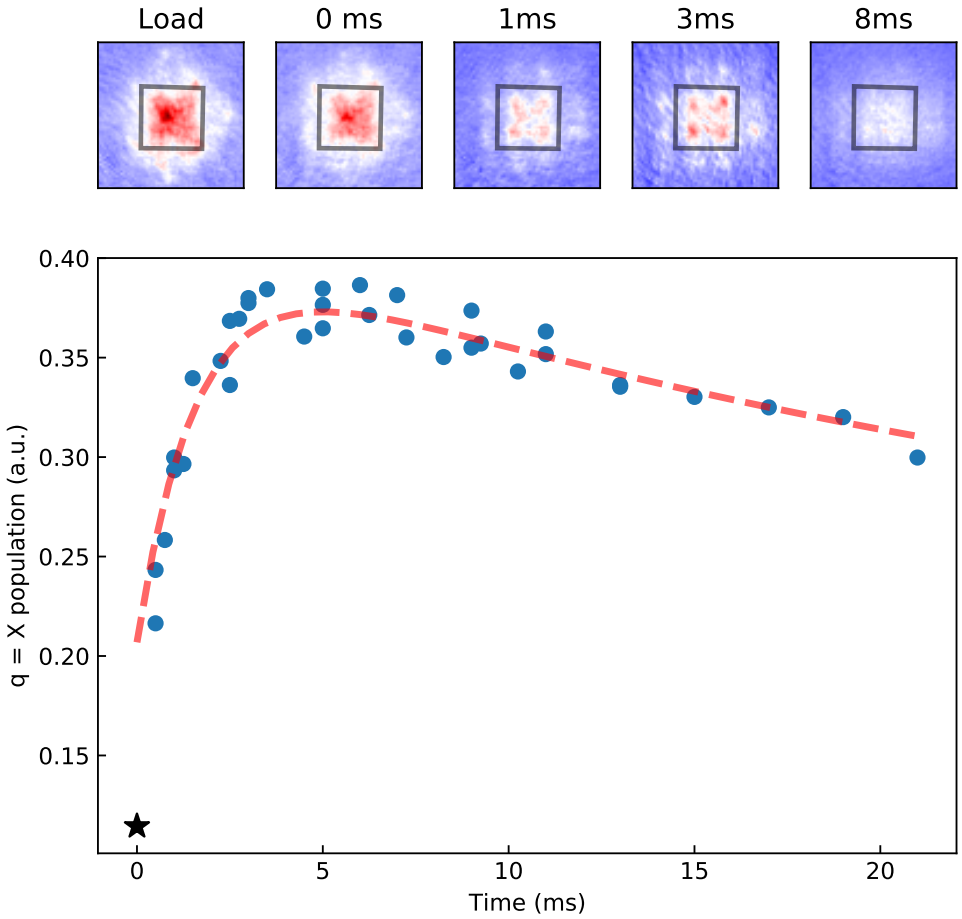

Figure 5.14: Observation of BEC relaxation dynamics. Using the procedure as described in the text, we observe that the BEC initially relaxes from the $\mathbf{q} \approx \Gamma$ points into the $\mathbf{q} = M$ points. The plot shows the relative population in $\mathbf{q} = X$ subtracting the $\mathbf{q} = \Gamma$ population. The fit is the sum of a fast exponential growth with a longer time exponential decay.

The measured populations are obtained by summing the optical depth of the time of flight images for the condensates present in the single shot images and subtracting out the optical depth of the center square. The difference is then divided by the total summed optical depth, to account for any shot to shot noise variation in total number. Boxes used for analysis are highlighted in Fig. 5.15, where the populations are given by $(n_1 + n_2 + n_3 - n_0)/n_T$

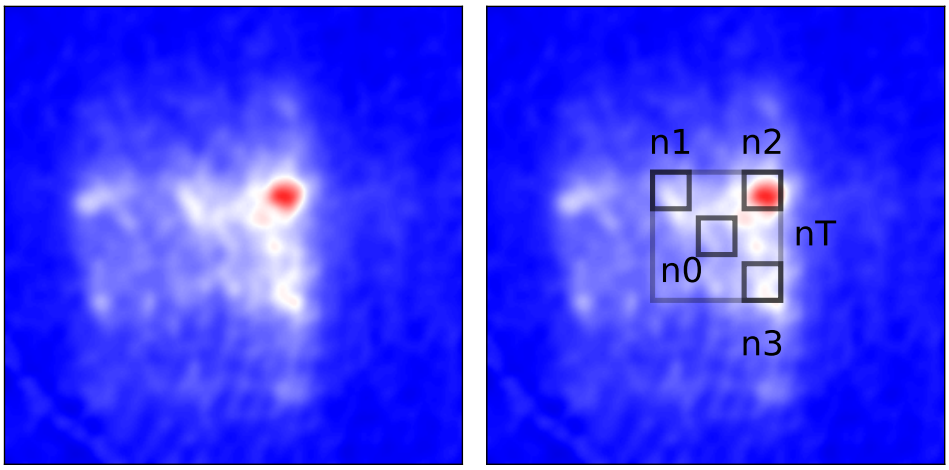

Figure 5.15: Data analysis for quench relaxation. The left panel represents a single shot and the right panel shows the boxes used for calculating the populations.

5.2.4 Relaxation Between Band Minima

Remarkably, the interacting cloud of atoms can relax from an initial state in a static lattice into an effective system with new band minima associated with a simulated gauge field. In this final experiment, I describe our observation of relaxation between the two inequivalent band minima at $\mathbf{q} = X_{\pm}$ by adjusting the ellipticity of the drive and quenching between bands that have different minimum points. Theoretically, the condensate in these two points is expected to be fragmented [78, 79], since the pure condensate's interaction does not select out a particular superposition of the two states.

The symmetry of the $X_{\pm}$ points can be broken by driving the lattice in an elliptical trajectory. The broken symmetry of the drive results in a favored direction, either along $\mathbf{b_1}$ or $\mathbf{b_2}$.

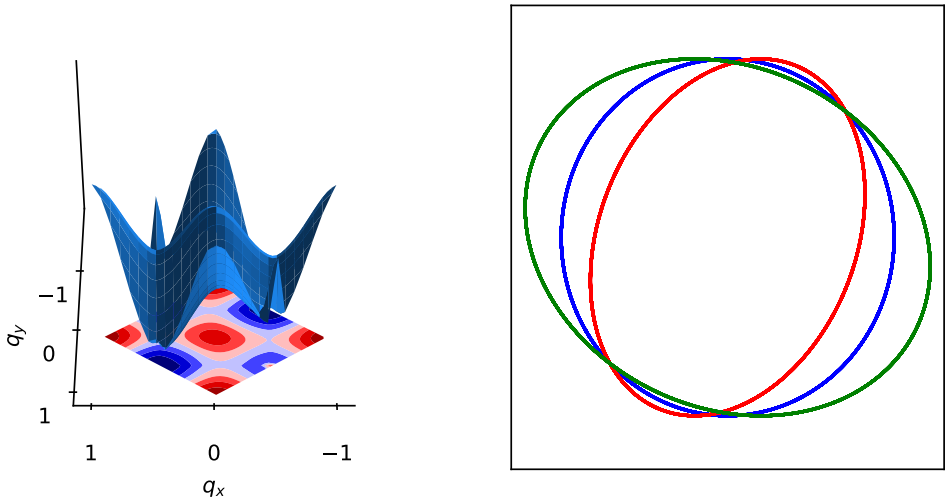

Figure 5.16: Left panel: Band structure, calculated in the extended basis, for our elliptical drive that results in a broken symmetry between X_+ and X_-. The small peak at (1/2,-1/2) is a numeric result of higher bands being present and the full band not being completely isolated. Right panel: The circular trajectory (blue) and then the two slightly elliptical trajectories obtained by setting the relative amplitudes to .8 (red) and 1.1 (green).

We found that the elliptical drive results in a population imbalance between the two points for this driving scheme, and the imbalance is sensitive, to the degree of ellipticity, even when the energy difference between the two minima is small. We study the relaxation between the loaded prethermal state at one ellipticity and the new band minima at a different ellipticity.

We create the different initial and final conditions by adjusting the relative amplitudes of our two piezo mirrors, so that the displacement deviates from strictly circular, as shown in Fig. 5.16. The small ellipticity gives a slight difference in the band structure at X_+, for which we calculate (using the full extended basis) that the single-particle energy difference between the two points is less than 100 Hz. The resulting band structure is shown in Fig 5.16, using $\delta_y = 1.1\delta_x$ and $\phi = \pi/2.2$ from Eq. 5.18.

We adiabatically load atoms into the X_+ point and then quench the bands into a config-

uration where the other X point is the minimum, by adjusting the piezo ratio from 1.1 to 0.8. The resulting pre-thermal relaxation is shown in Fig. 5.17, where we observe recondensation at the new minimum on a short timescale similar to the other $n\pi$ quenches shown in Fig. 5.13 and Fig. 5.14. The fast relaxation between the two minima is further evidence that the condensate is not fragmented, as there is no superposition between the two states.

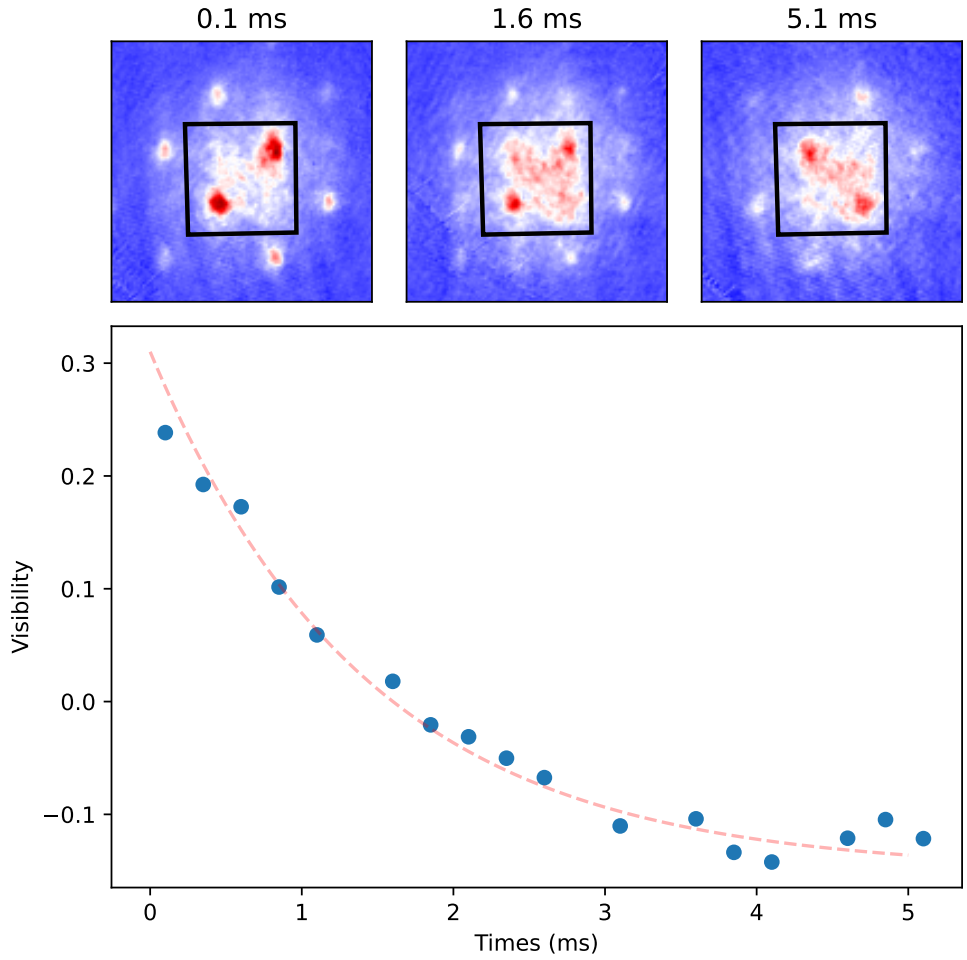

Figure 5.17: Relaxation dynamics between band minima. The shaking is ramped on such that the atoms condense into one minimum. The drive is then quenched such that the opposite point is lower energy. We measure the relative visibility between the two points as a function of time after quenching and note the relaxation from one to the other.

Chapter 6: Outlook

The results described in this thesis demonstrate that in a weakly interacting system in the mean field limit, pre-thermal relaxation to an effective equilibrium state is possible. In this concluding section, I give a brief overview of future work that could be studied with the techniques used in our lab.

6.1 Topology

Realizing effective bands with topological structure is one of the most intriguing applications for Floquet engineering particularly in the low density, highly correlated regime. However, there are significant challenges to reaching that goal. In this section, I will discuss our initial efforts in this direction, along with some challenges that arise in reaching this regime.

6.1.1 Theory

For the periodically driven $n\pi$ flux model, the Hamiltonian, Eq. 5.12, could be expressed as a set of 2x2 matrices in the (a_q, b_q) basis. This two-level system can be represented for each $\mathbf{q}$ using the bloch sphere picture, where the two poles are the a_q, b_q basis states:

$$\mathcal{H}_q = \vec{h}_q \cdot \sigma, \tag{6.1}$$

where $\vec{h}_q$ is the bloch vector and σ are the Pauli matrices. The bloch vector representing the two level system, for each $\mathbf{q}$ in the lowest BZ, can be expressed in spherical coordinates as

$$\vec{h}_q/|\vec{h}_q| = (\sin(\theta_q)\cos(\phi_q), \sin(\theta_q)\sin(\phi_q), \cos(\theta_q)). \tag{6.2}$$

The Berry Curvature, which is a local gauge invariant property of the Hamiltonian that describes the response of eigenstates that are adiabatically varied in $\mathbf{q}$, can be expressed in terms of the bloch vector:

$$\Omega(q) = \frac{1}{2}\left(\partial_{q_x}\vec{h}_q \times \partial_{q_y}\vec{h}_q\right) \cdot \vec{h}_q. \tag{6.3}$$

The Chern number, C, is a gauge invariant property of the band, and is defined as the integrated Berry curvature over the band, $2\pi C = \int_{\text{BZ}} d^2q\, \Omega(q)$, and in the two-level picture it has the simple geometric interpretation as the number of times that the bloch vector covers the entire bloch sphere [80, 81, 82].

In the checkerboard lattice, considering the $n = 1$ case, there are two values of $\mathbf{q}$ for which the off diagonal component of $\mathcal{H}_q$ (h_z) will vanish. At these two $\mathbf{q}$, $\mathbf{q} = \Gamma, M$, which are shown in Fig 6.1, there is no coupling between the a_q, b_q sublattices ($|A\rangle, |B\rangle$). These points with $\langle A|\mathcal{H}_q|B\rangle = 0$, are known as Dirac points, where there is a linear touching of the bands at the proper detuning. At the Dirac point, the eigenstates will be one of the poles of the bloch sphere, namely one of the eigenstates $|A\rangle, |B\rangle$. In the case where $\langle A|\mathcal{H}_q|A\rangle \neq \langle B|\mathcal{H}_q|B\rangle$ for the two $\mathbf{q}$ points with band crossings, then there are two different detunings (frequencies), $\Delta_{1/2}$, where the bands touch at the Dirac points. Due to the circular drive, the Berry curvature will be large and non-negative at the two $\mathbf{q}$ points. For frequencies between the two band crossings, the Berry

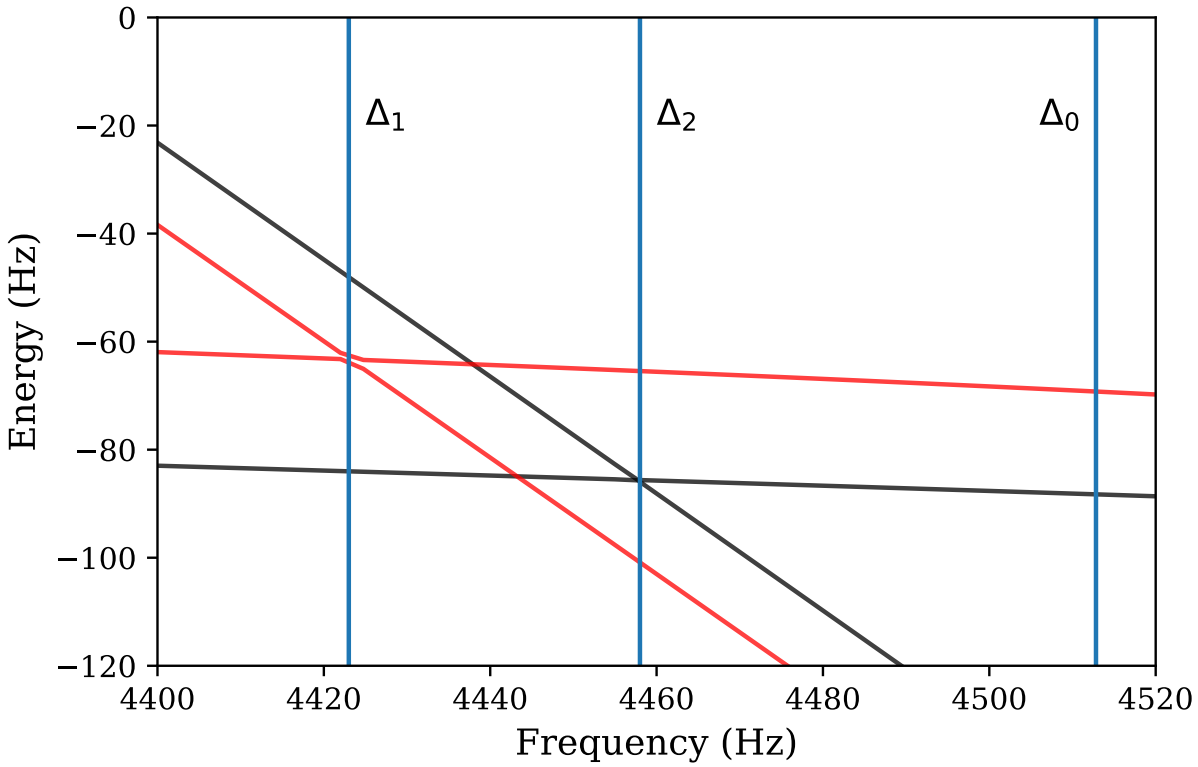

Figure 6.1: Zoom in of the fan plot from Chapter 5, Fig. 5.5, showing the frequency crossing for the two Dirac points at $\mathbf{q} = \Gamma$ (black) and $\mathbf{q} = M$ (red). The band structure is topological in between these points, indicating that there is a roughly 40 Hz window where the non-interacting bands should be topological and have a non-zero Chern number. The Δ_0 line indicates the static $\mathbf{q} = \Gamma$ gap, illustrating the effect that the K_0 shifts can have on the position of features in parameter space.

curvature will have the same sign at those points, resulting in a non-zero Chern number. Outside these band crossing points, the Berry curvature at the two Dirac points will have opposite signs, which will integrate to zero, which is a non-topological band. Intuitively, we can see that there is an exchange of Berry curvature when the bands touch, which results in the boundary at the two detunings.

In order to determine the topological properties of the band, we experimentally need to reconstruct the state at each $\mathbf{q}$, and determine the change in the state as a function of $\mathbf{q}$. The state can be reconstructed by constructing the bloch vector using a tomography procedure, which was

proposed in [82] and experimentally performed with non-interacting, spin polarized fermions in a periodically driven lattice[83]. To understand this experiment, the two sublattices can be represented as the poles of the bloch sphere, and we label them with the states $|q, A\rangle, |q, B\rangle$. The system is initially prepared in a band insulating state, where all atoms are on one pole of the bloch sphere (all in one sublattice). The drive is adiabatically turned on, resulting in coupling between the two sublattices, and the new state can be expressed on the bloch sphere as a linear combination of the two undressed states:

$$|q, -\rangle = \sin(\theta_q/2)|q, A\rangle - \cos(\theta_q/2)e^{i\phi_q}|q, B\rangle. \tag{6.4}$$

The drive is then suddenly shut off and the lattice is quenched to a deep configuration, which results in rotations around the z axis of the bloch sphere. Since the bands are approximately flat in the deep lattice, the rotation about the z-axis are $\mathbf{q}$ independent. After snapping off the lattice potential and releasing the atoms, the population can be seen as the projection along the $|A\rangle + |B\rangle$ axis, resulting in a population at each q of:

$$n_q(t) = f(q)|\langle q, -|A\rangle + \langle q, -|B\rangle|^2 = f(q)(1 - \sin(\theta_q)\cos(\theta_q)), \tag{6.5}$$

where $f(q)$ is the momentum distribution of the Wannier function associated with the deep lattice.

If the atoms are held in the final condition for a variable time t, the state will evolve at the frequency given by the deep lattice band spacing, $\hbar\omega$ so the final angle is $\phi_q \rightarrow \phi_q + \omega t$. Performing a measurement of the populations at various times allows us to reconstruct the angles θ_q and ϕ_q, which are related to the amplitude and phase of the oscillations. By reconstructing

the bloch vector for each $\mathbf{q}$, we are then able to reconstruct the local Berry curvature for $\mathbf{q}$ in the lowest band.

One caveat of this tomography technique is that measurement of the oscillation amplitude does not completely uncover the bloch vector. The z component of the bloch vector, h_z is related to the extracted amplitude as $h_z = \cos(\theta_q) \equiv \sqrt{|1 - \sin^2(\theta_q)|}$, meaning that we can only extract an amplitude and not the sign. Since a topological band will fully cover the band, this means that in order to see a topological state, h_z must cross through 0, which would show up as a cusp in the amplitude.

6.1.2 Experimental Work

Since we work with bosons, there are two significant differences between our system and the non-interacting Fermi system in [83]. The first is that we cannot fill the lowest band as simply as in the case of fermionic atoms. The second and more challenging difference, is that our system is inherently interacting, which will be discussed later. Our technical approach to prepare a filled band with all atoms on one site is to load the atoms into a deep tilted lattice, with a depth of about 25 E_R and a tilt of 15 kHz. This scrambles the phase on each site and fills $\mathbf{q}$ within the lowest band, mimicking the band insulating state, where all atoms are loaded into one sublattice. After loading, the atoms are held in the deep lattice for a short time (5ms), and then in 4ms, we simultaneously ramp down the lattice depth and ramp on the amplitude of the circular shaking, at an off-resonant frequency. To mix the bands and enter the topological regime, we sweep the drive frequency (which changes the detuning) to a final value. If the bands are truly ramped through a Dirac point, then the sweep can not be adiabatic enough to prevent undesired transfer to the

upper band. We select sweep times that balance between too fast for adiabaticity and too slow for heating to have an impact.

Once the final detuning is reached, we quench the lattice back to 25 E_R, so that the bands are flat, and hold for a variable time, allowing for the bloch sphere to rotate about the z axis. After the variable hold time, we snap off all confining potentials and observe absorption images after time of flight. The density oscillations, as shown in Fig. 6.2 and Fig. 6.3 allow us to reconstruct the amplitude and phase of our initial state, and reconstruct the bloch vector for each $\mathbf{q}$.

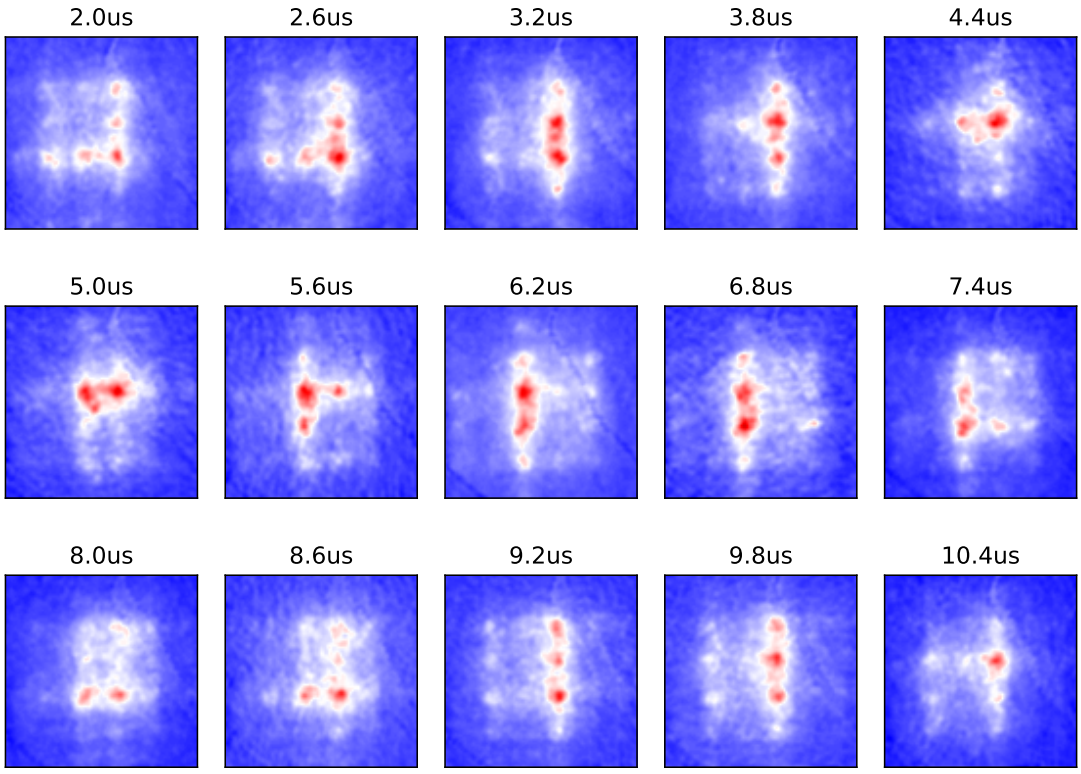

Figure 6.2: Density oscillations resulting from the tomography procedure. The amplitude and phase of the oscillation at each $\mathbf{q}$ is related to the relative amplitudes and phase of the initial superposition state on the Bloch sphere.

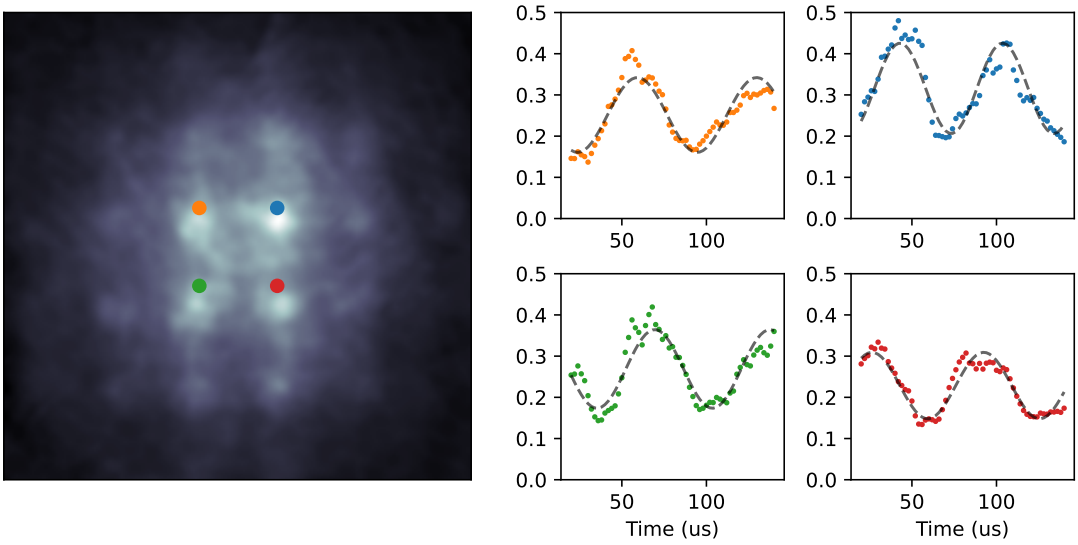

Figure 6.3: Oscillation for four different pixels after holding in the flat bands. The left image shows the mean image of Fig 6.2 and the points are color coordinated with the images in the right panel. Each of the four charts shows the raw density oscillation points, as well as the best sin fit to the data (dashed black curve).

We analyze the images by fitting Eq.6.5 to the oscillations of the normalized pixel count for each pixel from Fig 6.3. Each series, $n_q(t)$, is smoothed with a Savitzky-Golay filter of window length 5 and polynomial order 3. An example of the extracted amplitude and phase of each $\mathbf{q}$ is shown in Fig. 6.4. The fits show 4 maximum amplitudes at the band edge and a phase vortex in the center.

Despite observing the phase vortex and the clear oscillations between the four minima, a topological band was not observed. The extracted amplitude never exhibited a cusp going through 0, which indicates the crossing of h_z over the equator on the Bloch sphere. It seems that this is a result of interaction based rethermalization of the band into the band minima, as observed in Chapter 5 of this thesis, where the π flux model exhibits a quick rethermalization into a prethermal state at the band minimum. Despite starting in a filled band, we observe that when the lattice is reduced to its final depth and the shaking is turned on, the atoms recondense

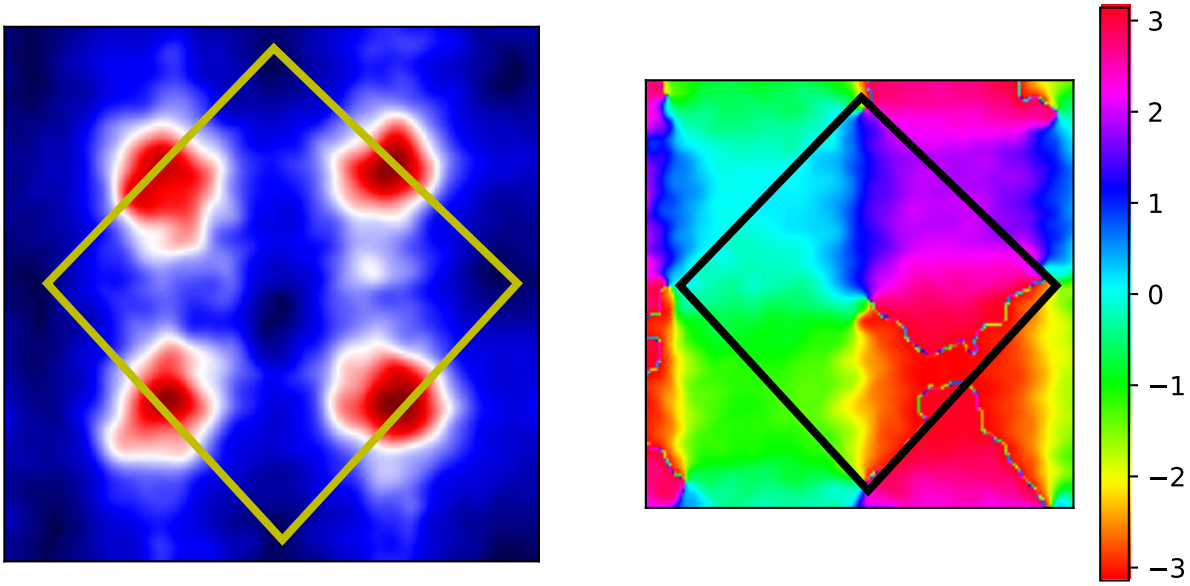

Figure 6.4: Amplitude (left) and phase (right) of oscillations for each $\mathbf{q}$ from the previous figures. The diamond indicates the boundary of the lowest Brillouin Zone.

into the minima, as seen in the time of flight images. As a result $\vec{h}$ does not traverse through the bloch sphere equator. In addition to allowing for the recondensing of the condensate, it is unclear how interactions modify the band structure particularly at the high temperatures required to fill the band.

Our attempt to see non-interacting topological band structures with interacting bosons was unsuccessful, but the dynamic thermal "relaxation" into the time dependent Floquet states provides hope that this system can be studied in prethermal conditions. Future studies could elucidate the potential role of interactions in destroying the topological regime.

Bibliography

[1] Gregor Jotzu, Michael Messer, Rémi Desbuquois, Martin Lebrat, Thomas Uehlinger, Daniel Greif, and Tilman Esslinger. Experimental realization of the topological haldane model with ultracold fermions. *Nature*, 515(7526):237–240, November 2014.

[2] Fabrice Gerbier and Jean Dalibard. Gauge fields for ultracold atoms in optical superlattices. *New Journal of Physics*, 12(3):033007, mar 2010.

[3] N Goldman, G Juzeliūnas, P Öhberg, and I B Spielman. Light-induced gauge fields for ultracold atoms. *Reports on Progress in Physics*, 77(12):126401, nov 2014.

[4] M. Aidelsburger, M. Lohse, C. Schweizer, M. Atala, J. T. Barreiro, S. Nascimbène, N. R. Cooper, I. Bloch, and N. Goldman. Measuring the chern number of hofstadter bands with ultracold bosonic atoms. *Nature Physics*, 11(2):162–166, December 2014.

[5] Victor Galitski and Ian B. Spielman. Spin–orbit coupling in quantum gases. *Nature*, 494(7435):49–54, February 2013.

[6] N. Goldman and J. Dalibard. Periodically driven quantum systems: Effective hamiltonians and engineered gauge fields. *Phys. Rev. X*, 4:031027, Aug 2014.

[7] Takuya Kitagawa, Erez Berg, Mark Rudner, and Eugene Demler. Topological characterization of periodically driven quantum systems. *Phys. Rev. B*, 82:235114, Dec 2010.

[8] Andreas Hemmerich. Effective time-independent description of optical lattices with periodic driving. *Phys. Rev. A*, 81:063626, Jun 2010.

[9] Y.-J. Lin, K. Jiménez-García, and I. B. Spielman. Spin–orbit-coupled bose–einstein condensates. *Nature*, 471(7336):83–86, March 2011.

[10] M. Hafezi, A. S. Sørensen, E. Demler, and M. D. Lukin. Fractional quantum hall effect in optical lattices. *Physical Review A*, 76(2), August 2007.

[11] Tigran A. Sedrakyan, Victor M. Galitski, and Alex Kamenev. Statistical transmutation in floquet driven optical lattices. *Phys. Rev. Lett.*, 115:195301, Nov 2015.

[12] Christian Schweizer, Fabian Grusdt, Moritz Berngruber, Luca Barbiero, Eugene Demler, Nathan Goldman, Immanuel Bloch, and Monika Aidelsburger. Floquet approach to z2 lattice gauge theories with ultracold atoms in optical lattices. *Nature Physics*, 15(11):1168–1173, September 2019.

[13] Achilleas Lazarides, Arnab Das, and Roderich Moessner. Equilibrium states of generic quantum systems subject to periodic driving. *Phys. Rev. E*, 90:012110, Jul 2014.

[14] Marin Bukov, Markus Heyl, David A. Huse, and Anatoli Polkovnikov. Heating and many-body resonances in a periodically driven two-band system. *Physical Review B*, 93(15), April 2016.

[15] Dmitry A. Abanin, Wojciech De Roeck, Wen Wei Ho, and François Huveneers. Effective hamiltonians, prethermalization, and slow energy absorption in periodically driven many-body systems. *Physical Review B*, 95(1), January 2017.

[16] Marin Bukov, Sarang Gopalakrishnan, Michael Knap, and Eugene Demler. Prethermal floquet steady states and instabilities in the periodically driven, weakly interacting bose-hubbard model. *Phys. Rev. Lett.*, 115:205301, Nov 2015.

[17] K. Singh, C. J. Fujiwara, Z. A. Geiger, E. Q. Simmons, M. Lipatov, A. Cao, P. Dotti, S. V. Rajagopal, R. Senaratne, T. Shimasaki, M. Heyl, A. Eckardt, and D. M. Weld. Quantifying and controlling prethermal nonergodicity in interacting floquet matter. *Physical Review X*, 9(4), October 2019.

[18] Dmitry A. Abanin, Wojciech De Roeck, and François Huveneers. Exponentially Slow Heating in Periodically Driven Many-Body Systems. *Physical Review Letters*, 115(25):1–5, 2015.

[19] Marin Bukov, Sarang Gopalakrishnan, Michael Knap, and Eugene Demler. Prethermal floquet steady states and instabilities in the periodically driven, weakly interacting bose-hubbard model. *Phys. Rev. Lett.*, 115:205301, Nov 2015.

[20] Takashi Mori, Tomotaka Kuwahara, and Keiji Saito. Rigorous Bound on Energy Absorption and Generic Relaxation in Periodically Driven Quantum Systems. *Physical Review Letters*, 116(12):1–5, 2016.

[21] Antonio Rubio-Abadal, Matteo Ippoliti, Simon Hollerith, David Wei, Jun Rui, S. L. Sondhi, Vedika Khemani, Christian Gross, and Immanuel Bloch. Floquet prethermalization in a bose-hubbard system. *Phys. Rev. X*, 10:021044, May 2020.

[22] Douglas R. Hofstadter. Energy levels and wave functions of bloch electrons in rational and irrational magnetic fields. *Phys. Rev. B*, 14:2239–2249, Sep 1976.

[23] R. K. Pathria. *Statistical mechanics*. Academic Press, Boston, 2011.

[24] Franco Dalfovo, Stefano Giorgini, Lev P. Pitaevskii, and Sandro Stringari. Theory of bose-einstein condensation in trapped gases. *Rev. Mod. Phys.*, 71:463–512, Apr 1999.

[25] Milena Grifoni and Peter Hänggi. Driven quantum tunneling. *Physics Reports*, 304(5-6):229–354, October 1998.

[26] Martin Holthaus. Floquet engineering with quasienergy bands of periodically driven optical lattices. *Journal of Physics B: Atomic, Molecular and Optical Physics*, 49(1):013001, nov 2015.

[27] Marin Bukov, Luca D'Alessio, and Anatoli Polkovnikov. Universal high-frequency behavior of periodically driven systems: from dynamical stabilization to floquet engineering. *Advances in Physics*, 64(2):139–226, 2015.

[28] Saar Rahav, Ido Gilary, and Shmuel Fishman. Effective hamiltonians for periodically driven systems. *Phys. Rev. A*, 68:013820, Jul 2003.

[29] Wilhelm Magnus. On the exponential solution of differential equations for a linear operator. *Communications on Pure and Applied Mathematics*, 7(4):649–673, November 1954.

[30] N. N. Bogolyubov. On the theory of superfluidity. *J. Phys. (USSR)*, 11:23–32, 1947.

[31] Mark Edwards, P. A. Ruprecht, K. Burnett, R. J. Dodd, and Charles W. Clark. Collective excitations of atomic bose-einstein condensates. *Phys. Rev. Lett.*, 77:1671–1674, Aug 1996.

[32] A. J. Leggett. *Broken Gauge Symmetry in a Bose Condensate*, pages 452–462. Cambridge University Press, 1995.

[33] Rudolf Grimm, Matthias Weidemüller, and Yurii B. Ovchinnikov. Optical dipole traps for neutral atoms. 1999.

[34] J. Sebby-Strabley, M. Anderlini, P. S. Jessen, and J. V. Porto. Lattice of double wells for manipulating pairs of cold atoms. *Phys. Rev. A*, 73:033605, Mar 2006.

[35] D. Jaksch, C. Bruder, J. I. Cirac, C. W. Gardiner, and P. Zoller. Cold bosonic atoms in optical lattices. *Physical Review Letters*, 81(15):3108–3111, October 1998.

[36] Matthew P. A. Fisher, Peter B. Weichman, G. Grinstein, and Daniel S. Fisher. Boson localization and the superfluid-insulator transition. *Physical Review B*, 40(1):546–570, July 1989.

[37] Markus Greiner, Olaf Mandel, Tilman Esslinger, Theodor W. Hänsch, and Immanuel Bloch. Quantum phase transition from a superfluid to a mott insulator in a gas of ultracold atoms. *Nature*, 415(6867):39–44, January 2002.

[38] Thilo Stöferle, Henning Moritz, Christian Schori, Michael Köhl, and Tilman Esslinger. Transition from a strongly interacting 1d superfluid to a mott insulator. *Physical Review Letters*, 92(13), March 2004.

[39] R. Peierls. Zur theorie des diamagnetismus von leitungselektronen. *Zeitschrift fur Physik*, 80(11-12):763–791, November 1933.

[40] André Eckardt, Martin Holthaus, Hans Lignier, Alessandro Zenesini, Donatella Ciampini, Oliver Morsch, and Ennio Arimondo. Exploring dynamic localization with a bose-einstein condensate. *Phys. Rev. A*, 79:013611, Jan 2009.

[41] C. E. Creffield, F. Sols, D. Ciampini, O. Morsch, and E. Arimondo. Expansion of matter waves in static and driven periodic potentials. *Phys. Rev. A*, 82:035601, Sep 2010.

[42] André Eckardt. Colloquium: Atomic quantum gases in periodically driven optical lattices. *Rev. Mod. Phys.*, 89:011004, Mar 2017.

[43] F. Grossmann, T. Dittrich, P. Jung, and P. Hänggi. Coherent destruction of tunneling. *Phys. Rev. Lett.*, 67:516–519, Jul 1991.

[44] Alessandro Zenesini, Hans Lignier, Donatella Ciampini, Oliver Morsch, and Ennio Arimondo. Coherent control of dressed matter waves. *Phys. Rev. Lett.*, 102:100403, Mar 2009.

[45] Mantas Račiūnas, Giedrius Žlabys, André Eckardt, and Egidijus Anisimovas. Modified interactions in a floquet topological system on a square lattice and their impact on a bosonic fractional chern insulator state. *Phys. Rev. A*, 93:043618, Apr 2016.

[46] Naomichi Hatano and Masuo Suzuki. Finding exponential product formulas of higher orders. 2005.

[47] C. A. Bracamontes, J. Maslek, and J. V. Porto. Realization of a floquet-engineered moat band for ultracold atoms. *Phys. Rev. Lett.*, 128:213401, May 2022.

[48] Roger Brown. *NONEQUILIBRIUM MANYBODY DYNAMICS WITH ULTRACOLD ATOMS IN OPTICAL LATTICES AND SELECTED PROBLEMS IN ATOMIC PHYSICS*. PhD thesis, 2014.

[49] Phillip L. Gould, George A. Ruff, and David E. Pritchard. Diffraction of atoms by light: The near-resonant kapitza-dirac effect. *Physical Review Letters*, 56(8):827–830, February 1986.

[50] E. Magnan, J. Maslek, C. Bracamontes, A. Restelli, T. Boulier, and J. V. Porto. A low-steering piezo-driven mirror. *Review of Scientific Instruments*, 89(7):073110, July 2018.

[51] Konrad Viebahn, Joaquín Minguzzi, Kilian Sandholzer, Anne-Sophie Walter, Manish Sajnani, Frederik Görg, and Tilman Esslinger. Suppressing dissipation in a floquet-hubbard system. *Physical Review X*, 11(1), March 2021.

[52] Pranjal Bordia, Henrik Lüschen, Ulrich Schneider, Michael Knap, and Immanuel Bloch. Periodically driving a many-body localized quantum system. *Nature Physics*, 13(5):460–464, January 2017.

[53] Sarang Gopalakrishnan, Michael Knap, and Eugene Demler. Regimes of heating and dynamical response in driven many-body localized systems. *Physical Review B*, 94(9), September 2016.

[54] Antonio Rubio-Abadal, Matteo Ippoliti, Simon Hollerith, David Wei, Jun Rui, S. L. Sondhi, Vedika Khemani, Christian Gross, and Immanuel Bloch. Floquet prethermalization in a bose-hubbard system. *Physical Review X*, 10(2), May 2020.

[55] S. Lellouch, M. Bukov, E. Demler, and N. Goldman. Parametric instability rates in periodically driven band systems. *Phys. Rev. X*, 7:021015, May 2017.

[56] C. E. Creffield. Instability and control of a periodically driven bose-einstein condensate. *Physical Review A*, 79(6), June 2009.

[57] Grazia Salerno, Tomoki Ozawa, Hannah M. Price, and Iacopo Carusotto. Floquet topological system based on frequency-modulated classical coupled harmonic oscillators. *Phys. Rev. B*, 93:085105, Feb 2016.

[58] L D Landau and E M Lifshitz. *Mechanics*. Butterworth-Heinemann, Oxford, England, 3 edition, January 1982.

[59] K. Wintersperger, M. Bukov, J. Näger, S. Lellouch, E. Demler, U. Schneider, I. Bloch, N. Goldman, and M. Aidelsburger. Parametric instabilities of interacting bosons in periodically driven 1d optical lattices. *Physical Review X*, 10(1), February 2020.

[60] T. Boulier, J. Maslek, M. Bukov, C. Bracamontes, E. Magnan, S. Lellouch, E. Demler, N. Goldman, and J. V. Porto. Parametric heating in a 2d periodically driven bosonic system: Beyond the weakly interacting regime. *Physical Review X*, 9(1), March 2019.

[61] L. Fallani, L. De Sarlo, J. E. Lye, M. Modugno, R. Saers, C. Fort, and M. Inguscio. Observation of dynamical instability for a bose-einstein condensate in a moving 1d optical lattice. *Physical Review Letters*, 93(14), September 2004.

[62] Martin Reitter, Jakob Näger, Karen Wintersperger, Christoph Sträter, Immanuel Bloch, André Eckardt, and Ulrich Schneider. Interaction dependent heating and atom loss in a periodically driven optical lattice. *Physical Review Letters*, 119(20), November 2017.

[63] Colin J. Kennedy, William Cody Burton, Woo Chang Chung, and Wolfgang Ketterle. Observation of bose–einstein condensation in a strong synthetic magnetic field. *Nature Physics*, 11(10):859–864, August 2015.

[64] Philipp Hauke, Olivier Tieleman, Alessio Celi, Christoph Ölschläger, Juliette Simonet, Julian Struck, Malte Weinberg, Patrick Windpassinger, Klaus Sengstock, Maciej Lewenstein, and André Eckardt. Non-abelian gauge fields and topological insulators in shaken optical lattices. *Physical Review Letters*, 109(14), oct 2012.

[65] C E Creffield, G Pieplow, F Sols, and N Goldman. Realization of uniform synthetic magnetic fields by periodically shaking an optical square lattice. *New Journal of Physics*, 18(9):093013, sep 2016.

[66] Li-Chung Ha, Logan W. Clark, Colin V. Parker, Brandon M. Anderson, and Cheng Chin. Roton-maxon excitation spectrum of bose condensates in a shaken optical lattice. *Phys. Rev. Lett.*, 114:055301, Feb 2015.

[67] Colin V. Parker, Li-Chung Ha, and Cheng Chin. Direct observation of effective ferromagnetic domains of cold atoms in a shaken optical lattice. *Nature Physics*, 9(12):769–774, October 2013.

[68] H. Lignier, C. Sias, D. Ciampini, Y. Singh, A. Zenesini, O. Morsch, and E. Arimondo. Dynamical control of matter-wave tunneling in periodic potentials. *Phys. Rev. Lett.*, 99:220403, Nov 2007.

[69] C. J. Fujiwara, Kevin Singh, Zachary A. Geiger, Ruwan Senaratne, Shankari V. Rajagopal, Mikhail Lipatov, and David M. Weld. Transport in floquet-bloch bands. *Phys. Rev. Lett.*, 122:010402, Jan 2019.

[70] Kai-Xuan Yao, Zhendong Zhang, and Cheng Chin. Domain-wall dynamics in bose–einstein condensates with synthetic gauge fields. *Nature*, 602(7895):68–72, feb 2022.

[71] Kilian Sandholzer, Anne-Sophie Walter, Joaquín Minguzzi, Zijie Zhu, Konrad Viebahn, and Tilman Esslinger. Floquet engineering of individual band gaps in an optical lattice using a two-tone drive. *Phys. Rev. Research*, 4:013056, Jan 2022.

[72] J. Struck, C. Ölschläger, R. Le Targat, P. Soltan-Panahi, A. Eckardt, M. Lewenstein, P. Windpassinger, and K. Sengstock. Quantum simulation of frustrated classical magnetism in triangular optical lattices. *Science*, 333(6045):996–999, aug 2011.

[73] B. K. Stuhl, H.-I. Lu, L. M. Aycock, D. Genkina, and I. B. Spielman. Visualizing edge states with an atomic bose gas in the quantum hall regime. *Science*, 349(6255):1514–1518, sep 2015.

[74] Lih-King Lim, Andreas Hemmerich, and C. Morais Smith. Artificial staggered magnetic field for ultracold atoms in optical lattices. *Physical Review A*, 81(2), February 2010.

[75] Y J Lin, R L Compton, K Jimenez-Garcia, W D Phillips, J V Porto, and I B Spielman. A synthetic electric force acting on neutral atoms. *NATURE PHYSICS*, 7(7):531–534, jul 2011.

[76] Stephen Powell, Ryan Barnett, Rajdeep Sensarma, and Sankar Das Sarma. Bogoliubov theory of interacting bosons on a lattice in a synthetic magnetic field. *Physical Review A - Atomic, Molecular, and Optical Physics*, 83(1):1–19, 2011.

[77] Erich J. Mueller, Tin-Lun Ho, Masahito Ueda, and Gordon Baym. Fragmentation of bose-einstein condensates. *Phys. Rev. A*, 74:033612, Sep 2006.

[78] G. Möller and N. R. Cooper. Condensed ground states of frustrated bose-hubbard models. *Phys. Rev. A*, 82:063625, Dec 2010.

[79] Lih-King Lim, Andreas Hemmerich, and C. Morais Smith. Artificial staggered magnetic field for ultracold atoms in optical lattices. *Phys. Rev. A*, 81:023404, Feb 2010.

[80] M. Z. Hasan and C. L. Kane. Colloquium: Topological insulators. *Rev. Mod. Phys.*, 82:3045–3067, Nov 2010.

[81] Matthias Tarnowski, F. Nur Ünal, Nick Fläschner, Benno S. Rem, André Eckardt, Klaus Sengstock, and Christof Weitenberg. Measuring topology from dynamics by obtaining the chern number from a linking number. *Nature Communications*, 10(1), apr 2019.

[82] Philipp Hauke, Maciej Lewenstein, and André Eckardt. Tomography of band insulators from quench dynamics. *Phys. Rev. Lett.*, 113:045303, Jul 2014.

[83] N. Fläschner, B. S. Rem, M. Tarnowski, D. Vogel, D.-S. Lühmann, K. Sengstock, and C. Weitenberg. Experimental reconstruction of the berry curvature in a floquet bloch band. *Science*, 352(6289):1091–1094, may 2016.